ΕΛΛΗΝΙΚΗ ΔΗΜΟΚΡΑΤΙΑ
Εθνικόν και Καποδιστριακόν Πανεπιστήμιον Αθηνών
ΙΔΡΥΘΕΝ ΤΟ 1837

hcmr
ΕΛΚΕΘΕ
ΕΛΛΗΝΙΚΟ ΚΕΝΤΡΟ ΘΑΛΑΣΣΙΩΝ ΕΡΕΥΝΩΝ
HELLENIC CENTRE FOR MARINE RESEARCH

NATIONAL AND KAPODISTRIAN UNIVERSITY OF ATHENS

SCHOOL OF SCIENCE

INTERINSTITUTIONAL POSTGRADUATE PROGRAM NKUA-HCMR

OCEANOGRAPHY AND MANAGEMENT OF THE MARINE ENVIRONMENT

# SEDIMENTATION PROCESSES AND PALEOCEANOGRAPHIC EVOLUTION IN THE EXTREME ENVIRONMENT OF DISCOVERY DEEP (RED SEA RIFT)

M.Sc. THESIS

Arianoutsou Aliki Stefania

**Athens 2024**

NATIONAL AND KAPODISTRIAN UNIVERSITY OF ATHENS
SCHOOL OF SCIENCE
INTERINSTITUTIONAL POSTGRADUATE PROGRAM NKUA-HCMR
OCEANOGRAPHY AND MANAGEMENT OF THE MARINE ENVIRONMENT

# SEDIMENTATION PROCESSES AND PALEOCEANOGRAPHIC EVOLUTION IN THE EXTREME ENVIRONMENT OF DISCOVERY DEEP (RED SEA RIFT)

M.Sc. THESIS

Arianoutsou Aliki Stefania

<u>M.Sc. Thesis Committee:</u>

I. P. Panagiotopoulos, Assistant Professor NKUA (supervisor)

M. V. Triantaphyllou, Professor NKUA

Aristomenis P. Karageorgis, Director at the Institute of Oceanography of HCMR

**Athens 2024**

# ABSTRACT

Situated within the central Red Sea Rift zone, some of the most mesmerizing environments, the hot brine-filled basins, have been discovered. This study investigates the dynamics of the Discovery Deep hot brine pool, an understudied depression adjacent to the highly mineralized Atlantis II Deep, employing sedimentological and micropaleontological analyses, along with radiocarbon ($^{14}C$) dating.

The geoarchive from the deep extends up to 3.5 m below the seafloor and exhibits three distinct lithostratigraphic units, reflecting shifts in sedimentation processes and environmental conditions over the past ~22 cal ka BP. The sedimentary sequence indicates changes from periods of slow pelagic sedimentation to periods of extreme depositional rates driven by hydrothermal activity, lasting from ~15 to 4 cal ka BP. Unlike the neighboring Atlantis II Deep, metal contents in Discovery Deep sediments display significantly lower values, suggesting occasional intense overflows of the Atlantis II brine as its source. Moreover, the dominance of the sand fraction in the hydrothermal influenced interval suggests either overflows or mass wasting episodes. Challenging previous assumptions, the presence of benthic foraminiferal assemblages highlights their adaptability to extreme settings, with their distribution being profoundly affected by hydrothermal activity. Along with the presence of Mn-rich layers they suggest periodic dissolved oxygen influxes into the brine.

Overall, this work contributes to understanding the unique environment of Discovery Deep, complementing existing knowledge, by highlighting the complex interplay between sedimentation and hydrothermal activity shaped by regional tectonics and oceanographic changes, along with biological adaptation.

**Key words:** Red Sea brine pools, Discovery Deep, Sedimentation, Paleoceanography Hydrothermal activity

# ACKNOWLEDGEMENTS

This master thesis was conducted under the interinstitutional postgraduate program NKUA-HCMR "Oceanography and Management of the Marine Environment", under the supervision of Assistant Professor Dr. Ioannis Panagiotopoulos.

This study would not have been possible without the assistance and nurturing of several individuals, to whom I would like to express my warmest gratitude.

I am profoundly grateful to my supervisor, Assistant Professor Dr. Ioannis Panagiotopoulos, for his continuous support, guidance and insightful suggestions throughout this study, which have been instrumental in shaping this work.

Moreover, I cannot begin to express my thanks and genuine appreciation to Professor Dr. Maria Triantaphyllou for her helpful advice, unwavering support and encouragement throughout this journey.

I would also like to sincerely thank Dr. Aristomenis Karageorgis for the financial support that enabled the completion of this research, as well as for his constructive feedback.

I am also deeply thankful to Professor Dr. Pavlos Avramidis and his team from the Laboratory of Sedimentology, Department of Geology, University of Patras, for their hospitality, invaluable assistance and support during my time at their laboratory.

Finally, I extend my sincere appreciation to Assistant Professor Dr. Theodora Tsourou for generously sharing her time, valuable assistance and insights.

# CONTENTS

# LIST OF FIGURES

# LIST OF TABLES

# 1. INTRODUCTION

## 1.1. Theoretical Background

Oceans cover ~71% of the Earth's surface. They accommodate the most unique and complex ecosystems and have a vital role in regulating climate and sustaining life, being inextricably linked to the Earth's geological processes. Mankind, since antiquity, has been drawn to the ocean recognizing its importance, determined to unravel its secrets. On that account, scientists from different backgrounds have been exploring the ocean in relation to its formation processes, physics, chemical composition, biodiversity and resources.

Earth's recent geological history is best reflected in marine deposits, where sedimentation is, generally, unceasing for the last ~100 Ma at least, despite the fact that several gaps in the sedimentary sequences (called "hiatuses") have been proved to occur, frustrating much effort at reconstruction. The examination of the sedimentary record leads to the reconstruction of paleoenvironments, providing a greater understanding of the Earth's evolution through the geological time scale. Sedimentological analyses in marine cores, including, for example, granulometric and geochemical analyses, are fundamental in identifying sedimentation trends and the hydrodynamic regime of a basin during deposition. Moreover, the microfossils preserved in sediments are prominent witnesses to the Earth's geological past. Apart from dating strata, these organisms are extremely sensitive to environmental changes and are, thus, established as one of the most important paleoceanographic proxies, revealing the environmental conditions at the time of deposition.

Red Sea is, by all accounts, a highly idiosyncratic environment with great geological significance. For starters, it is a juvenile ocean basin and the sole place on Earth where early stages of seafloor spreading are observable, rendering it a unique environment for the study of rifting processes. Additionally, the hydrothermal activity reported in the region as well as the presence of hot and cold brine pools has prompted numerous oceanographic surveys in pursuit of potential financial benefits from mineral exploitation. Furthermore, as a semi-enclosed basin, with limited connection to the open ocean, it is particularly susceptible to global climate changes and, thus, an ideal location for recording paleoceanographic and paleoclimatic fluctuations. Therefore, Red Sea is undoubtedly a valuable area for geological research, due to its unique tectonics, potential mineral resources and paleoenvironmental record.

## 1.2. Scope of Thesis

The hot brine pools in the central Red Sea Rift are some of the most fascinating and bizarre environments found on Earth, however, not all of them have been thoroughly explored. Although the Atlantis II Deep, located at the central Red Sea, has been extensively studied, as it contains the most massive metalliferous deposits worldwide, there is only minimal and mostly outdated research concerning its nearby brine pool, i.e., the Discovery Deep. Taking that into consideration, this thesis aims to reduce this knowledge gap, by studying the sedimentation processes and paleoceanographic evolution of Discovery Deep.

The current study focused on the analysis of sediment samples from a 3.5-m-long gravity core recovered from the Discovery Deep brine, in order to determine the vertical distribution of sedimentological characteristics (physical and geochemical) in an attempt to detect the depositional trends in this extreme environment. Hence, the sedimentary record could, in turn, reveal variations in the physico-chemical conditions of the brine, resulting from changes in the hydrothermal activity within the deep or interactions between the brine and seawater.

Additionally, the investigation of autochthonous benthic foraminifera, including their diversity, vertical distribution and morphological characteristics of their tests, could assist in identifying the impact of hydrothermal activity on their assemblages. Furthermore, their study could contribute to the paleoceanographic reconstruction of the brine area, thereby enhancing our understanding of how environmental conditions have influenced sedimentation.

# 2. HYDROTHERMAL ACTIVITY AND BRINE POOL FORMATION

## 2.1. Hydrothermal Activity at the Global Mid-Ocean Ridge

Seafloor relief is considerably more complex than the continental topography. One of the most remarkable topographic features of the seabed, and the most extensive on Earth's surface, is the global mid-ocean ridge, which is a continuous submarine mountain range stretching over ~75,000 km and directly linked to plate tectonics. The global mid-ocean ridge emerges at divergent plate boundaries, where seafloor spreading takes place, and is characterized by great seismic and volcanic activity, accounting for over 75% of the Earth's volcanism (Harris, 2020). At divergent boundaries, rising convection currents from the asthenosphere push magma to the lithosphere, eventually, rupturing the continental crust. After the initial phase of continental rifting, as the two plates begin to drift apart, new oceanic crust is formed along a spreading axis by the rising magma and basaltic lava extrusion, gradually shaping a segment of the global mid-ocean ridge (Hess, 1962; Wilson et al., 2019). Variations in the spreading rate of the ridge segments affect their morphology, with slow-spreading centers producing elevated and more rugged topography featuring rift valleys, in contrast to the fast-spreading centers (LaFemina, 2015).

Some of the most astonishing and extreme environments found on Earth are located at seafloor spreading centers, i.e., the hydrothermal vent systems, where magmatic heat from the newly formed oceanic crust induces hydrothermal circulation of the seawater and deposition of metalliferous sediments (Hannington et al., 2005; German & Seyfried, 2014). The mid-ocean ridge metalliferous sediments, when compared to normal pelagic sediments, lack Al, Si and Ti, but are enriched in Ag, As, B, Ba, Cd, Cr, Cu, Fe, Hg, Mg, Mn, Ni, Pb, Tl, U, V and Zn (Boström & Peterson, 1966; Boström & Peterson, 1969; Fisher & Boström, 1969; Boström & Fisher, 1969; Boström et al., 1972; Cronan, 1972; Horowitz & Cronan, 1976).

More specifically, in the mid-ocean ridge segments, cold seawater penetrates the newly formed basaltic crust through fault zones, cracks and fissures created by the divergence of tectonic plates. As it circulates through the seabed, it comes in close proximity with the underlying mantle material and gets heated, with temperatures reaching as high as 400 $^{o}$C, while it becomes more acidic. As the heated water moves through the crustal ruptures, it reacts with the surrounding basaltic rocks, causing the leaching of metals such as Cu, Fe, Mn, Pb and Zn. This hot, sulfur- and metal-enriched hydrothermal solution gradually, due to buoyancy, reemerges to the seabed through vents, where hydrothermal activity is expressed. Mixing with the surrounding cold, usually oxygenated seawater, causes a series of chemical reactions that lead to the precipitation of dissolved minerals and inorganic sulfides, forming different types of hydrothermal vent structures, with the most recognizable being the black smokers (see Figure 1). Sulfides of Cu, Fe and Zn, sulfates of Ba and Ca, Fe and Mn oxides, as well as oxyhydroxide minerals (e.g., α-FeOOH, MnOOH) are the most common hydrothermal deposits in the global mid-ocean ridge, with metal concentrations depending on temperature, pH, chlorinity and redox conditions.

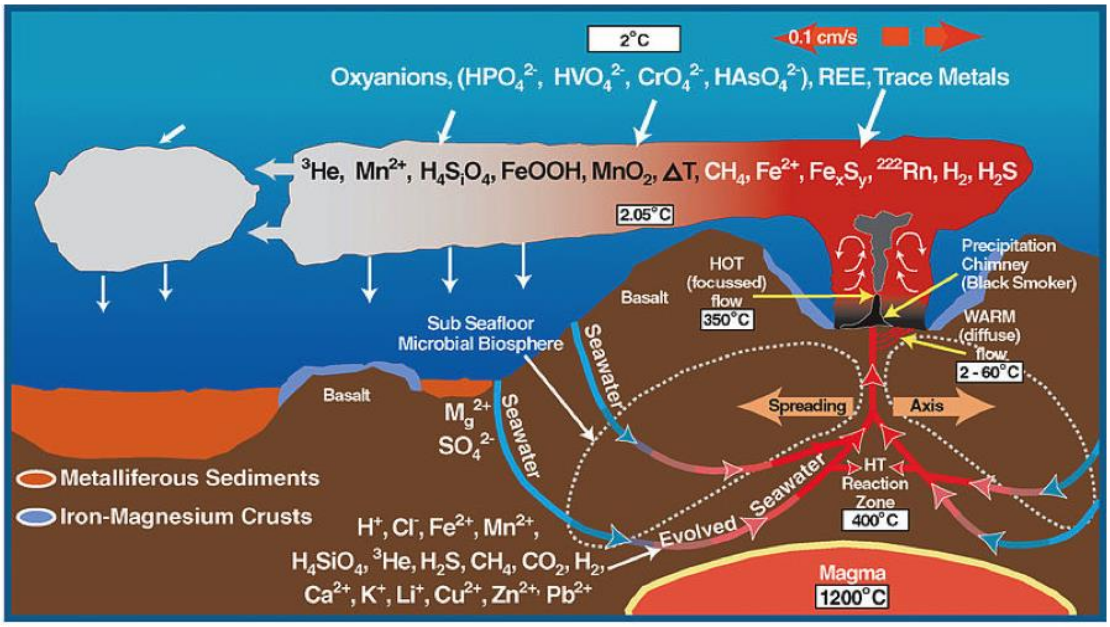


**Figure 2:** *Illustrative diagram of a hydrothermal vent system, featuring the circulation of hydrothermal fluid, the plume and the resulting deposits and precipitates. Volcanic heat at the global mid-ocean ridge axis drives hydrothermal circulation and chemical exchange between the ocean crust and seawater (Source: National Oceanic and Atmospheric Administration).*

In general, the distribution of hydrothermal activity is highly influenced by tectonism and magmatism. While hydrothermal vents have been discovered at all mid-ocean ridge segments, accounting for ~65% of all seafloor hydrothermal activity (Hannington et al., 2005), the spatial frequency, the depth at which hydrothermal fluids circulate and the size of hydrothermal ore deposits vary depending on the spreading rate of the various ridge segments (Baker & German, 2004; Hannington et al., 2011). In slow-spreading centers, the amount of metalliferous sediments appears to be larger than in fast-spreading centers, whereas vent sites along the axis increase with spreading rate (Fouquet, 1997).

Despite the inhospitable marine conditions, it has been discovered that unique species, mostly endemic, and lively ecosystems thrive around hydrothermal vents. These biological communities, instead of relying on sunlight and photosynthesis, depend on a chemical process known as chemosynthesis (Jannasch & Wirsen, 1979). This process is carried out by bacteria and archaea that convert $H_2S$ and other chemicals released by the vents into usable forms of energy, providing food for organisms at higher trophic levels such as clams, crabs, mussels, shrimps and tubeworms (Corliss et al., 1979; Harris, 2020).

The metalliferous ore deposits in the hydrothermal vents could potentially yield significant economic benefits. Deep-sea mining and mineral exploitation from the seabed is a recently developed industry driven by the urgent need to find more resources to meet the ever-growing demands, the diminishing land reserves and the rapid technological development. However, it is a challenging process due to both the difficulty in locating and accessing seafloor hydrothermal vents and the presence of fragile ecosystems in these peculiar environments (Hannington et al., 2011; German & Seyfried, 2014).

Therefore, submarine hydrothermal systems are extreme environments that could potentially hold great importance for the scientific community. Their study could provide information about the geological history of Earth and the existence of economically valuable metalliferous deposits, aid in the discovery of new molecules with therapeutical usage and even assist in space exploration (Farmer, 2000; Thornburg et al., 2010; Hannington et al., 2011).

## 2.2. Brine Pools

Deep-sea brine pools are among the most extraordinary and enigmatic environments nestled within the ocean. These peculiar habitats have captivated the scientific community due to their unique characteristics setting them apart from the surrounding water. Nevertheless, there is still limited knowledge regarding their precise formation mechanism, geochemical and physical properties, and ecology.

Brine pools are stable accumulations of dense hypersaline water settled in depressions on the seabed, ranging in size from a few meters to several kilometers, with their formation being a complex process influenced by the interplay of geological, hydrological and environmental factors. Brine pools exhibit remarkable variations in physico-chemical parameters compared to the overlying seawater, with distinct brine-seawater interfaces as documented by measurements from water samples and geophysical surveys (Hunt et al., 1967; Miller et al., 1966; Degens & Ross, 1970). These variations usually include elevated salinities (up to ~370) and temperatures (up to ~68 ºC), reductions in pH and oxygen levels, and metal enrichment (Antunes et al., 2011; Laurila et al., 2014b).

Brine-filled sub-basins are relatively rare and have only been recorded in a few regions, including the Mediterranean Sea (e.g., Tyro and Bannock sub-basins), the Gulf of Mexico (e.g., Orca sub-basin) and, most notably, in the Red Sea (e.g., Atlantis II Deep, Discovery Deep, Kebrit Deep) (Degens & Ross, 1969; Addy & Behrens, 1980; De Lange et al., 1990). The shared characteristic among the previous three major marine basins is the presence of salt deposits in their sedimentary record, which is a key factor in the development of brine pools, with salt tectonics being the primary process contributing to their formation (Hunt et al., 1967; Craig, 1966; Backer & Schoell, 1972; Cita, 2006). In the past, the three aforementioned basins were cut off from the global ocean and, eventually, dried out, which led to the deposition of evaporites. When their connection with the open ocean was restored, typical (mainly) pelagic sediments accumulated on top of these salt deposits. The sediment overburden, finally, became excessive and led to salt flows and diapirism that moved upwards through the overlying sediments towards the seafloor. Then, plate movement and faulting resulted in the deformation and fracturing of the evaporitic deposits, creating pathways for seawater to infiltrate into the sediments and dissolve soluble salts and minerals, creating highly dense fluids. When the hypersaline water emerged, it filled restricted depressions on the seafloor and, subsequently, was sunk and accumulated into the deeps, since it was denser than the ambient seawater, forming a brine pool (e.g., see Atlantis II Deep in Figure 2).

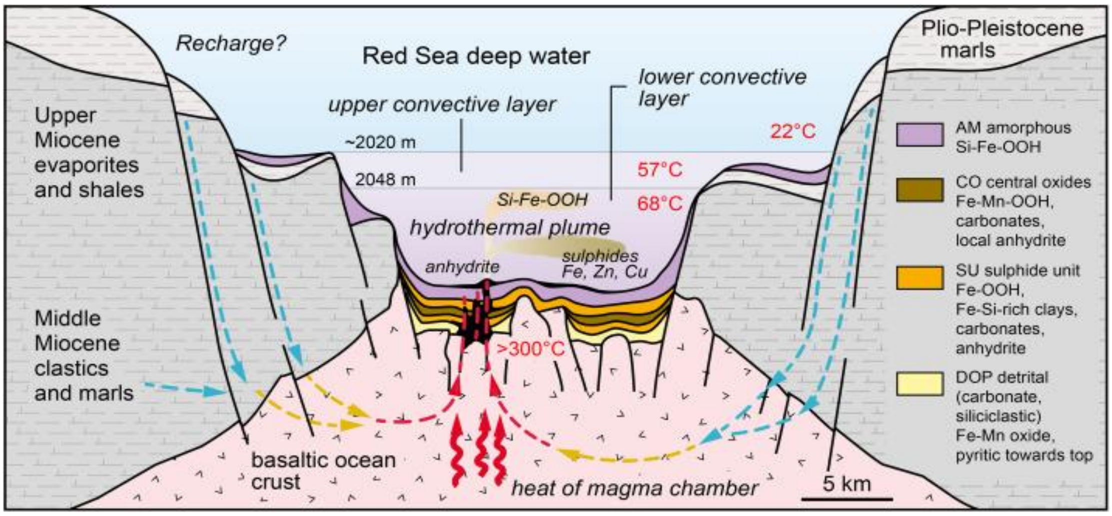


**Figure 2:** *Schematic cross-section of the brine in the Atlantis II Deep (Red Sea), showing the geological setting, sedimentary strata and the two main stratified brine layers (Barrett et al., 2021).*

Alternatively, another process contributing to the formation of hot brine pools is the hydrothermal activity occurring along the global mid-ocean ridge (Degens & Ross, 1969; Harris, 2020). In the mid-ocean ridge, seawater, in addition to the evaporitic strata, penetrates the newly formed basaltic oceanic crust and comes in close vicinity with the underlying magma, heating up and becoming enriched in minerals (Modenesi

& Santamarina, 2022). This highly dense hydrothermal solution discharges into seabed topographic depressions that act as morphological traps, leading to the formation of submarine brine pools. As the hot, dense fluid undergoes cooling, minerals begin to precipitate within the brine, forming metalliferous ore deposits (Scholten et al., 1991).

Finally, cold brine pools have been formed at both passive continental margins and subduction zones, and they are often associated with hydrocarbon seeps (Degens & Ross, 1969; Duarte et al., 2020; Harris, 2020).

Although it was initially speculated that brine pools were sterile environments, due to their extreme physicochemical conditions, it was later discovered that they were, in fact, oases of life hosting unique life forms of high ecological significance. For instance, the discovery of extremophile microbes within the inhospitable environment of the brines and their adaptation mechanisms set new limits to the understanding of life on Earth (Mapelli et al., 2017).

# 3. MICROFOSSILS

Fossils serve as the most important witnesses to the Earth's geological history, as they clearly reveal its evolutionary progression. Microfossils are typically found embedded in sediments, primarily in marine environments, but also in lacustrine, brackish and terrestrial settings, and are characterized by their relatively small size and high abundance. The most notable groups of microfossils include coccolithophores, foraminifera, diatoms, radiolaria and dinoflagellates. They serve as paleoenvironmental indicators, aiding in the understanding of the conditions that prevailed during the depositional period by correlating ancestral forms with present-day species, and are also used to determine the absolute age of the strata in which they are found.

## 3.1. Foraminifera

Foraminifera are classified within the kingdom of *Chromista*, subkingdom of *Rhizaria*, phylum of *Retaria* and infraphylum of *Foraminifera* (Cavalier-Smith, 2018). Their evolutionary history traces back to Early Cambrian (Culver, 1991) and possibly even earlier throughout the Neoproterozoic Era (Pawlowski et al., 2003). There are more than 40,000 extinct species, while the ~10,000 living species establish foraminifera as the most diverse living organisms in the ocean to date (Cavalier-Smith, 2018).

Foraminifera are single-celled, eukaryotic, heterotrophic organisms, with heterophasic life cycle, characterized by alternating phases of asexual and sexual reproduction (Goldstein, 1997). They consist of protoplasm that forms a network of pseudopods aiding in movement and food intake (Sen Gupta, 1999). The majority of foraminifera produce a shell (test) with one or more chambers, composed mostly of calcium carbonate ($CaCo_3$) or sediment particles glued together (agglutinated) to protect the organism. Shell sizes vary from 100 to 500 μm, however, large benthic foraminifera can reach sizes up to 20 cm. Their classification is based on the wall structure of the test (hyaline, porcelaneous, agglutinated), the number of chambers (monothalamous, polythalamous) and the morphology of the test (coiling, chamber arrangement and form, aperture system) (Holbourn et al., 2013).

Foraminifera inhabit all aquatic ecosystems, from the poles (Dieckmann et al., 1991) to the equator (Reghellin et al., 2015). They are abundant in the ocean, but are also found in brackish and freshwater environments (Siemensma et al., 2017). They are classified as planktonic, living along the water column, or benthic, residing in the seafloor, either on the surface of the seabed (epifauna) or within the sediments (infauna) (Figure 3).

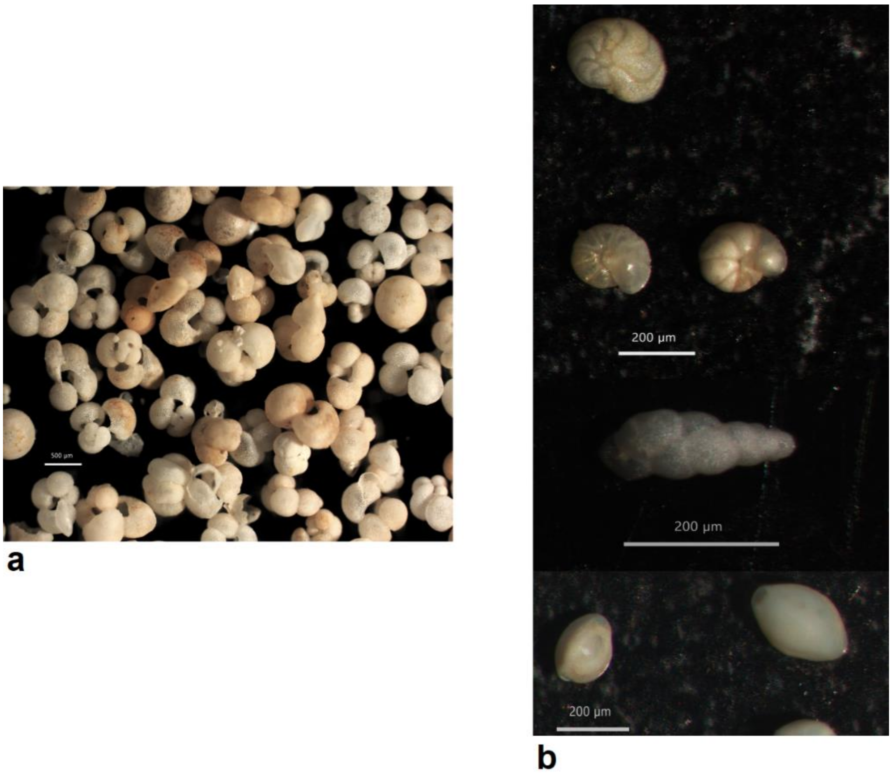


**Figure 3:** *Foraminiferal tests a: planktonic species, b: benthic species.*

Foraminifera's significance in paleoenvironmental research is based on their high abundance and wide spatial distribution as well as on the durability of their shells. Additionally, their short lifespan combined with their rapid response to environmental changes qualifies them as suitable indicators for the reconstruction of paleoenvironments. Characteristic species of foraminifera are also used in biostratigraphy. The contribution of foraminifera to the biogeochemical cycle of carbon is remarkable, producing an annual amount of $CaCO_3$ estimated at ~1.4 billion tons, accounting for ~25% of the global ocean carbonate production (Langer, 2008), and providing significant inputs to biogenic carbonate sedimentation.

### 3.2. Benthic Foraminifera

Benthic foraminifera are highly important palaeoecological indices because the prevailing environmental conditions are reflected in their shells. Various biotic and abiotic factors, such as $CaCO_3$ availability, seafloor oxygenation, water temperature, turbidity, light, depth, sediment type, ocean currents, salinity, alkalinity (pH) and food-nutrient availability, influence foraminiferal diversity and abundance. For instance, temperature affects the shape and size of their shells, with studies showing that higher temperatures lead to larger shell sizes (Frerichs, 1970). Additionally, shell composition is affected by the availability of $CaCO_3$, which, in turn, is influenced by water salinity and sea temperature.

Benthic foraminifera microhabitat (penetration depth in sediments) strongly depends on oxygen levels and food availability, as described in the Trophic Oxygen (TROX) model (see Figure 4; Jorissen et al., 1995; Sen Gupta, 1999). Specifically, in well-oxygenated and oligotrophic environments, benthic foraminifera assemblages are predominantly composed of epifaunal taxa, whereas dysoxic and eutrophic environments are primarily dominated by infaunal species (Figure 4*)*. Therefore, the distinction between benthic foraminifera microhabitats serves as indicators of oxygen level and food availability.

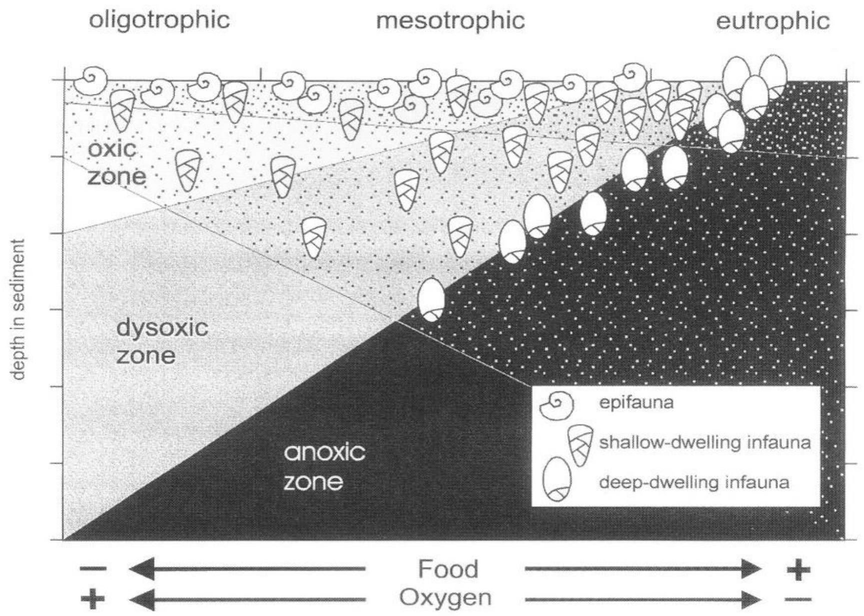


**Figure 4:** *The TROX model showing variations of the benthic foraminifera microhabitat depth, according to food availability and oxygen concentration (Jorissen et al., 1995; Sen Gupta, 1999).*

The response of benthic foraminifera to environmental changes, reflected in their abundances, diversity and shell morphology (dwarfism, test abnormalities), establishes them as one of the most suitable indicators of paleoclimate, paleoceanography and ecological disturbances.

In a plethora of studies, foraminifera have contributed to the determination of the relative and absolute age of sedimentary deposits through biostratigraphy (Zambetakis-Lekkas et al., 1998; Groves et al., 2003; Bugrova, 2020) and the method of $^{14}C$ dating in the shells of planktonic species, respectively. Furthermore, foraminifera provide insights into sea level changes (Cosentino et al., 2017; Triantaphyllou et al., 2021), salinity variations (Pérez-Asensio & Rodríguez-Ramírez, 2020) and temperature fluctuations through the study of the stable isotope ratios of $\delta^{18}O$ (Waelbroeck et al., 2002) and $\delta^{13}C$ (D'haenens et al., 2012), as well as via the analysis of trace element ratios (e.g., Mg/Ca, Sr/Ca) measured from their shells (Rosenthal et al., 1997). Additionally, they have aided in the determination of paleodepths and paleotectonics

(Frerichs, 1971) and even in the discovery of hydrocarbons (O'neill, 1996). Moreover, the use of the Low Oxygen index contributes to the identification of variations in the concentration of dissolved oxygen at the seabed (Sen Gupta & Machain-Castillo, 1993). Finally, foraminifera serve as bioindicators of water quality and environmental stress, allowing the monitoring of human-induced pollution (Frontalini & Coccioni, 2008; Dimiza et al., 2016 Martins et al., 2016; El-Kahawy et al., 2018).

# 4. STUDY AREA

## 4.1. Red Sea

The unique environment of Red Sea (Figure 5) has attracted the attention of many scientists over the last few decades. Its name is most likely derived from seasonal algal blooms of the cyanobacterium *Trichodesmium erythraeum*. The Red Sea geotectonic regime along with the abnormal marine conditions recorded, as well as its paleoenvironmental and historical significance, have resulted in numerus studies regarding its evolution.

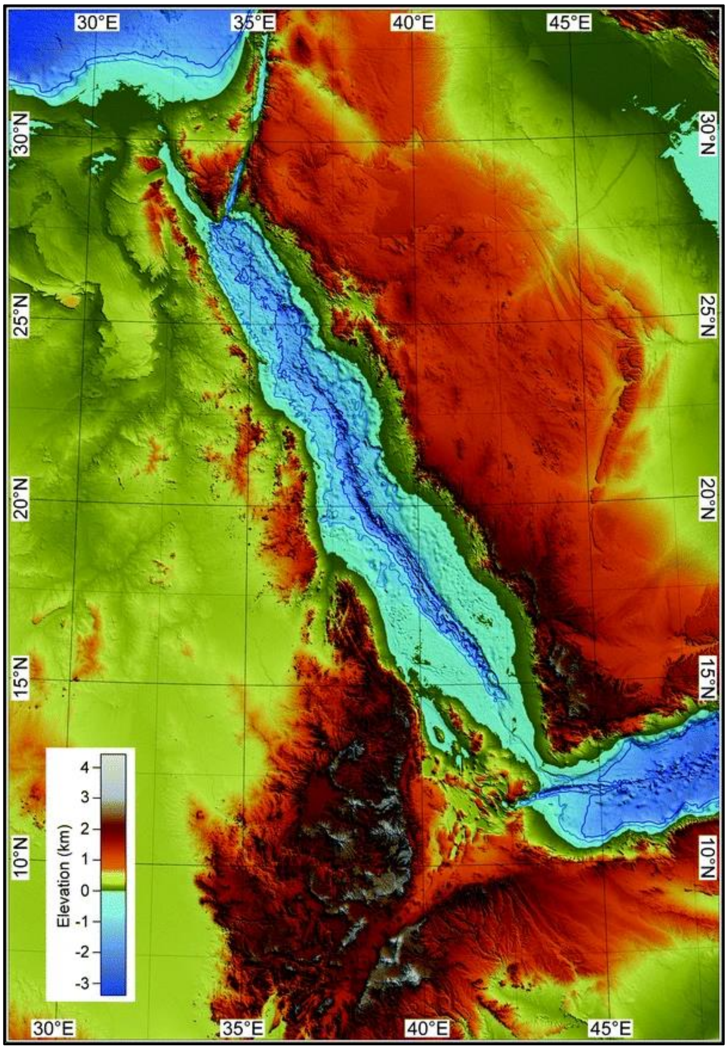


**Figure 5:** *Topographic and bathymetric map of Red Sea (Rasul et al., 2015).*

Red Sea is an elongate, marginal, semi-enclosed sea located between NE Africa and the Arabian Peninsula, stretching from 30° N to 12.5° N in a NW-SE direction (Xie et al., 2019). The Red Sea region is surrounded by seven countries, making its management and exploration challenging to joint research activities. It has a length of ~2000 km, a maximum width of ~355 km, covering an area of 458,620 $km^2$ (Rasul et al., 2015). Its average depth is 524 m (Sofianos & Johns, 2015), with the maximum depth reaching ~3000 m at the Suakin Trough in the central Red Sea (Saada et al., 2021). Red Sea accommodates several islands formed by corals (such as the Farasan Islands and Dahlak Islands), volcanic material (such as the Hanish Islands and Zubair Islands), sand deposits or continental fragments (Rasul et al., 2015). At its northern end, ~28° N near Ras Mohamed (Sinai Peninsula), Red Sea splits into the Gulf of Aqaba to the northeast and the Gulf of Suez to the northwest (where the Suez Canal provides a connection with Mediterranean Sea). In the south, Red Sea is connected to the Gulf of Aden and, consequently, to the Arabian Sea and Indian Ocean through the straits of Bab al-Mandab (Rasul et al., 2015).

Both African and Arabian coastlines surrounding the Red Sea are mostly linear at latitudes northern of 24°, while southern the geometry changes to curvilinear, exhibiting high elevations across the Arabian Peninsula and in the southern part of African margin (Bosworth, 2015). Based on bathymetry (Figure 5), Red Sea can be divided in three main depth zones: (i) the shallow shelves with less than 50 m depth; (ii) the deep shelves with depths between 500 to 1000 m; and (iii) the central rift zone with depths ranging from 1000 to 3000 m (Saada et al., 2021).

Red Sea is a restricted basin isolated from the open ocean, located in a hot arid climate zone, with very low humidity, exchanging water solely with the Indian Ocean via the narrow and shallow straits of Bab-al-Mandab, configured by a sill at a depth of 137 m

(Werner & Lange, 1975). In addition, the lack of any permanent river discharges and minimal precipitation (10-200 mm·yr$^{-1}$) has resulted in a negative hydrological budget (Morcos, 1970), characterized by high evaporation rates estimated at 2.06 ± 0.22 m·yr$^{-1}$, thus, making Red Sea a highly dense body of water (Sofianos et al., 2002). Therefore, the hydrodynamics in the Bab-al-Mandab straits as well as the regional climate are responsible for the extreme marine conditions (Edelman-Furstenberg et al., 2009), demonstrating sea surface salinities up to 40 in the northern Red Sea (Edwards, 1987) and mean sea surface temperatures of 25.11 ± 0.62 °C during winter and 30.28 ± 0.62 °C during summer (Shaltout, 2019). An example of the extreme conditions prevailing in Red Sea is the occurrence of aplanktonic stratigraphic intervals in sediments deposited during glaciation periods, suggesting salinities beyond planktonic foraminiferal tolerance limit (Fenton et al., 2000).

The water mass circulation regime of Red Sea is mostly driven by thermohaline-forcing and wind-forcing seasonal changes (Chung et al., 1982). The wind field in Red Sea is controlled by the Mediterranean climate system over the northern part of the basin, whereas the central and southern parts are influenced by the Indian monsoonal system (Pedgley, 1974). At latitudes northern than 19° N, the prevailing wind comes from NW throughout the year, while southern of this latitude the wind reverses its direction from NW-SE during summer to SE-NW during winter (Patzert, 1974; Pedgley, 1974). Due to the atmospheric circulation in the winter, low-salinity surface water from the Gulf of Aden enters the Red Sea flowing northwards, becoming gradually denser due to evaporation, and, eventually, sinking at the northern part of the basin. Then, it returns southwards as deep, high-salinity water mass, exiting the Red Sea through the Bab al-Mandab straits. Hence, a typical anti-estuarine circulation pattern predominates. On the other hand, in summer, due to the reversal of the wind field, Red Sea surface water flows southwards exiting the Red Sea, while a subsurface inflow from the Gulf of Aden enters the Red Sea, resulting in an upwelling to the north (i.e., estuarine circulation) (Patzert, 1974; Murray & Johns, 1997; Sofianos & Johns, 2015).

Red Sea is an oligotrophic basin, especially its northern part, where nutrient supply - because of the absence of any river discharges - is mostly affected by the water exchange through the Bab al-Mandab straits (Edelman-Furstenberg et al., 2009; Triantafyllou et al., 2014).

As a semi-enclosed basin, Red Sea has been highly affected by climatic variabilities and sea-level changes that occurred during Quaternary, as revealed by fauna and floral assemblages found on sediments, which indicate extreme marine conditions and palaeoceanographic changes (Thunell et al., 1988; Almogi-Labin et al., 1991; Fenton et al., 2000; Edelman-Furstenberg et al., 2009). For instance, isotopic measurements on microfossils have shown higher salinities during glaciation periods, when connection with the Indian Ocean was limited (Berggren, 1969). Additionally, laminated sediments deposited at 15-4 ka signify seasonal variations in productivity as a response to changes in seawater circulation patterns, stratification of the water column and, thus, nutrient availability, with summer productivity being indicated by light-colored coccolith-rich layers, whereas fall and winter flux is evident by dark diatomaceous laminations (Seeberg-Elverfeldt et al., 2004).

Red Sea is a juvenile oceanic basin, formed at the divergent boundary between the African (Nubian) plate to the west and the Arabian plate to the east (Figure 6), which moves to a NE direction (Rasul et al., 2015).

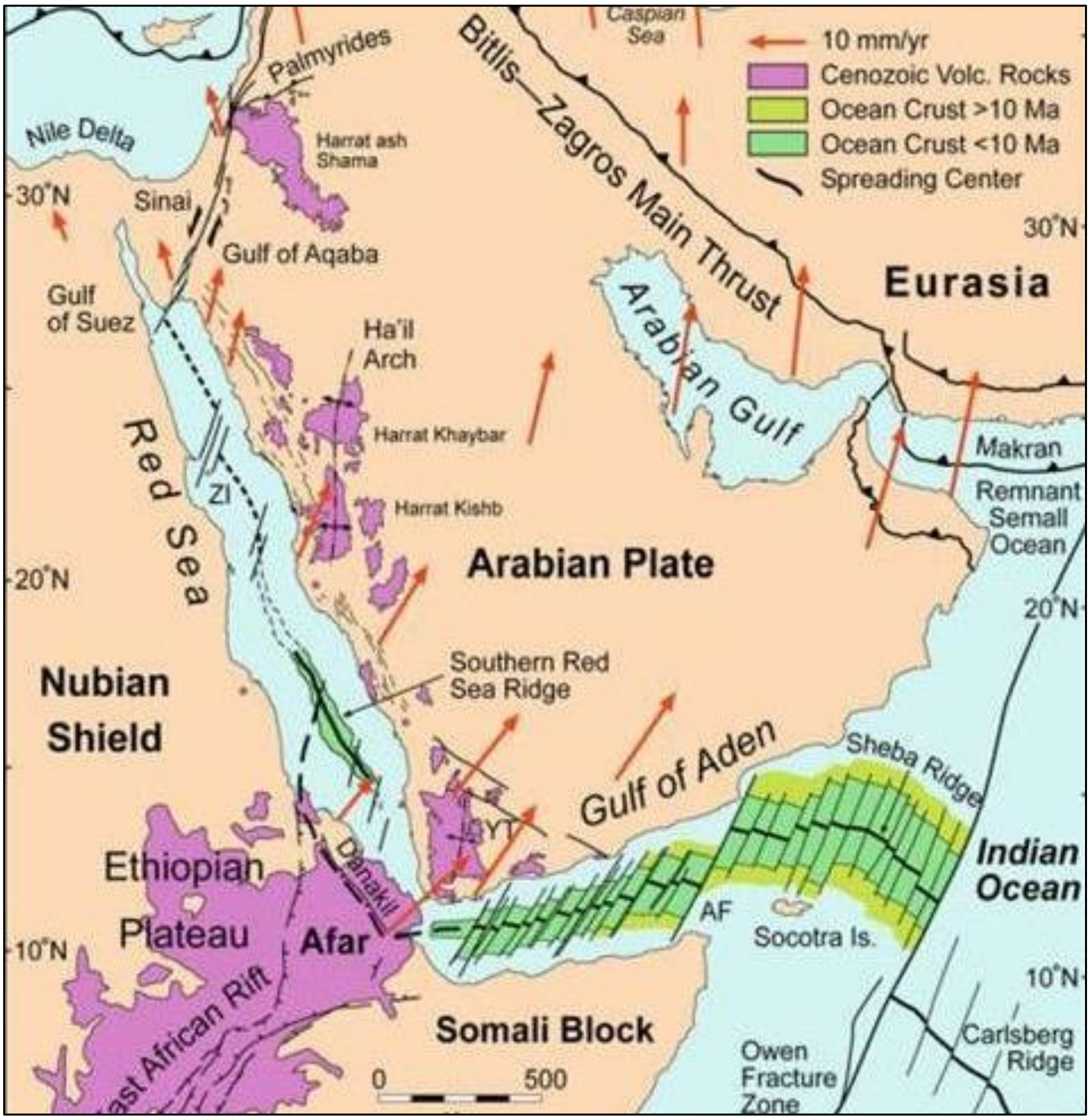


**Figure 6:** *Main tectonic features of the Red Sea Rift system (Bosworth, 2015).*

Different stages of crustal evolution are visible in the region, from the rupture of continental lithosphere (i.e., East African Rift) to the emplacement of new oceanic crust (i.e., Gulf of Aden and southern Red Sea) (Bonatti et al., 2015). Therefore, Red Sea is the most prominent example of the transition from continental rifting to seafloor spreading, being part of an extensive rift system stretching from Dead Sea to Mozambique (Bosworth, 2015), where three main tectonic plates, i.e., African (Nubian), Arabian and Somalian, are drifted apart defining the geodynamic regime of the area (Mckenzie et al., 1970). Another microplate is located in the SW part of the Red Sea, i.e., the Danakil plate (Monin et al., 1982). Apparently, the boundaries of the aforementioned plates are characterized by seismic activity, while their meeting point is located at the southernmost edge of Red Sea (Mckenzie et al., 1970).

The Red Sea Rift, and by extension the Danakil Rift, meet with the East African Rift and the Asal Rift at the so called Afar Triangle (i.e., the Afar triple junction; see Figure 6), which is considered to be the initiation point of the rifting process (Bonatti et al., 2015). The Asal Rift extends eastwards into the Tajura Rift and farther into the Gulf of Aden Rift and the Sheba Ridge, reaching, eventually, the Owen fracture zone in Indian Ocean. Northwards, the Red Sea Rift is connected via the Gulf of Aqaba - Levant transform zone with the Bitlis – Zagros convergence zone (Monin et al., 1982; Rasul et al., 2015).

According to isotopic dating ($^{40}Ar/^{39}Ar$ radiometric dating on igneous rocks), the onset of continental rifting in Red Sea, has most probably taken place during Early Oligocene at ~30 Ma (Zumbo et al., 1995; Ukstins et al., 2002). Bosworth et al. (2005) and Bosworth (2015) configured the Red Sea evolution from continental rifting to seafloor spreading into several phases (see Figure 7): (1) The onset of rifting was established by basaltic and rhyolitic volcanism, related to the Afar plume impinging continental lithosphere, which was initiated at 31-30 Ma in the Afar region and SW Yemen and propagated to the north in the western Saudi Arabia; (2) Marine syn-tectonic sediments were deposited between 29.9-28.7 Ma on rifted continental crust in the central Gulf of Aden; (3) Marine syn-rift sediments were also deposited offshore Eritrea at 27.5-23.8 Ma, concurrently with the formation of a small rift basin in the area, while at Late Oligocene (25 Ma) extension and rifting began in Afar; (4) A second stage of volcanism was established across the entire Red Sea region at 24-23 Ma, with basaltic dike intrusions and layered gabbro and granophyre flows, followed by rift-normal extension, with rift shoulder uplift and rapid syn-rift subsidence at ~20 Ma; (5) Seafloor spreading first started at 19-18 Ma at the Sheba Ridge and probably reached the central Gulf of Aden by ~16 Ma;

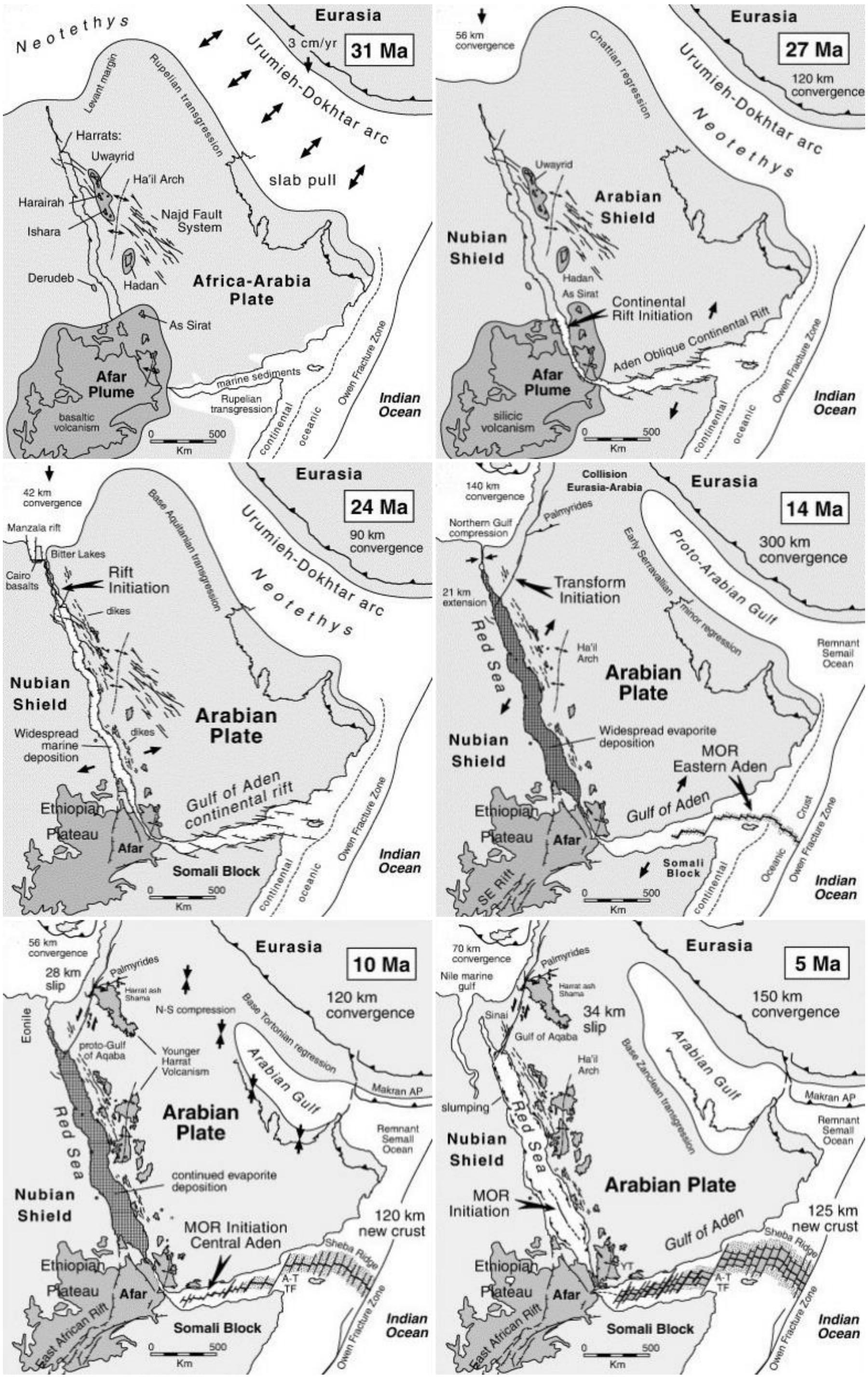


**Figure 7:** *Palinspastic restoration of the Red Sea – Gulf of Aden Rift system (Bosworth et al., 2005).*

(6) During the time of the collision between Arabian and Eurasia plates, at ~14 Ma, the Aqaba-Levant transform fault cut through the continental crust of the northern Arabian plate, thus, connecting the northern Red Sea with the Bitlis-Zagros convergence zone.

This event shifted the Red Sea's extension from normal rifting to highly oblique rifting, parallel to the Aqaba-Levant transform fault. At the same time, during the Middle Miocene, the Red Sea connection with Mediterranean Sea became restricted, resulting in a shift in the Red Sea sedimentation from open marine to evaporitic conditions. The deposition of enormous evaporites, primarily halite (up to 3 km thick), led to salt diapirism throughout Red Sea. In addition, basaltic volcanism resumed in the northwest Arabian Peninsula and continued until recently; (7) Oceanic spreading propagated from the central part of Gulf of Aden westward to the Shukra al Sheik fracture zone at 10 Ma; (8) The onset of seafloor spreading started shortly after in the southern Red Sea at ~5 Ma. This event coincides with an unconformity observed at the top of the evaporitic strata deposited during Miocene throughout the entire basin and by the re-establishment of open marine conditions. Currently, the Red Sea spreading center is propagating towards the north, even though the extent to which oceanic crust has spread is debatable.

The main lithostratigraphy of Red Sea (see Figure 8) remains largely consistent along its northern and southern margins. The Red Sea crystalline basement is formed by Neoproterozoic rocks (Bosworth et al., 2005; Stern & Johnson, 2019). Pre-rifting sedimentation, spanning from Early Paleozoic to Early Oligocene, led to the deposit of sandstorm, carbonates and shale. Early Miocene is characterized by syn-rift sedimentation, marked by the presence of Globigerina marl, sandstone and carbonate strata, whereas during the Middle to Late Miocene, when the Red Sea water influx was restricted, thick evaporates (i.e., halite, anhydrite and gypsum) were deposited. Overlying these sediments, over the last 5 Ma, Plio-Pleistocene biogenous and terrigenous sediments have been deposited (Monin et al., 1982), with clastic sediments (sandstone, shales) and carbonates signifying the re-establishment of open marine conditions (Bosworth et al., 2005; Bosworth, 2015).

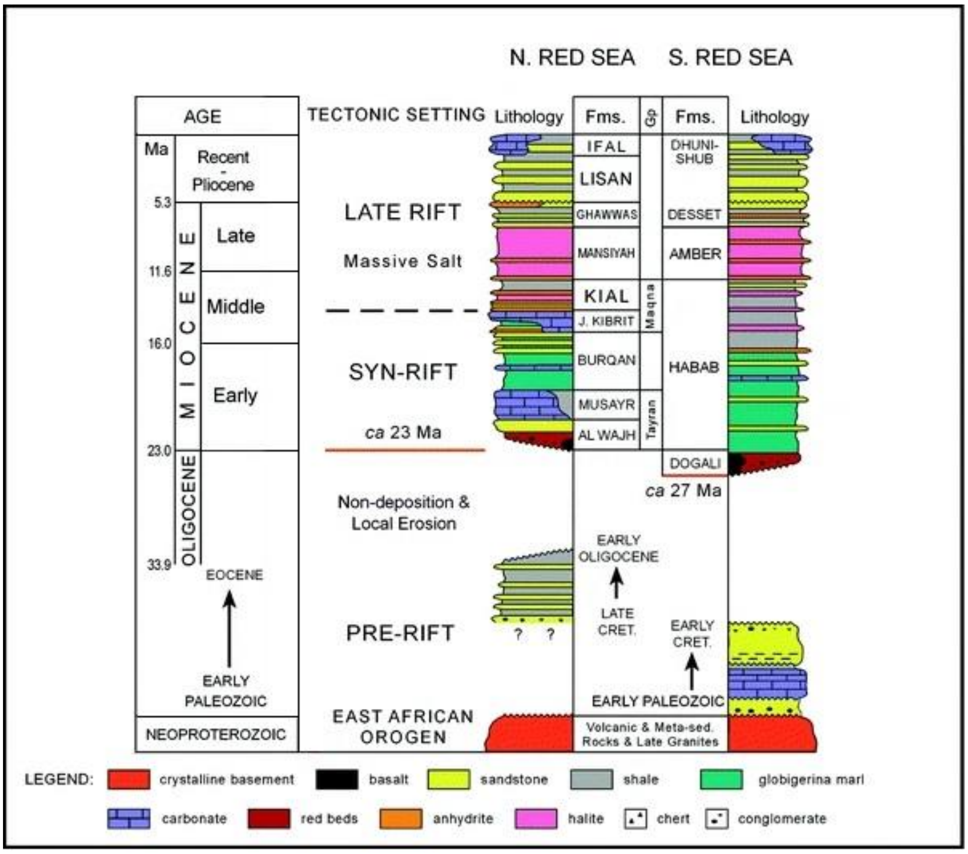


**Figure 8:** *Main stratigraphic sections of northern and southern Red Sea (after Bosworth, 2015).*

## 4.2. Red Sea Rift

The divergence of the Arabian and Nubian plates gave rise to the formation of the Red Sea Rift valley and the generation of new oceanic crust along the rift axis (Bonatti, 1985). Seafloor spreading in Red Sea is generally very slow, with present spreading rates increasing southward, ranging from about $0.9 \pm 0.1$ $cm \cdot yr^{-1}$ in the northern Red Sea to $1.5 \pm 0.05$ $cm \cdot yr^{-1}$ in the central and southern parts of the basin, reaching a peak of ~1.6 $cm \cdot yr^{-1}$ at 18° N (Chu &s Gordon, 1998; DeMets et al., 2010).

The narrow axial trough, developed within the rift valley, is a steep-sloped depression with irregular morphology and water depths ranging from 1000 to ~3000 m in some deeps, with depth decreasing from the central Red Sea towards the north and south parts (Coleman, 1974; Nawab, 1984; Delaunay et al., 2023). Along the axial trough, the occurrence of tholeiitic basalts and extrusive volcanic features, including pillow lavas, lava flows and pyroclastic rocks, indicates an analogue to the global mid-ocean ridge environments (Young & Ross, 1974; Monin et al., 1982). The presence of volcanic, seismic and hydrothermal activity along with newly formed basaltic intrusions provides evidence of on-going seafloor spreading (Coleman, 1974; Rasul et al., 2015).

Along the rift valley, sediments are unevenly distributed and their thickness increases with distance from the axial trough (Monin et al., 1982). The oceanic seafloor is only exposed at the axial rift, and at certain deeps, whereas elsewhere the basement is either covered by allochthonous Miocene evaporitic layers, due to salt diapirism and rift tectonics, or buried under younger pelagic sediments (Heaton et al., 1995; Delaunay et al., 2023). Consequently, the interpretation of magnetic and gravity data is equivocal, and is, thus, difficult to determine the nature (continental vs. oceanic) of the underlying crust (Izzeldin, 1987; Augustin et al., 2021).

In accordance with the stage of rifting from continental to oceanic, Red Sea can be divided into three sectors, i.e., the northern (north of 24° N), central (from 24° N to 19° N) and southern one (south of 19° N) (Bonatti, 1985). In the southern Red Sea, high heat flow, positive gravity (up to 259 mGal) and strong magnetic (-237 to 211 nT) anomalies indicate active oceanic spreading with emplacement of newly formed oceanic crust. This region features a well-developed and continuous axial trough that has been developed over the last ~5 Ma (Cochran, 1983; Bonatti, 1985; Saada et al., 2021), accompanied by extensive volcanism and seismic activity (Bonatti et al., 2015). Moving to the central sector of the Red Sea rift zone, as shown by magnetic and gravity data, this area is characterized as a transitional zone, where the axial trough is intermittent, seafloor spreading is discontinuous and oceanic crust is limited in isolated deeps along the basin axis, with the deeps being separated by shallower inter-trough zones (Bonatti et al., 2015; Saada et al., 2021). The deeps are considered as the initiation points of drifting and may also exhibit hydrothermal activity (Bonatti, 1985). According to geophysical data, the inter-trough zones lack strong magnetic anomalies, have lower gravity values than the deeps and are, thus, may be interpreted as stretched continental crust (Bonatti et al., 2015). Nevertheless, the actual extent of oceanic crust remains unknown, as sediments cover most of these inter-trough zones, while a few studies argue that the magnetic anomalies observed beyond the deeps could be interpreted as the result of lava flows and dikes (LaBrecque & Zitellini, 1985; Rasul et al., 2015). In the northern sector of the basin, the absence of an axial trough and the presence of only a few scattered deeps (with oceanic crust) suggest a late-stage rifting (Cochran, 1983; Bonatti, 1985). Additional evidence of underlain continental crust is the absence of magnetic and gravity anomalies, except for a few isolated higher magnetic anomalies within the deeps (Cochran, 1983; Saada et al., 2021). However, similarly to the central sector, the nature of crust is unclear due to the overlying sediments (Rasul et al., 2015), even though some studies suggest, based on the juxtaposed Red Sea shoreline, that oceanic crust is present along the entire Red Sea (Stern & Johnson, 2019).

In the 1880s, reports of extreme temperatures and salinities at great depths in Red Sea piqued scientific interest. Decades later, during the Albatross Expedition in the late 1940s, researchers once again encountered indications of high temperature and salinity anomalies in the central Red Sea, thus, performing a series of research cruises in the following years (Degens & Ross, 1970). Eventually, it was discovered that hot, dense, anoxic brines, with acidic water and sediments enriched in heavy metals, such as Cu, Fe, Mn and Zn, were located at some of the isolated deeps along the axial zone in the central and northern Red Sea (Miller et al., 1966; Hoffmann, 1991). These deeps (Figure 9), filled with saline hot water, constituted the first geochemical evidence of hydrothermal venting on the seafloor and, given that Red Sea serves as an archetypal rifting ocean basin, it was speculated that similar phenomena could also be observed in spreading centers of the global mid-ocean ridge (Degens & Ross, 1969).

In the last few decades, through the systematic exploration of Red Sea, more than 20 brine-filled deeps (Figure 9) have been found out, with their formation being associated with seafloor spreading, hydrothermal activity and salt deposits. Most of these brines are located at the intersection of transform faults with the axial rift zone (Nawab, 1984), however, recently cold brines were also discovered beyond the Red Sea central axis, at the shelves near the Saudi Arabian coastline (Thuwal Seeps) (Batang et al., 2012) and north of the Farasan Islands (Afifi brine) (Duarte et al., 2020) as well as at the Gulf of Aqaba (NEOM brine pools) (Purkis et al., 2022).

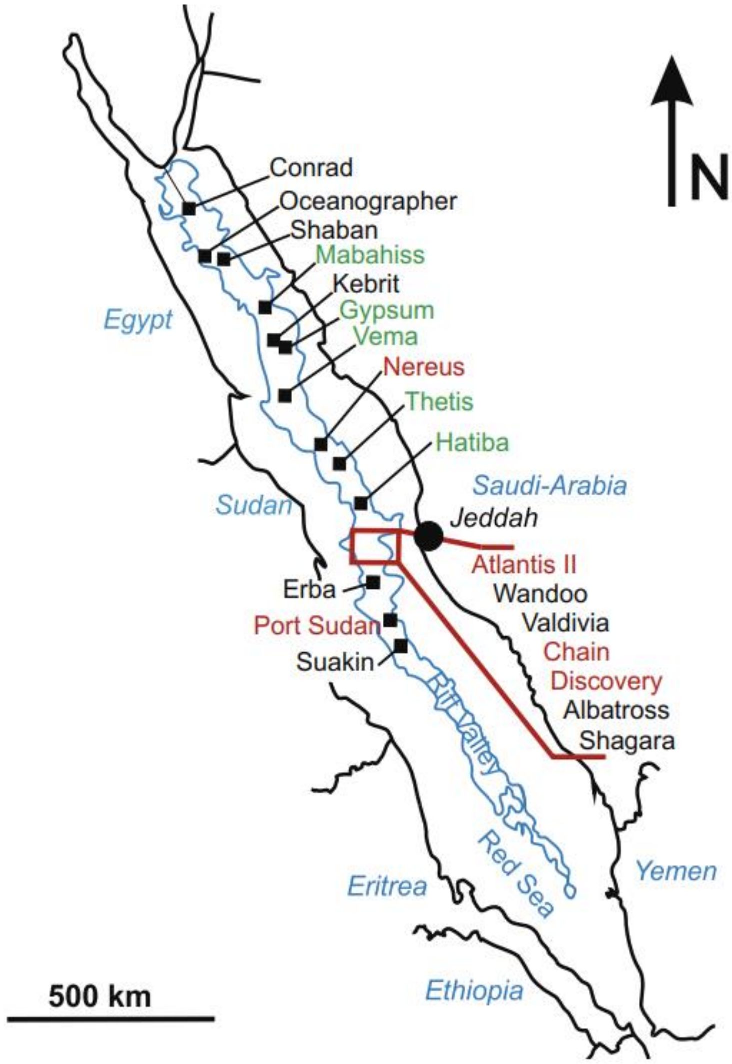


**Figure 9:** *Location of the main brine pools in the axial trough of Red Sea. Deeps containing hot brine (>30 °C) are marked in red, whereas deeps without brine are marked in green (Laurila et al., 2014a).*

The Red Sea brine pools originate from the dissolution of the underlying Miocene evaporites, which sometimes outcrop on the deeps' flanks, resulting in salinities up to ten times higher than those of the Red Sea Deep Water (Miller et al., 1966; Ross et al., 1973). The thickness of the brines is controlled both by the amount of leaching salt and by the diffusion processes at the seawater-brine interface (Anschutz et al., 1999; Seeberg-Elverfeldt et al., 2004). The brines display variations in their temperature and chemical composition as well as in the mineralogy of their metalliferous sediments. According to isotopic studies, their composition is affected by regular seawater, leaching of the Miocene evaporites and hydrothermal circulation through the Red Sea Rift - related basalts (Zierenberg & Shanks, 1988). The presence of hot brine pools, metalliferous deposits and excess of Cl in the occurring basalts indicate distinct hydrothermal venting in the Red Sea Rift zone (van der Zwan et al., 2019). However, some of the brines exhibit temperatures similar to those of the Red Sea Deep Water (e.g., Suakin Deep, Thuwal Seeps), while in some deeps there are metalliferous sediments without the presence of brine (e.g., Thetis Deep). Further, fragments from inactive black smokers have been recovered from the Kebrit Deep (Blum & Puchelt, 1991). Therefore, all previous cases could potentially indicate past occurrences of hydrothermal activity (Scholten et al., 1991; Gurvich, 2006; Pierret et al., 2010; Batang et al., 2012).

Hydrothermal circulation through the underlying basaltic rocks in the Red Sea Rift results in mineral-enriched fluids. As this hydrothermal solution vents into the brine, the metals eventually precipitate within the brine forming hydrothermal metalliferous sediments, which vary depending on the chemical characteristics of each brine (Modenesi & Santamarina, 2022). In general, these metalliferous deposits are enriched in Fe and Mn oxides and oxyhydroxides (e.g., goethite, hematite, lepidocrocite, magnetite), Fe and Mn carbonates (e.g., rhodochrosite, siderite), metal sulfides (e.g., pyrite, sphalerite, chalcopyrite), Fe-silicates and sulfates (e.g., anhydrite) (Miller et al., 1966; Ikpeama et al., 1974; Anschutz et al., 1990; Anschutz et al., 2000; Dekov et al., 2007; Barrett et al., 2021). The largest and most well-studied brine is the Atlantis II Deep, located in the central Red Sea sector (see Figures 9, 10). It contains the greatest present-day hydrothermal ore deposits on the seafloor, with metalliferous sediments up to ~90 million tons, enriched in Ag, Au, Co, Cu, Fe, Mn, Pb and Zn (Guney et al., 1988; Anschutz et al., 2000). With an estimated value of metal reserves (i.e., Zn, Cu, Ag and Au) of ~$11 billion, the Atlantis II Deep mining appears to be an extremely lucrative opportunity (Brueckmann et al., 2017). Finally, except from the metalliferous sediments, organic-rich sediments have also been found in some of the brines, mostly in the northern Red Sea (Kebrit and Shaban deeps) (Botz et al., 2007).

While it was initially thought that no organism could possibly survive in such a hostile environment (Watson & Waterbury, 1969), it was later revealed that Red Sea brines are, in fact, blooming hypersaline ecosystems with immense microbial communities. Several extremophile bacteria and archaea, even from new taxonomic groups, thrive in these harsh physico-chemical conditions (Eder et al., 2002; Antunes et al., 2011; Adel et al., 2016). However, the biodiversity of these extreme habitats is not limited to microorganisms. For instance, benthic macrofauna (such as sea anemones, polychaetes, hydroids, gastropods and top-snails) associated with the brine pool has been found at the brine-seawater interface in the Kebrit Deep (Vestheim & Kaartvedt, 2016). Additionally, evidence of animal activity (animal mounds most probably formed by polychaete worms) has been observed inside the Atlantis II Deep (Young & Ross, 1974).

### 4.3. Discovery Deep

Discovery Deep is a brine-filled isolated (small) sub-basin located at the rift zone in the central Red Sea, occurring ~5 km southwest of the Atlantis II Deep (Figure 10) and constituting part of the deep-water Atlantis II - Discovery - Chain (morphological complex) system (Anschutz et al., 1999). However, even though Atlantis II Deep has been thoroughly studied due to the expected economic benefits, little research has been carried out concerning the nearby Discovery Deep, which exhibits different physical and geochemical characteristics.

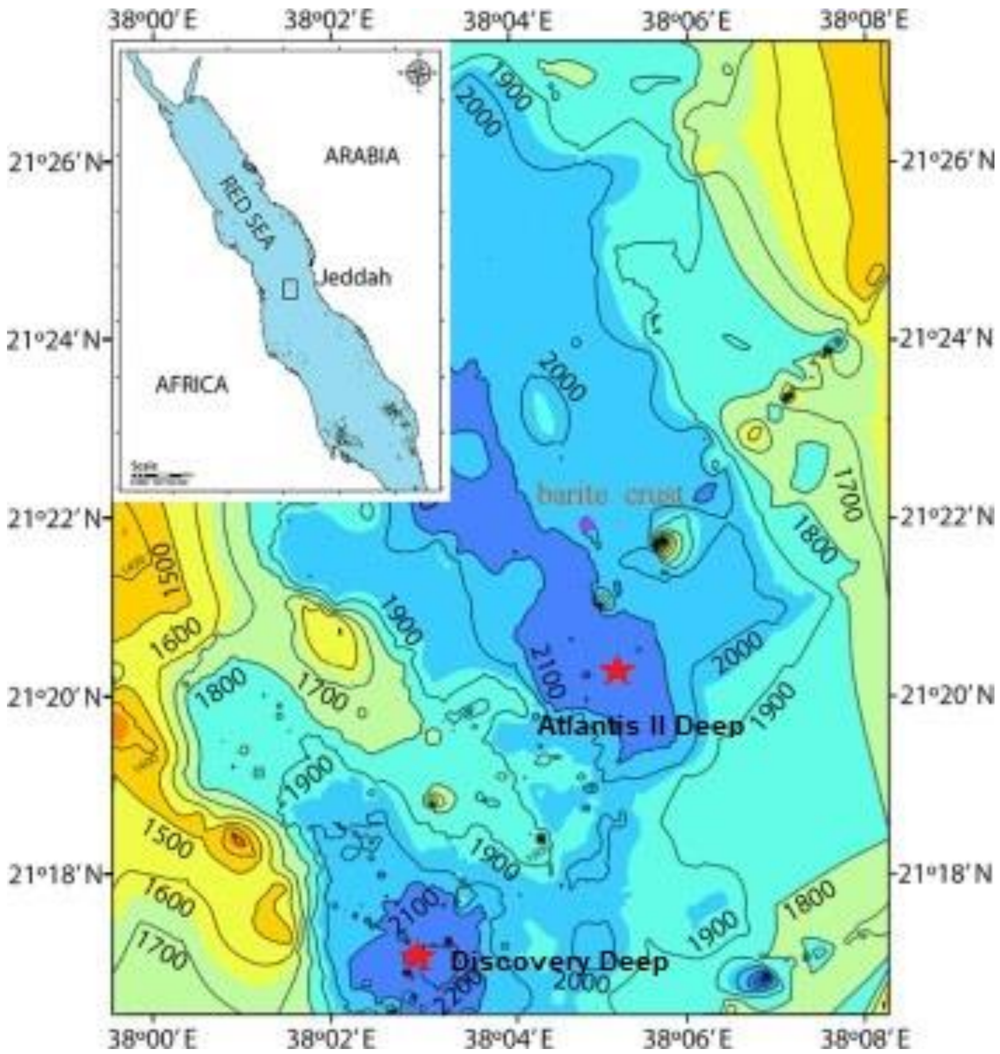


**Figure 10:** *Geographic location of two deep-sea brine pools in the Red Sea (Wang et al., 2015)*

Discovery Deep was found out in 1964 when anomalous temperatures and salinities exceeding 44 ºC and 270, respectively, were detected in a restricted depression at depths below 2000 m near 21º 17' N, 38º 02' E (Swallow & Crease, 1965).

Discovery Deep is a 2.5-km-wide and 4-km-long rounded depression, covering an area of ~12 km$^2$, with its maximum depth reaching ~2200 m. It is separated from the Atlantis II Deep by a highly irregular relief, which is featured by a sill (at a depth of ~1900 m) that acts as a connection channel between the two deeps when the latter overflows. Discovery Deep consists of a 150-m-thick transitional zone that overlies a high-temperature, oxygen-depleted, homogeneous 200-m-thick brine layer with a pH value of ~6.4 (Hunt et al., 1967; Degens & Ross, 1969; Hartmann et al., 1998; Winckler et al., 2001). Even though the environmental conditions prevailing in the brine are considered to be relatively stable, some indications of active hydrothermal activity were shown in 1995 (Hartmann et al., 1998). In particular, the temperature increased from ~45 ºC to ~50 ºC, while the brine level rose by ~17 m. At the same time, a similar increase in the temperature of Atlantis II Deep suggested a connection between the two sub-basins and the supply of new brine into Discovery Deep through the overflow of Atlantis II Deep. The association of the brine with an active hydrothermal venting system was also implied by the measured concentrations of He and Ar isotopes in analyzed water samples, indicating their mantle-derived origin (Winckler et al., 2001). However, since 1995, no significant changes in the temperature of the Discovery Deep have been recorded, leading to the conclusion that hydrothermal venting in the site is currently inactive (Swift et al., 2012).

The unique chemical composition of the Discovery Deep and the presence of metalliferous sediments below the brine are some of the most remarkable features in the site. According to Miller et al. (1966) and Bischoff (1969), the mineralogy of

Discovery Deep consists of a variety of authigenic minerals, including limonite, goethite, Fe-montmorillonite, Mn-bearing siderite, lepidocrocite and pyrite. Moreover, detrital material has been found as inmixtures with other facies, mainly composed of aragonitic pteropod shells, foraminiferal calcite tests, coccoliths, clastic quartz, feldspars and clays. Additionally, a recent study by Modenesi & Santamarina (2022) reported that the sediments of Discovery Deep result from a combination of background sedimentation and hydrothermal metalliferous sediment formation within the brine.

Finally, it should be emphasized again that even though the initial studies of the Red Sea brine pools suggested that they were sterile environments (Watson & Waterbury, 1969), due to the extreme environmental conditions, the Discovery Deep is actually teeming with life. The brine stands as an oasis where extremophile microorganisms thrive, in an otherwise barren landscape (Siam et al., 2012; Wang et al., 2015).

# 5. MATERIALS AND METHODS

## 5.1. Sediment Core Sampling and Treatment

During the "KAUST Red Sea Expedition 2010", carried out by the R/V Aegaeo of the Hellenic Center for Marine Research (HCMR), sediment sampling was performed in the Discovery Deep brine pool, using a gravity corer (from Benthos, USA) with a 4-m-long core barrel. Multiple cores were recovered from the area and one of them (3.5-m-long), obtained from ~2000 m water depth (at 21° 17.09' N, 38° 02.90' E; Figure 11), has been used for the scope of the present Thesis. After the expedition ended, a part of the collected cores (cut into ~1.2-m-long segments and tightly sealed following the guidelines of Winters (1987) was transferred to the HCMR facilities and stored at 4 °C in a humidity-controlled room.

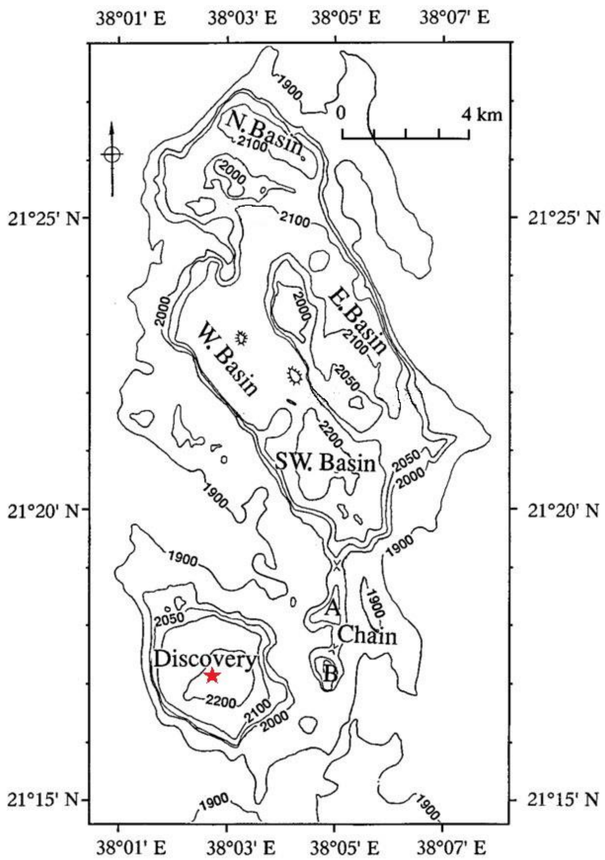


**Figure 11:** *The broader study area (Blanc & Anschutz, 1995) and location (see red star) of the investigated sediment core, recovered from the Discovery Deep brine pool.*

In 2023, the investigated sediment core was transferred to the Sedimentology Lab at the Geology Department of University of Patras for subsequent sedimentological analyses. Each core segment was split in half lengthwise for working and archival purposes (the archive half of each core was wrapped with shrink film to prevent moisture loss and contamination). The core segments were photographed and visually examined (using the unaided eye and a low-power (×10) hand lens) for characteristics such as sediment color, microstructure occurrence (e.g., laminae, patches) and signs of oxidation. Based on the visual observations, distinct sedimentary units were identified and the stratigraphic intervals for the extraction of sediment samples for the subsequent discrete analyses were determined. In brief, sedimentological analyses (including granulometric analysis, measurements of the total carbon, total inorganic carbon, total organic carbon and total nitrogen contents, sediment color determination based on the RGB color model, magnetic susceptibility measurements and inorganic geochemical analysis) as well as micropaleontological analysis and $^{14}C$ dating were integrated for the interpretation of the core from the Discovery Deep brine pool.

## 5.2. Sediment Core Dating

The age-depth model for the investigated core derived from the linear interpolation of four accelerator mass spectrometry (AMS) $^{14}C$ dates on well-preserved, clean, hand-picked mixed planktonic foraminiferal tests. The dating of monospecific planktonic foraminiferal assemblages was hindered by their relatively limited occurrence in certain core stratigraphic intervals, i.e., aggravated by the prerequisite foraminiferal specimen quantity of ~10 mg for accurate analysis. The sample preparation was carried out in the Laboratory of Historical Geology and BioGeosciences at the Geology and Geoenvironment Department of National and Kapodistrian University of Athens (NKUA), whereas AMS $^{14}C$ dating was performed at the Laboratory of Beta Analytic Inc (Florida, USA).

The results obtained from $^{14}C$ dating are, initially, reported as conventional $^{14}C$ ages (BP: AD 1950) and, therefore, need to be calibrated in the equivalent calendar years. Additionally, marine $^{14}C$ dates have to be corrected due to the local marine reservoir effect (ΔR). Hence, the conventional $^{14}C$ dates were calibrated using the CALIB v.8.2 software (Stuiver & Reimer, 1993) and the MARINE20 calibration dataset (Heaton et al., 2020) applying the nearest available regional marine reservoir correction for the central Red Sea, i.e., $\Delta R = -59 \pm 38$ (Southon et al., 2002). Based on the AMS $^{14}C$ dating, the sedimentation rates in the study site were estimated. However, the previous estimation is a rough approximation of the actual condition due to the limited number of dating points.

## 5.3. Sedimentological Analyses

**Granulometric Analysis**

Grain size analysis, along with the calculation of the sedimentological statistical parameters, is a fundamental tool in most geological studies. It offers valuable insights regarding depositional environments, sediment sources and transportation mechanisms, while it contributes to paleoenvironmental reconstructions (McManus, 1988).

Due to the high percentages of fine-grained material in the investigated core, the grain size distribution was determined with the use of a laser particle analyzer (Malvern Mastersizer Hydro 2000; by Malvern Panalytical, UK; see Figure 12).

**Figure 12:** *The Malvern Mastersizer Hydro 2000.*

The Malvern Mastersizer Hydro 2000 model is a sophisticated analyzer, which uses the laser diffraction technic to reliably determine the grain size distribution of particles suspended in a liquid medium; tap water for the present study. The laser diffraction method is especially utilized for unconsolidated sediments and is based on the principal that particles passing through a laser beam diffract light at an angle directly related to their size, with the angle increasing logarithmically as grain size decreases. In particular, the sample is dispersed into the liquid medium (tap water), ensuring a homogeneous suspension. Afterwards, a laser beam is directed through the dispersion and scattered light is detected by 52 sensors. By analyzing the angle and intensity of scattered light, this instrument calculates the particle size distribution using the Mie scattering theory, ultimately distributing particles in 100 different size classes. The Mastersizer software presents data in both graphical and numerical forms (Malvern Instruments Ltd, 2007).

**Figure 13:** *Ultrasonic water bath, Sonorex RK 100.*

The particle size analysis was performed on 26 samples (Table 1). Aliquots of sediment (a few mg) were transferred into labelled glass beakers, in which 3 ml of hydrogen peroxide ($H_2O_2$) and 40 ml of tap water were added to remove any organic particle from the samples. Following the $H_2O_2$ treatment, the samples were placed in an ultrasonic water bath (Sonorex RK 100; by BANDELIN electronic, Germany; see Figure 13) for a couple of minutes until the sediment was fully disaggregated. The Mastersizer was set up (pump speed: 2800, ultrasonic displacement: 17.50, ultrasonic timer: 00:30) and the system's cleanliness was verified through background measurements. Afterwards, the samples were dispersed in beakers filled with ~650-750 ml of tap water up to the point where obscuration level was in the appropriate range, the solution was led to suspension and, finally, data collection began.

After each measurement, the dispersion head was being lifted and the system was being cleaned (two cleaning cycles with water).

**Table 8:** *Stratigraphic intervals where grain size analysis was performed.*

| Core Samples (cm) used for Granulometric Analysis | |
|---|---|
| 14-17 | 184-186 |
| 40-42 | 198-199 |
| 76-78 | 209-212 |
| 87-89 | 218-220 |
| 100-102 | 223-224 |
| 108-110 | 228-231 |
| 111-113 | 236-239 |
| 129-131 | 250-253 |
| 134-136 | 267-270 |
| 145-147 | 283-286 |
| 166-168 | 297-300 |
| 174-175.5 | 318-321 |
| 175.5-177 | 344-347 |

The grain size percentages were calculated based on the Wentworth grading scale (Wentworth, 1922). Sediment classification as well as the statistical grain size parameters were automatically established using GRADISTAT V.8 software (Blott & Pye, 2015), based on the Folk and Ward nomenclature (Folk & Ward, 1957; Folk, 1974):

- **Mean size (Mz)** assesses the average grain size and lithology of the sediment and is also used as an indicator of the force magnitude required for sediment transport:

$$\mathrm{Mz} = \frac{\Phi 16 + \Phi 50 + \Phi 84}{3}$$

- **Standard deviation / Sorting (σi)** expresses the degree of uniformity of the grain size distribution in the sediment. High sorting values indicate heterogeneity and are usually associated with low-energy environments with high sedimentation rates, suggesting rigorous sediment transport (e.g., mass wasting events). On the other hand, low sorting values are found in homogenized sediments and indicate selective transportation in high-energy environments (e.g., coasts), provided that sediment supply is low:

$$\sigma i = \frac{\Phi 84 - \Phi 16}{4} + \frac{\Phi 95 - \Phi 5}{6.6}$$

- **Skewness (Ski)** measures the degree and "direction" of asymmetry of the grain size distribution and reflects the ability of the transport mechanism to selectively transfer fine- or coarse-grained particles. Symmetrical curves exhibit values close to 0 and, thus, have subequal amounts of fine- and coarse-grained material. When Ski >0, there is an excess of fine-grained material, whereas samples enriched with coarse material display values of Ski <0:

$$\mathrm{Ski} = \frac{\Phi 16 - \Phi 84 - 2\Phi 50}{2(\Phi 84 - \Phi 16)} + \frac{\Phi 5 + \Phi 95 - 2\Phi 50}{2(\Phi 95 - \Phi 5)}$$

- **Kurtosis ($K_G$)** describes the extent to which grain size distribution deviates from the normal probability curve. It expresses the ratio between the sorting in the central part of the probability curve and the sorting in the curve's tails. If the central portion exhibits better sorting compared to the tails, the probability curve is described as leptokurtic/excessively-peaked, whereas in the opposite case, the curve is said to be platykurtic/flat-peaked.

$$K_G = \frac{\Phi 95 - \Phi 50}{2.44(\Phi 75 - \Phi 25)}$$

## Total Carbon, Total Inorganic Carbon, Total Organic Carbon and Total Nitrogen Analysis

The relevant analysis was performed on 25 samples obtained from the same stratigraphic intervals selected for the grain size determination. Total carbon (TC), total inorganic carbon (TIC), total organic carbon (TOC) and total nitrogen (TN) measurements were carried out simultaneously, using the Shimadzu combustion-type TOC-$V_{CSH}$ Analyzer combined with the chemiluminescence detector TNM-1 TN unit (by Shimadzu Scientific Instruments, Japan; see Figure 14) (Avramidis et al., 2015).


**Figure 14:** *The Shimadzu TOC-$V_{CSH}$ Analyzer and TNM-1 TN unit.*

The Shimadzu TOC-$V_{CSH}$ analyzer employs a catalytic combustion method, which involves high-temperature (up to 720 °C) oxidation of the sample in order to convert all organic and inorganic carbon to carbon dioxide ($CO_2$) and water. The produced $CO_2$ is then measured and used to determine the TC content, while the inorganic carbon component is measured separately at the same time. Thereby, the difference between

TC and TIC values is regarded as the TOC concentration. On the other hand, the TNM-1 TN unit uses a combustion catalytic oxidation together with a chemiluminescence detection method to accurately determine TN content (Shimadzu Scientific Instruments).

For the preparation of the samples, prior to their analysis, they were placed in crucible bowls at a drying oven at 70 ºC overnight. After 18-20 h, since the samples were not completely dry yet, they were left in the oven for a couple more hours at 102 ºC. After sediments dried out, aliquots of the samples were manually powdered with the aid of a porcelain mortar and pestle (Figure 15). Approximately 0.2 g of pulverized sediment was weighted on an APX-100 analytical balance (by Denver Instrument, USA) and placed in Erlenmeyer flasks of 250 ml (Table 2).

**Figure 15:** *Powdered sample preparation for the TOC and TN determinations.*

Afterwards, 200 ml of diluted hydrochloric acid (HCl) solution was added to dissolve carbonates and form a suspension medium. For the preparation of the diluted HCl solution, 25 ml of concentrated HCl diluted in 1000 ml of distilled water were used. The samples were, then, sealed with parafilm and left for ~24 h (Figure 16).

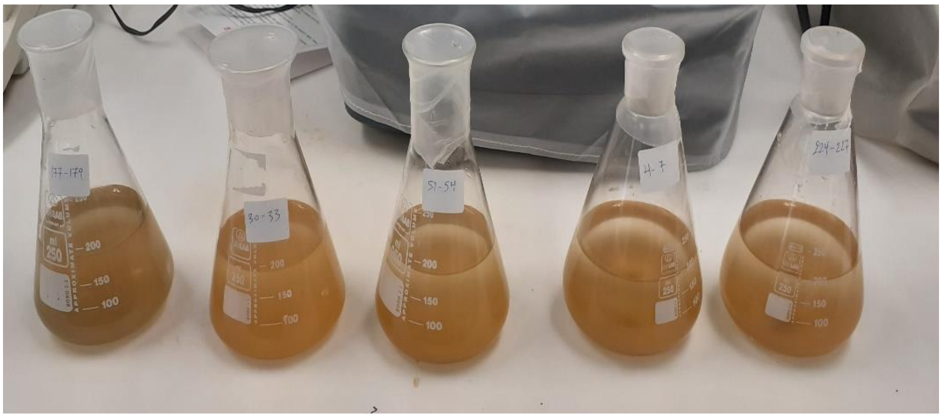

**Figure 16:** *Sediment samples suspended in HCl solution.*

Subsequently, the suspension was dispersed and homogenized, and the samples were transferred directly to the elemental analyzer, which was previously calibrated with ultrapure water, in order for the measurements to begin immediately. For each sample, the TC, TIC, TOC and TN contents were measured. The values obtained were converted from $mg \cdot L^{-1}$ to $mg \cdot g^{-1}$ and % to facilitate further calculations.

More specifically, TOC/TN ratios were calculated to identify the origin of the organic matter in the analyzed sediments. Typically, values between 4 and 10 are associated with marine sources, while values exceeding 10 generally suggest terrestrial inputs (Meyers, 1994). Furthermore, TOC and TN concentrations are ubiquitously employed in paleoenvironmental reconstructions, because they provide insights into primary productivity and bottom water oxygenation (Canfield, 1994; Gogou et al., 2007).

Finally, $CaCO_3$ concentrations were calculated using the formula of Bunzel et al. (2017): $CaCO_3(\%) = (TC - TOC) \times 8.33$.

**Table 9:** *Stratigraphic intervals where TOC and TN analysis was performed.*

| Core Samples (cm) used for TOC-TN Analysis | Weight (g) |
|---|---|
| 14-17 | 0.2006 |
| 40-42 | 0.2003 |
| 76-78 | 0.2007 |
| 87-89 | 0.2006 |
| 100-102 | 0.2002 |
| 108-110 | 0.2008 |
| 111-113 | 0.2001 |
| 129-131 | 0,200 |
| 134-136 | 0.2011 |
| 145-147 | 0.2002 |
| 166-168 | 0.2009 |
| 174-175.5 | 0.2001 |
| 175.5-177 | 0.2001 |
| 184-186 | 0.2001 |
| 198-199 | 0.2006 |
| 209-212 | 0.2002 |
| 218-220 | 0.2007 |
| 228-231 | 0.2002 |
| 236-239 | 0.2001 |
| 250-253 | 0.2008 |
| 267-270 | 0.2011 |
| 283-286 | 0.2008 |
| 297-300 | 0.2006 |
| 318-321 | 0.2011 |
| 344-347 | 0.2001 |

## Sediment Color Determination (RGB Color Model)

Sediment color is an integral component of all sedimentological studies, used to identify lithological units and minerals, facilitate stratigraphic analyses, aid in paleoenvironmental reconstructions and assist in the interpretation of geological processes and environmental conditions (Rothwell & Rack, 2006).

In the present study, sediment color determination was based on high-resolution image scanning, performed on all core segments through line-scan photography. To make more convenient the procedure, U-channels were extracted from the segments of the investigated core (see Figure 17). The Java-based ImageJ software was used to extract the RGB spectrum, with the RGB color values being displayed in a downcore depth profile.

**Magnetic Susceptibility Measurements**

Scanning was carried out for all core segments to determine the magnetic susceptibility (MS) distribution with core depth. Prior to scanning, U-channels were extracted again from the core segments to facilitate the procedure (Figures 17, 18).

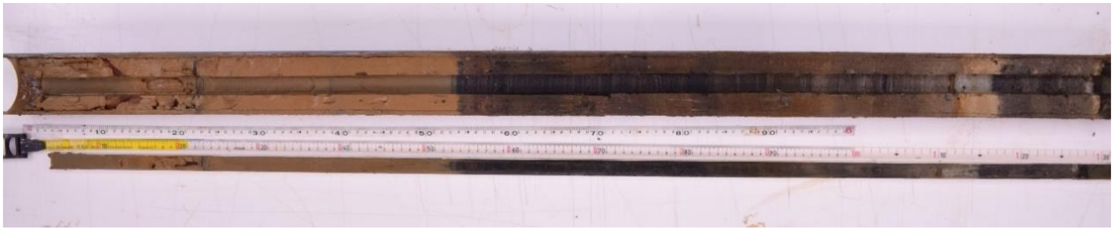

**Figure 17:** *U-channel extracted from a segment of the Discovery Deep core.*

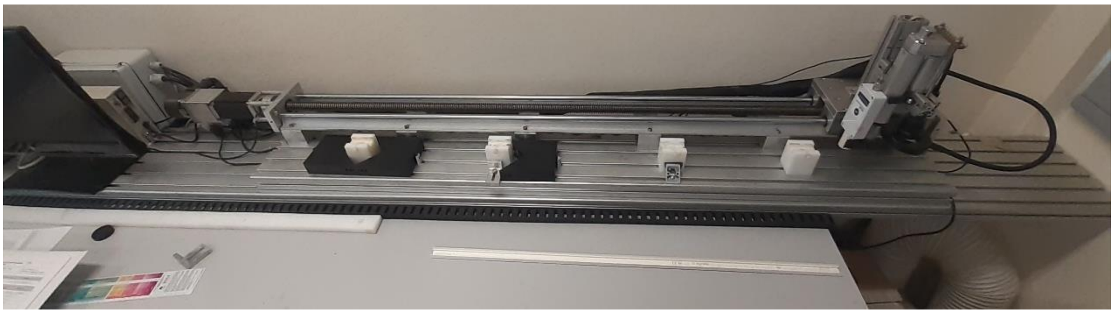

**Figure 18:** *Core scanning for the magnetic susceptibility measurements and RGB color profile as well.*

The MS determination indicates the degree to which a material can be magnetized when exposed to an external magnetic field. It is influenced by the magnetic properties of the minerals within the sediments, including their type, accumulation rate and grain size, Diamagnetic minerals (e.g., calcite, quartz) typically exhibit small or negative MS values, paramagnetic minerals (e.g., clay minerals, biotite) tend to show weak positive values, whereas ferromagnetic minerals (e.g., magnetite) demonstrate very high MS values (Dekkers, 1978). The MS determination is considered a valuable proxy, providing information about different depositional environments, sediment sources, paleoclimate and the mineralogical and geochemical composition of the sediments (Rothwell & Rack, 2006). For instance, it distinguishes marine from terrestrial sediments by the low and high MS values they exhibit, respective (Reicherter et al., 2010).

The MS determination throughout the entire sedimentary sequence was achieved using a Bartington MS2 Magnetic Susceptibility Meter (by Bartington Instruments, UK) equipped with the MS2E sensor mounted on an automated scanning system.

**Inorganic Geochemical Analysis**

To shed more light into the sedimentary processes and paleoenvironmental evolution of the Discovery Deep brine an X-ray fluorescence (XRF) analysis was performed (Figures 19). The XRF scanning was conducted with a S1 TITAN Handheld Analyzer (by Brucker, USA) and the downcore variability in the contents of 38 major (Fe, Mn), trace (Ag, As, Au, Ba, Bi, Cd, Co, Cr, Cu, Ga, Hf, Hg, Mo, Nb, Ni, Pb, Pd, Pt, Rb, Rh, Sb, Se, Sn, Sr, Ta, Te, Th, Tl, U, V, W, Zn, Zr) and Rare-earth (Ce, La, Y,) elements was determined.

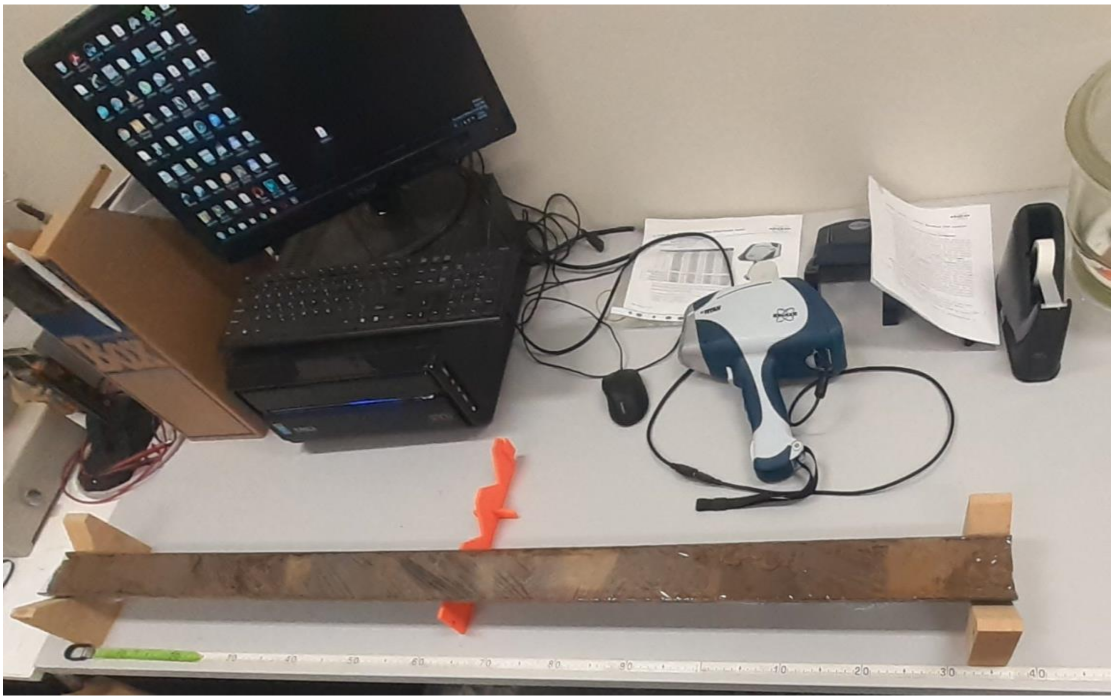

**Figure 19:** *XRF core scanning with the S1 TITAN Handheld Analyzer.*

An XRF analyzer emits a high-energy X-ray beam, which interacts with the sediment sample upon impact, causing it to fluoresce. Following this, the X-ray detector in the analyzer measures the fluorescent radiation, which is, subsequently, used to determine the elemental composition of the sediment sample, as each element exhibits distinct X-ray emissions. In addition to the elemental identification, the XRF analyzer provides quantitative results, measuring the element contents in parts per million (ppm) or in percent (%).

In general, the XRF analysis provides valuable information about lithostratigraphy, paleoceanography, environmental changes and diagenetic processes (Rothwell & Rack, 2006).

In the context of the current study, the XRF analyzer was properly calibrated (GeoExploration: Oxide3phase method) and a certified reference sample (CS–M2) was used to test instrument's performance. Prior to core scanning, the working cores segments were smoothened and carefully wrapped with cling foil in order to prevent contamination of the detector window. The handgun was properly placed in contact with the core segments and measurements were taken. The XRF core scanning was performed with a resolution of ~5 cm using a Rh tube with 10 s exposure time. Additionally, a few more measurements were taken in sediment of particular interest. Once the analysis was finished, reports for the elemental composition of each sample (in ppm) were acquired from the XRF analyzer's software.

Eventually, downcore profiles of geochemical proxies in the form of elemental ratios (e.g., Mn/Fe) were used to interpret the depositional trends, redox condition and paleoenvironmental changes in the Discovery Deep brine pool.

### 5.4. Micropaleontological Analysis

The micropaleontological analysis of the examined core was undertaken in the Laboratory of Historical Geology and BioGeosciences at the Geology and Geoenvironment Department of NKUA. More specifically, 15 sediment samples were selected for the investigation of benthic foraminiferal assemblage, abundance and diversity, thus, aliquots of ~2 g of dry sediment were used (Table 3).

**Table 3:** *Stratigraphic intervals where benthic foraminifera analysis was performed.*

| Core Samples (cm) used for Benthic Foraminifera Analysis | Weight (g) |
|---|---|
| 15-16 | 2.009 |
| 40-41 | 2.011 |
| 66-67 | 2.001 |
| 87-88 | 2.002 |
| 110-111 | 2.029 |
| 145-146 | 2.001 |
| 185-186 | 2.105 |
| 210-211 | 2.004 |
| 240-241 | 2.009 |
| 267-268 | 2.013 |
| 297-298 | 2.013 |
| 306-307 | 2.005 |
| 316-317 | 2.009 |
| 336-337 | 2.009 |
| 346-347 | 2.006 |

Each sample was transferred to a plastic beaker in which 10 ml of Perhydrol (30% w/v of $H_2O_2$) along with 40 ml of distilled water were added to disintegrate the sediment and remove organic matter. Then, the samples were transferred to a fume hood for ~4 h and, afterwards, to an ultrasound water bath for 10-15 min for further disaggregation. Finally, the samples were thoroughly washed through a 63 μm mesh sieve, using tap water to remove fine material. The residues were transferred to plastic Petri dishes and dried for 2 days in an oven at 60 ºC in order for the water to be evaporated.

After the wet sieving procedure, the samples were divided using an Otto microsplitter, to isolate a minimum of ~200 benthic foraminiferal specimens per sample (Figure 20). When the number of specimens in the subsample was not sufficient, benthic foraminifera were isolated from the entire sample.

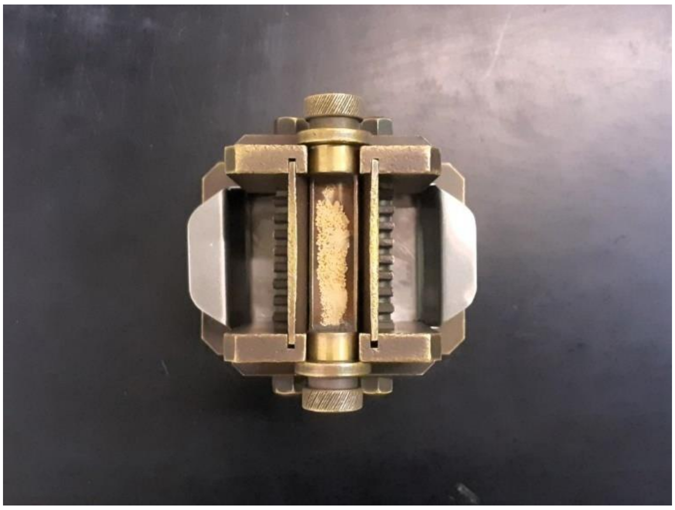

**Figure 20:** *Splitting of a sample using the Otto microsplitter.*

Afterwards, to facilitate the picking process, the subsamples were placed in a picking tray and benthic foraminifera were handpicked with the use of a fine paintbrush (No. 000) before being transferred to Chapman slides, where they were, subsequently, affixed with a special adhesive (Gomme Adragante or tragacanth gum). For their quantitative analysis, all benthic specimens were sorted, counted and identified using a Leica S8 APO stereoscope (zoom ×128) (by Leica Microsystems, Germany). The identification of benthic foraminifera was based on the generic classification of Loeblich & Tappan (1987) and the standardized nomenclature of the World Register of Marine Species (WoRMS Editorial Board, 2023). In addition to the previous subsamples, a subsample from the laminae at the stratigraphic interval of 326-327 cm was wet sieved and the microfauna was briefly examined but not quantified.

Due to the small size of the benthic foraminifera tests, several specimens were examined and photographed with the aid of a Jeol JSM-6390 Scanning Electron Microscope (SEM; by JEOL, USA; Figure 21). For their observation in SEM, foraminifera were fixed to a SEM specimen stub using double-sided adhesive tape. Eventually, the prepared stud was gold coated using the Agar Auto Sputter Coater (by Agar Scientific, UK) and transferred to SEM for imaging.


**Figure 21:** *The Jeol JSM-6390 Scanning Electron Microscope.*

## Statistical Data Analysis

For the evaluation of the benthic foraminifera community, the following indices were estimated:

- **Absolute abundance:** the total number of benthic foraminiferal specimens per gram of dry sediment (BFN – Benthic Foraminifera No., $n \cdot g^{-1}$).

- **Relative abundance:** expressed as percentage (%) of the total benthic foraminiferal population, for the three prevailing genera.

In addition to the abovementioned indices, benthic foraminiferal diversity indices were calculated, using the Past.exe. 4.03. software package (Hammer et al., 2001), in order to assess the overall community structure in the Discovery Deep brine pool and the prevailing environmental conditions:

- **Species richness (S):** number of different taxa.
- **Dominance index (D):** used to assess the dominance of a certain species (Ludwig & Reynolds, 1988).
- **Species evenness (J):** determines whether all species are equally abundant (Ludwig & Reynolds, 1988).
- **Shannon-Wiener index (H'):** one of the most widely-employed tools for assessing heterogeneity, based on species richness and the relative abundance of each species (Shannon, 1948; Murray, 1991).
- **Fisher's alpha index (a-index):** a reliable assessment of biodiversity, based on the relation between the number of species and the number of individuals (Fisher et al., 1943).

The fragmented and poorly preserved agglutinated tests were excluded from the majority of the data analysis. They were only used as separate taxa in the calculation of species richness.

# 6. RESULTS

## 6.1. Core Physical Description

Upon visual examination, three distinct lithostratigraphic units were identified in the sediment core from the Discovery Deep brine (Figure 22): (i) an upper unit (Unit A: 0-87 cm) characterized by homogeneous brownish pelagic mud, with a dark lamina at ~65 cm (see Unit A in Figure 22); (ii) an intermediate unit (Unit B: 87-297 cm) including a continuous alternation of color-banded layers and laminae (i.e., ≤1 cm thick); and, finally, (iii) a bottom unit (Unit C: 297-350 cm) exhibiting light brownish homogeneous pelagic mud, with a dark lamina at ~328 cm (see Unit C in Figure 22).

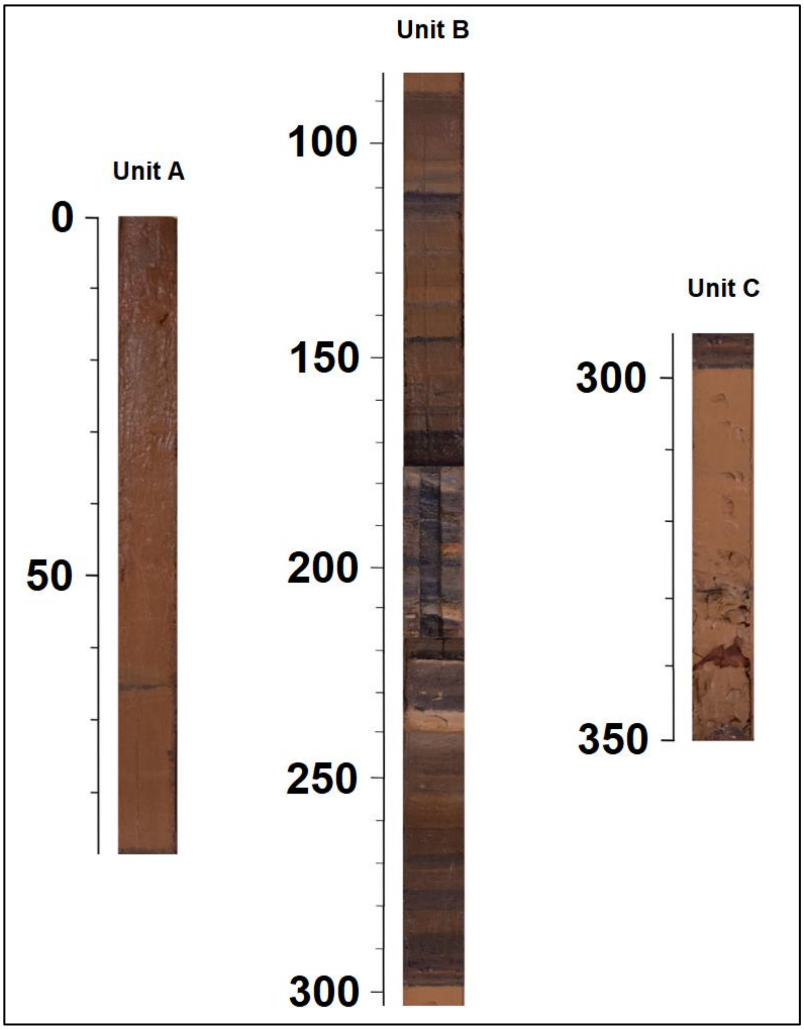


**Figure 22:** *The distinct sedimentary units (A, B and C) in the Discovery Deep core, based on visual observation, are presented. The vertical scales are in centimeters.*

In general, the Discovery Deep deposit comprises medium sand to fine silt, with the relevant statistics of the grain size distribution showing variability, without a persistent trend dominating the core (except the poor to very poor sediment sorting), i.e., Mz ranges from 1.5 to 7.63, Ski fluctuates from very fine skewed to symmetrical to coarse skewed and $K_G$ extends from extremely leptokurtic to leptokurtic to mesokurtic to platykurtic to very platykurtic (see Figure 23 and Table 4).

Concerning the TOC profile, the Discovery Deep deposit may, generally, be characterized as organic-poor material (the majority of analyzed samples showed values less than 0.5). Similarly, $CaCO_3$ contents appear low throughout the core (less than 20%), most probably reflecting the abundance of foraminiferal tests in the sediment column and, therefore, representing the biogenic component. Also, the commonly used TOC/TN ratio consistently exceeds the marine threshold condition (see Figure 24 and Table 5), suggesting a terrestrial origin for the collected sediment. This sounds peculiar for a deposit recovered from a depth of ~2000 m, considering that past evidence of bottom or turbidity currents originating from the Red Sea margin have not been reported yet, while only the study of Ehrmann, et al., (2024) indicates aeolian terrigenous silt inputs, during the last 200 kyr, at a relatively high water depth (~825 m) in the central Red Sea, with their sources primarily being in the eastern Sahara and secondary in the eastern Arabian Peninsula and/or Mesopotamia, and in the northern Egypt.

Finally, the MS values are, in general, relatively positively weak, however, displaying a few minor negative values within the 177-183 cm stratigraphic interval and several significantly higher positive peaks (values greater than $100 \times 10^{-6}$ CGS) within Unit B (see Figure 23).

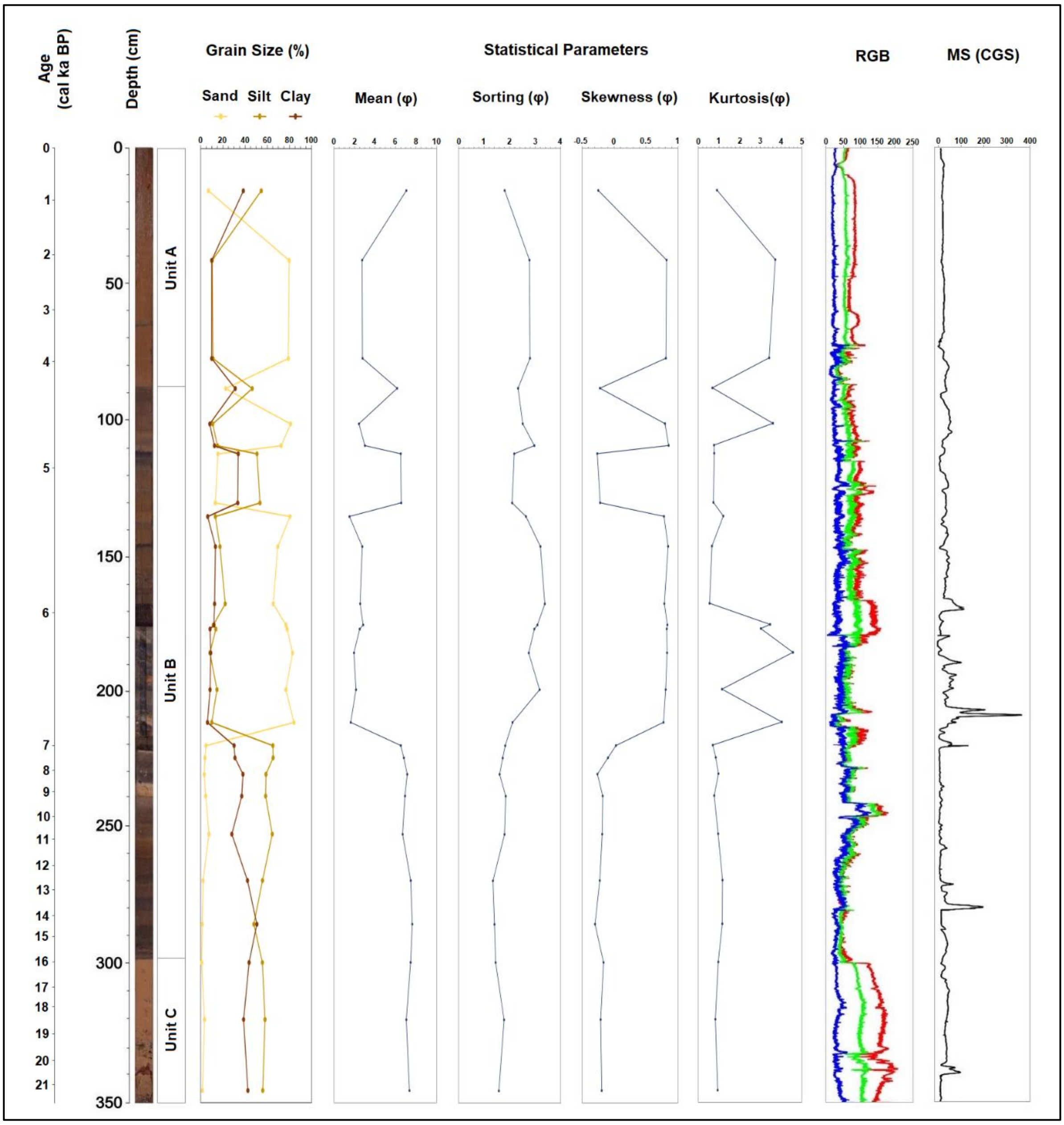


**Figure 23:** *The lithology of the Discovery Deep core along with the calibrated $^{14}C$ dating (based on the age-depth model) is presented. The grain size distribution (i.e., clay, silt and sand) together with the profiles of the relevant statistical parameters are illustrated. The RGB color model profile and the MS measurements also appear.*

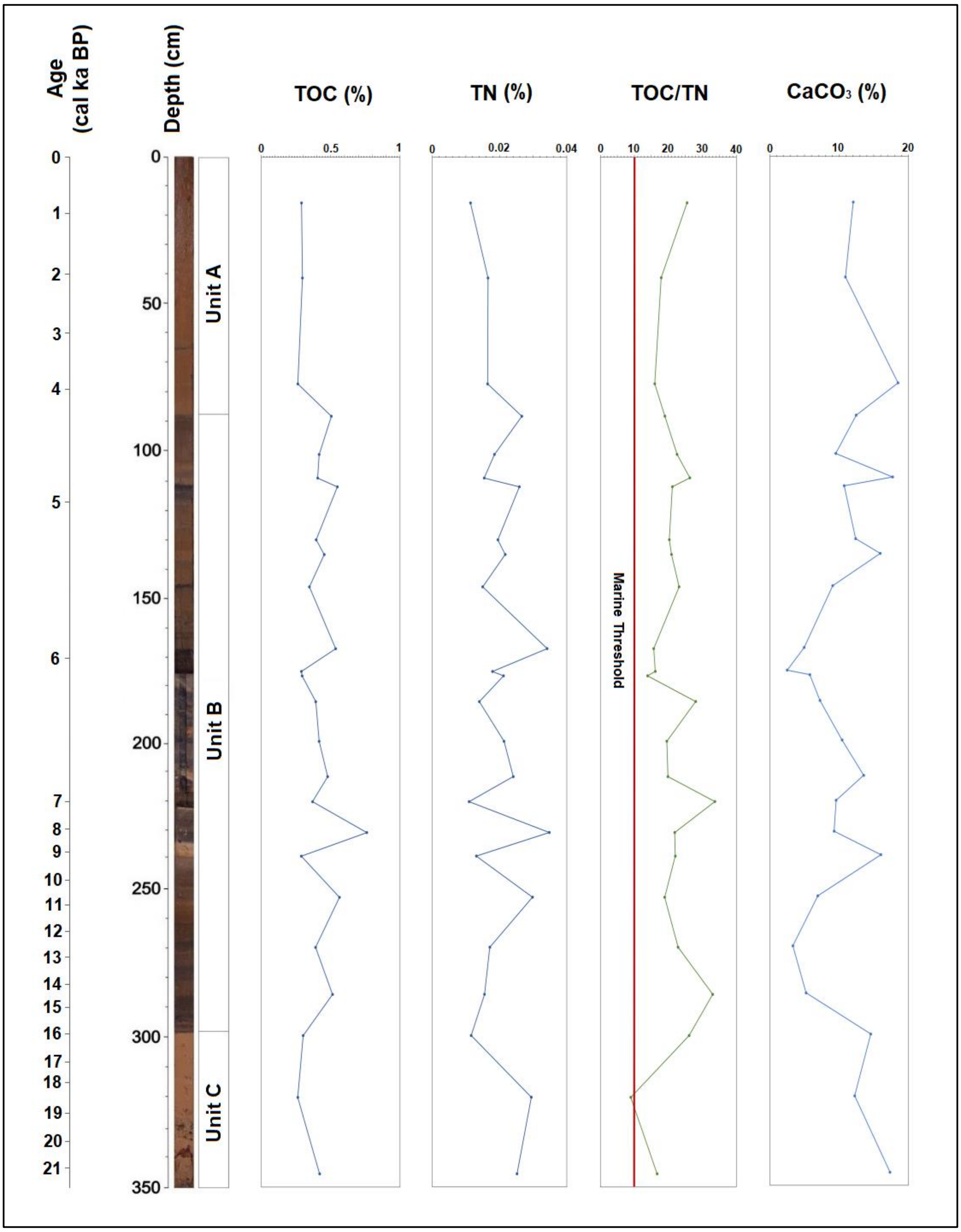


**Figure 24:** *The TOC, TN, TOC/TN and $CaCO_3$ profiles along the Discovery Deep core are displayed.*

**Table 4:** *Grain size analysis results of the Discovery Deep core.*

| DEPTH (cm) | Wentworth Size Class | | | FOLK AND WARD METHOD | | | | | | | |
|---|---|---|---|---|---|---|---|---|---|---|---|
| | GRAIN SIZE (%) | | | MEAN (Mz) | | SORTING ($\sigma_i$) | | SKEWNESS ($Sk_i$) | | KURTOSIS ($K_G$) | |
| | Sand | Silt | Clay | ϕ | Description | ϕ | Description | ϕ | Description | ϕ | Description |
| **14-17** | 6.96 | 54.57 | 38.47 | 7.05 | Fine Silt | 1.81 | Poorly Sorted | -0.25 | Coarse Skewed | 0.90 | Platykurtic |
| **40-42** | 79.78 | 10.29 | 9.93 | 2.75 | Fine Sand | 2.78 | Very Poorly Sorted | 0.82 | Very Fine Skewed | 3.72 | Extremely Leptokurtic |
| **76-78** | 78.94 | 11.15 | 9.91 | 2.78 | Fine Sand | 2.80 | Very Poorly Sorted | 0.81 | Very Fine Skewed | 3.43 | Extremely Leptokurtic |
| **87-89** | 22.54 | 46.40 | 31.06 | 6.15 | Medium Silt | 2.33 | Very Poorly Sorted | -0.22 | Coarse Skewed | 0.68 | Platykurtic |
| **100-102** | 81.11 | 10.75 | 8.14 | 2.43 | Fine Sand | 2.51 | Very Poorly Sorted | 0.80 | Very Fine Skewed | 3.61 | Extremely Leptokurtic |
| **108-110** | 72.48 | 15.13 | 12.39 | 3.01 | Very Fine Sand | 2.97 | Very Poorly Sorted | 0.85 | Very Fine Skewed | 0.75 | Platykurtic |
| **111-113** | 15.50 | 50.74 | 33.76 | 6.50 | Medium Silt | 2.18 | Very Poorly Sorted | -0.26 | Coarse Skewed | 0.76 | Platykurtic |
| **129-131** | 13.14 | 53.47 | 33.39 | 6.55 | Medium Silt | 2.10 | Very Poorly Sorted | -0.22 | Coarse Skewed | 0.73 | Platykurtic |
| **134-136** | 80.51 | 13.16 | 6.33 | 1.50 | Medium Sand | 2.64 | Very Poorly Sorted | 0.78 | Very Fine Skewed | 1.20 | Leptokurtic |
| **145-147** | 69.43 | 17.34 | 13.22 | 2.76 | Fine Sand | 3.21 | Very Poorly Sorted | 0.85 | Very Fine Skewed | 0.65 | Very Platykurtic |
| **166-168** | 65.37 | 22.11 | 12.52 | 2.55 | Fine Sand | 3.38 | Very Poorly Sorted | 0.79 | Very Fine Skewed | 0.54 | Very Platykurtic |
| **174-175,5** | 76.76 | 11.31 | 11.94 | 2.84 | Fine Sand | 3.09 | Very Poorly Sorted | 0.83 | Very Fine Skewed | 3.47 | Extremely Leptokurtic |
| **175,5-177** | 77.97 | 13.65 | 8.38 | 2.51 | Fine Sand | 2.97 | Very Poorly Sorted | 0.82 | Very Fine Skewed | 3.02 | Extremely Leptokurtic |
| **184-186** | 82.76 | 8.30 | 8.94 | 1.94 | Medium Sand | 2.75 | Very Poorly Sorted | 0.83 | Very Fine Skewed | 4.58 | Extremely Leptokurtic |
| **198-199** | 76.79 | 14.62 | 8.46 | 2.14 | Fine Sand | 3.17 | Very Poorly Sorted | 0.81 | Very Fine Skewed | 1.14 | Leptokurtic |
| **209-212** | 84.01 | 9.92 | 6.08 | 1.63 | Medium Sand | 2.11 | Very Poorly Sorted | 0.77 | Very Fine Skewed | 4.04 | Extremely Leptokurtic |
| **218-220** | 4.80 | 65.11 | 30.10 | 6.51 | Medium Silt | 1.83 | Poorly Sorted | 0.03 | Symmetrical | 0.70 | Platykurtic |
| **223-224** | 3.84 | 65.30 | 30.86 | 6.81 | Medium Silt | 1.73 | Poorly Sorted | -0.10 | Symmetrical | 0.84 | Platykurtic |
| **228-231** | 3.07 | 58.86 | 38.07 | 7.14 | Fine Silt | 1.61 | Poorly Sorted | -0.26 | Coarse Skewed | 0.97 | Mesokurtic |
| **236-239** | 4.49 | 58.53 | 36.98 | 6.92 | Medium Silt | 1.85 | Poorly Sorted | -0.18 | Coarse Skewed | 0.77 | Platykurtic |
| **250-253** | 7.43 | 64.49 | 28.08 | 6.69 | Medium Silt | 1.80 | Poorly Sorted | -0.19 | Coarse Skewed | 0.96 | Mesokurtic |
| **267-270** | 2.07 | 55.74 | 42.19 | 7.48 | Fine Silt | 1.35 | Poorly Sorted | -0.22 | Coarse Skewed | 1.17 | Leptokurtic |
| **283-286** | 1.42 | 47.96 | 50.62 | 7.63 | Fine Silt | 1.41 | Poorly Sorted | -0.30 | Coarse Skewed | 1.16 | Leptokurtic |
| **297-300** | 0.84 | 55.54 | 43.62 | 7.47 | Fine Silt | 1.45 | Poorly Sorted | -0.16 | Coarse Skewed | 0.96 | Mesokurtic |
| **318-321** | 3.32 | 57.99 | 38.70 | 7.05 | Fine Silt | 1.78 | Poorly Sorted | -0.21 | Coarse Skewed | 0.82 | Platykurtic |
| **344-347** | 1.55 | 55.96 | 42.49 | 7.35 | Fine Silt | 1.58 | Poorly Sorted | -0.19 | Coarse Skewed | 0.93 | Mesokurtic |

**Table 5:** *Carbon, carbonate and nitrogen bulk analysis results of the Discovery Deep core.*

| DEPTH (cm) | TC % | IC % | TOC % | TN % | TOC/TN | CaCO3 % |
|---|---|---|---|---|---|---|
| 14-17 | 1.73 | 1.45 | 0.29 | 0.01 | 25.51 | 12.04 |
| 40-42 | 1.61 | 1.31 | 0.30 | 0.02 | 17.89 | 10.91 |
| 76-78 | 2.48 | 2.22 | 0.26 | 0.02 | 15.99 | 18.50 |
| 87-89 | 2.00 | 1.50 | 0.50 | 0.03 | 18.97 | 12.46 |
| 100-102 | 1.56 | 1.14 | 0.42 | 0.02 | 22.56 | 9.52 |
| 108-110 | 2.53 | 2.13 | 0.41 | 0.02 | 26.32 | 17.72 |
| 111-113 | 1.84 | 1.29 | 0.55 | 0.03 | 21.17 | 10.73 |
| 129-131 | 1.88 | 1.49 | 0.40 | 0.02 | 20.29 | 12.38 |
| 134-136 | 2.37 | 1.91 | 0.45 | 0.02 | 20.93 | 15.94 |
| 145-147 | 1.44 | 1.09 | 0.35 | 0.01 | 23.16 | 9.08 |
| 166-168 | 1.13 | 0.59 | 0.54 | 0.03 | 15.69 | 4.96 |
| 174-175,5 | 0.59 | 0.30 | 0.29 | 0.02 | 16.17 | 2.50 |
| 175,5-177 | 0.99 | 0.69 | 0.29 | 0.02 | 13.89 | 5.77 |
| 184-186 | 1.26 | 0.87 | 0.39 | 0.01 | 28.05 | 7.23 |
| 198-199 | 1.67 | 1.25 | 0.42 | 0.02 | 19.56 | 10.43 |
| 209-212 | 2.10 | 1.63 | 0.48 | 0.02 | 19.87 | 13.55 |
| 218-220 | 1.52 | 1.15 | 0.37 | 0.01 | 33.70 | 9.57 |
| 228-231 | 1.87 | 1.11 | 0.76 | 0.03 | 21.87 | 9.28 |
| 236-239 | 2.21 | 1.92 | 0.29 | 0.01 | 22.04 | 16.03 |
| 250-253 | 1.39 | 0.83 | 0.56 | 0.03 | 18.92 | 6.92 |
| 267-270 | 0.79 | 0.40 | 0.39 | 0.02 | 22.87 | 3.32 |
| 283-286 | 1.14 | 0.63 | 0.51 | 0.02 | 33.04 | 5.23 |
| 297-300 | 2.05 | 1.75 | 0.30 | 0.01 | 26.10 | 14.57 |
| 318-321 | 1.73 | 1.47 | 0.26 | 0.03 | 8.94 | 12.25 |
| 344-347 | 2.50 | 2.08 | 0.42 | 0.03 | 16.69 | 17.35 |

**Lithological Unit A (0-87 cm)**

It consists of poorly to very poorly sorted (σi: 1.81-2.80) light reddish-brown fine silt to fine sand (Mz: 2.75-7.05), with sand prevailing within a major part of the stratigraphic interval reaching up to 80% (see Figure 23). The Ski (-0.25 to 0.81) and $K_G$ (0.9-3.72) distributions show asymmetrical and platykurtic to extremely leptokurtic trends, respectively. The MS values appear relatively weak (average of $20 \times 10^{-6}$ CGS), while the magnetic signal demonstrates an almost uniform pattern. Finally, the TOC content is nearly stable (0.26-0.3%), the TOC/TN ratio exceeds ~16 and the $CaCO_3$ contents present the maximum measured value within the core, i.e., 18.5%.

**Lithological Unit B (87-297 cm)**

In contrast to Unit A, it exhibits distinct changes in the grain size, evident pulses in the MS and RGB color signals, and the highest TOC/TN values in the core (with most of them exceeding ~20). This emphasizes the fact that the deposition of this stratigraphic interval is mainly the result of an extreme geological process, i.e., hydrothermal sedimentation.

Based on the profiles of the grain size statistics, RGB color model, MS, TOC content and TOC/TN ratio, Unit B can be divided into three subunits (i.e., B1, B2 and B3), each one probably reflecting a different intensity of hydrothermal impact. The subunit B1 (87-134 cm) consists of very poorly sorted (σi: 2.1-2.97) darkish-brown medium silt to fine sand (Mz: 2.43-6.55). The sediment is coarse skewed to very fine skewed (-0.26 to 0.85), with the kurtosis pattern ranging from platykurtic to extremely leptokurtic distribution ($K_G$: 0.68-3.61). The MS values are positively weak, varying between 6 and $56 \times 10^{-6}$ CGS. Finally, the TOC content shows values between 0.4% and 0.55%, while the TOC/TN ratio fluctuates from 19 to 26.3. The intermediate subunit B2 (134-212 cm) includes alternating dark brown, black, grayish, reddish layers and laminae composed of very poorly sorted (σi: 2.11-3.38) medium to fine sand (Mz: 1.5-2.84). The grain size distribution of this stratigraphic interval appears very fine skewed (Ski: 0.77 to 0.85) and very platykurtic to extremely leptokurtic ($K_G$: 0.54-4.58). The most prominent feature of subunit B2 is the occurrence of a few high peaks in the MS signal, with the values exceeding 100 × $10^{-6}$ CGS and reaching a maximum of 363 × $10^{-6}$ CGS at 206 cm. Eventually, the TOC content fluctuates between 0.29% and 0.54%, while the TOC/TN ratio ranges from 13.9 to 28.1. The subunit B3 (212-297 cm) comprises blackish-gray, brown, reddish and almost white layers, as well as blackish-brown laminae towards the bottom of the deposit. The occurring sediment appears poorly sorted (σi: 1.35-1.85) and is characterized as fine to medium silt (Mz: 6.51-7.63). The grain size distribution shows symmetrical to coarse skewed (Ski: -0.3 to 0.03) and platykurtic to leptokurtic ($K_G$: 0.7-1.17) trends. The MS values are relatively low with an average of 16.5 × $10^{-6}$ CGS; however, there is a couple of peaks exceeding 100 × $10^{-6}$ CGS. Finally, the TOC content varies between 0.29% and 0.76%, while the TOC/TN ratio displays values between 18.9 and 33.7 (i.e., the maximum value at 218-220 cm).

**Lithological Unit C (297-350 cm)**

It is composed of poorly sorted (σi: 1.45-1.78) light brownish fine silt (Mz: 7.05-7.47). The grain size distribution is characterized as coarse skewed, showing a narrow range of values (Ski: -0.16 to -0.21), while a platykurtic and mesokurtic trend prevails ($K_G$: 0.82-0.96). The MS signal in Unit C appears relatively weak with the relevant values having an average of 20 × $10^{-6}$ CGS; however, a peak of 95 × $10^{-6}$ CGS at 335 cm is evident. Finally, the TOC content ranges between 0.26% and 0.42%, while the TOC/TN ratio exhibits a remarkably variation extending from 8.9 (i.e., the minimum value in the entire core) to 26.1.

## 6.2. Age Assessment and Sedimentation Rates

The age-depth model for the Discovery Deep core was established using the four calibrated $^{14}C$ ages, with a $2\sigma$ uncertainty of ± 0.2 ka (Table 6, Figure 25). Based on the observed trend, the sedimentary sequence spans from the "Late" Pleistocene (21.43 ka BP) to the present time and is associated with the cool Marine Isotope Stage 2 (MIS-2: 29-11.7 ka BP) and the current warm Marine Isotope Stage 1 (MIS-1: 11.7 ka BP to present). Assuming linear relationships between the data points (see Figure 25), the sedimentation rates at specific stratigraphic intervals have been estimated and are presented in Table 7. It is apparent an excessive sediment accumulation in the largest part of the hydrothermal impacted Unit B, most of which has been deposited in the interglacial MIS-1. In particular, an astonishing, for deep-water environment, sedimentation rate (107 cm/ka) is observed between 6.56-6.26 cal ka BP.

**Table 6:** *Conventional and calibrated $^{14}C$ ages for the Discovery Deep core at four stratigraphic levels.*

| Lab Number | Depth (cm) | 14C Age (yr BP) | Calibrated Age (2σ) (cal ka BP) | Mean Calibrated Age (cal ka BP) |
|---|---|---|---|---|
| Beta-675644 | 87 – 88 | 4380 ± 30 | 4.21 – 4.62 | 4.41 ± 0.20 |
| Beta-675643 | 185 – 186 | 5970 ± 30 | 6.08 – 6.43 | 6.26 ± 0.18 |
| Beta-675642 | 217 – 218 | 6260 ± 30 | 6.38 – 6.75 | 6.56 ± 0.18 |
| Beta-675641 | 310 – 311 | 14840 ± 50 | 16.94 – 17.46 | 17.20 ± 0.26 |

**Table 7:** *Approximate sedimentation rates for the Discovery Deep core, based on the age-depth model.*

| Depth (cm) | Sedimentation Rate (cm/ka) |
|---|---|
| 0-87 | 19.73 |
| 87-185 | 52.97 |
| 185-217 | 106.67 |
| 217-310 | 8.74 |
| 310-347 | 8.81 |

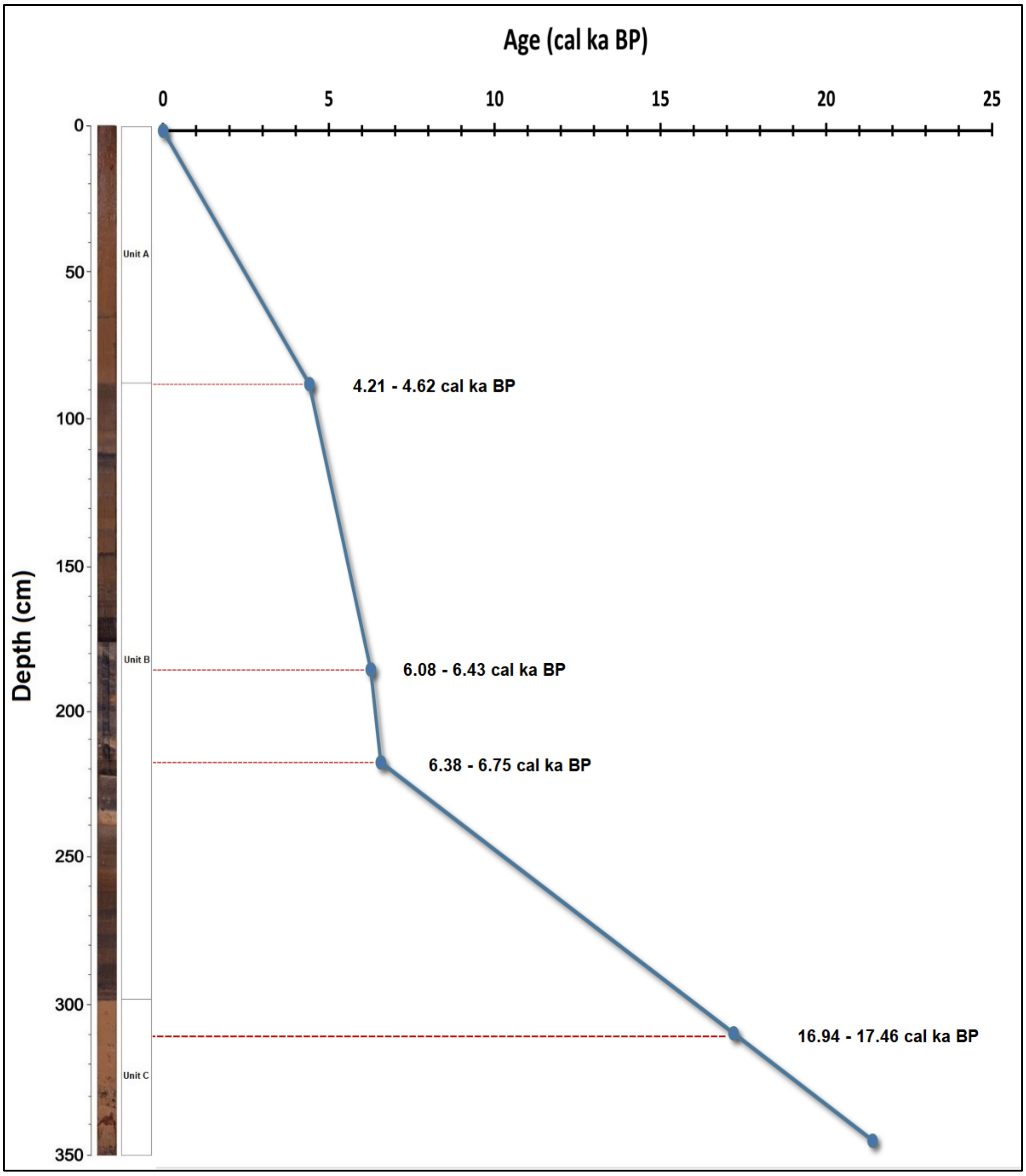


**Figure 25:** *The age-depth model of the Discovery Deep deposit with the calibrated $^{14}C$ ages is illustrated.*

### 6.3. Inorganic Geochemical Analysis

The most abundant geochemical element in the Discovery Deep core is Fe (see Figure 26 and Table 8), with an average content of 21,714 ppm. The Fe profile exhibits several distinct peaks in the subunits B2 and B3. However, the most prominent element throughout the core is Mn, with most of its contents ranging from 1200 ppm (higher than the typical marine baseline) up to extraordinary values of 14,300 to 62,300 ppm (occurring in Unit B, in the stratigraphic interval 176-256 cm of the subunits B2 and B3). The excessive peaks of Mn are observed within certain darkish layers. Concerning the Mn/Fe ratio, which is a reliable proxy for tracing the bottom water oxygenation, its downcore distribution (Figure 26) shows continuously low ratios in Units A and C, suggesting poor water oxygenation (a more rapid reduction of Mn than Fe under anoxic conditions leads to a preferential Mn release, resulting in low Mn/Fe values; Loizeau et al., 2001; Naeher et al., 2013). In contrast, in Unit B, the Mn/Fe ratio displays considerable fluctuations, marked by several sharp positive peaks, indicating time intervals (at 4.5, 5.2, 6.1-6.2, 7.2-7.5 and 9.1-11 cal ka BP) of seafloor oxygenation due to oxygen diffusion via the interface of the typical seawater with the brine.

The contents of economically important metals in the brine-filled Discovery Deep are notably limited compared to other analogous sites in Red Sea. Most elemental contents display irregular variations with depth, while they do not show significant correlations between them. In particular, Ag is entirely absent, while the contents of Cu and Co range from 0 to 72 ppm and 0 to 347 ppm, respectively, with minor enrichments of Cu observed in Units A and B. In terms of elemental correlations, based on the well-known Pearson correlation coefficient (r), only the Co distribution shows a good correlation with the Mn contents ($r = 0.8$), which may be attributed to the absorption of Co into the Mn oxyhydroxides occurring in the Discovery Deep deposits. However, Ni, which is also affiliated with Mn oxyhydroxides, does not show any statistical correlation with Mn, while its occurrence in the Discovery Deep deposit is surprisingly limited. Finally, even though the Zn content is, in general, quite low within the core, a pronounced increase in the uppermost part of Unit B, reaching up to 1546 ppm at 116 cm is observed (Figure 26).

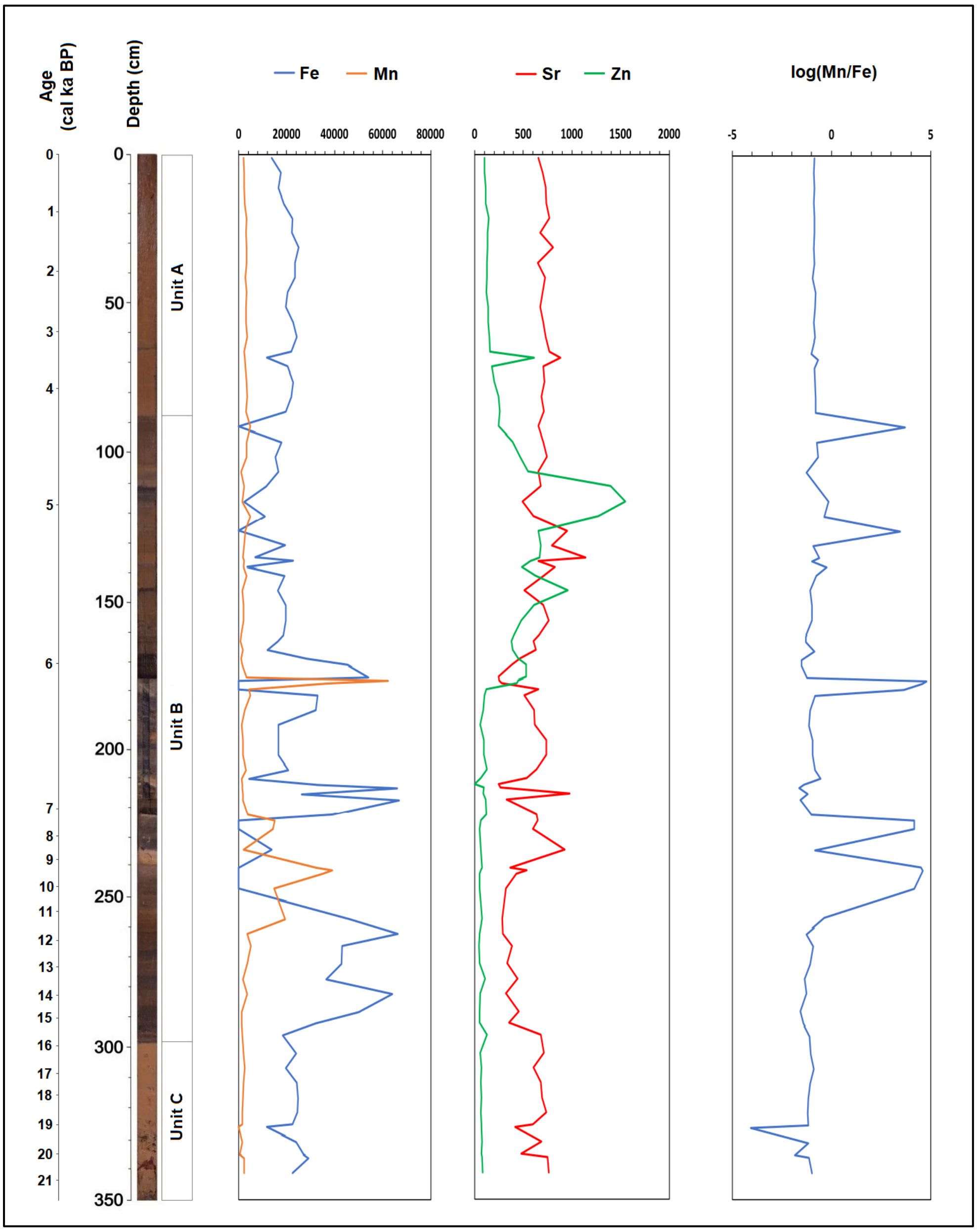


**Figure 26:** *Profiles of the more enhanced element contents and distribution of the widely-used geochemical proxy (log(Mn/Fe) ratio) in the Discovery Deep core.*

Further, base metals such as Cd, Pb and Tl occur in limited values, showing a fuzzy trend. In addition, the chalcophile elements As, Hg, Sb and Sn, along with Cr, Mo, Rb and U, are also found only in minor contents. In contrast, the Sr contents appear increased, compared to the rest of the trace metals, ranging from 247 and 1136 ppm (Table 8). In Units A and C, its content shows a rough consistency, whereas in Unit B, the Sr values vary continuously, exhibiting some sharp peaks (Figure 26). Finally, the Ba contents show an average of only 111 ppm (this is in contrast with the abundant barite ($BaSO_4$) crust found in the neighboring Atlantis II Deep; Wang et al., 2015), showing just two small peaks in Unit B, at 135 and 233 cm, while the V content greatly fluctuates within the core, however, being almost absent in subunit B3 and Unit C.

**Table 8:** *Inorganic geochemistry (elemental contents in ppm) of the core from Discovery Deep (n.d.: no data). The zero values correspond to the detection limit of the performed XRF analysis.*

| Depth (cm) | Ag | As | Au | Ba | Bi | Cd | Ce | Co | Cr | Cu |
|---|---|---|---|---|---|---|---|---|---|---|
| 1 | 0 | 13 | 32 | 149 | 0 | 0 | 308 | 27 | 0 | 57 |
| 6 | 0 | 11 | 0 | 142 | 12 | 10 | 101 | 19 | 0 | 9 |
| 11 | 0 | 14 | 0 | 94 | 45 | 3 | 188 | 49 | 0 | 43 |
| 16 | 0 | 5 | n.d. | 188 | 0 | 8 | 304 | 50 | 17 | 0 |
| 21 | n.d. | 11 | 12 | 172 | 4 | 5 | 196 | 111 | 17 | 72 |
| 26 | 0 | 6 | 24 | 61 | 0 | 6 | 95 | 81 | 0 | 25 |
| 31 | n.d. | 26 | 32 | 162 | 0 | 2 | 252 | 57 | 31 | 26 |
| 36 | n.d. | 25 | n.d. | 132 | 0 | 4 | 178 | 66 | 61 | 44 |
| 41 | n.d. | 17 | 16 | 149 | 0 | 2 | 304 | 41 | 0 | 33 |
| 46 | n.d. | 19 | 22 | 120 | 2 | 6 | 119 | 106 | 0 | 32 |
| 51 | n.d. | 13 | 12 | 141 | 0 | 2 | 385 | 24 | 0 | 0 |
| 56 | n.d. | 13 | 17 | 158 | 0 | 1 | 340 | 109 | 0 | 26 |
| 61 | n.d. | 12 | 10 | 130 | 20 | 9 | 112 | 76 | 48 | 32 |
| 66 | 0 | 11 | n.d. | 77 | 0 | 0 | 308 | 28 | 71 | 30 |
| 68 | n.d. | 14 | 20 | 119 | 0 | 1 | 245 | 122 | 0 | 23 |
| 71 | 0 | 10 | n.d. | 167 | 25 | 0 | 256 | 44 | 0 | 0 |
| 76 | n.d. | 12 | 22 | 130 | 0 | 3 | 269 | 43 | 0 | 29 |
| 81 | n.d. | 11 | 12 | 104 | 1 | 6 | 180 | 87 | 0 | 29 |
| 86 | n.d. | 7 | 0 | 132 | 0 | 6 | 457 | 82 | 0 | 25 |
| 91 | 0 | 27 | 0 | 84 | 0 | 6 | 212 | 95 | 0 | 12 |
| 96 | 0 | 21 | n.d. | 38 | 0 | 6 | 153 | 100 | 0 | 21 |
| 101 | n.d. | 21 | 0 | 114 | 0 | 0 | 126 | 48 | 11 | 22 |
| 106 | 0 | 5 | 31 | 93 | 0 | 0 | 271 | 34 | 76 | 0 |
| 111 | n.d. | 17 | n.d. | 89 | 6 | 3 | 182 | 78 | 0 | 68 |
| 116 | n.d. | 17 | n.d. | 132 | 0 | 7 | 128 | 46 | 0 | 50 |
| 121 | n.d. | 18 | 41 | 163 | 0 | 8 | 152 | 91 | 0 | 24 |
| 126 | 0 | 18 | n.d. | 140 | 0 | 0 | 136 | 98 | 0 | 8 |
| 131 | 0 | 17 | 11 | 74 | 0 | 9 | 83 | 72 | 0 | 9 |
| 135 | 0 | 24 | 0 | 288 | 2 | 2 | 183 | 35 | 19 | 0 |
| 136 | n.d. | 12 | 11 | 178 | 0 | 0 | 111 | 123 | 0 | 18 |
| 138 | 0 | 10 | 0 | 212 | 12 | 0 | 115 | 0 | 0 | 2 |
| 141 | 0 | 8 | 23 | 213 | 0 | 2 | 167 | 49 | 0 | 17 |
| 146 | n.d. | 39 | 10 | 139 | 0 | 13 | 0 | 76 | 0 | 45 |
| 151 | 0 | 8 | 37 | 86 | 0 | 9 | 279 | 100 | 0 | 31 |
| 156 | n.d. | 8 | 22 | 141 | 0 | 16 | 94 | 85 | 0 | 15 |
| 161 | 0 | 9 | n.d. | 132 | 0 | 6 | 419 | 72 | 48 | 15 |
| 163 | 0 | 23 | 21 | 108 | 6 | 18 | 328 | 72 | 94 | 25 |
| 166 | 0 | 8 | n.d. | 88 | 0 | 5 | 149 | 168 | 0 | 16 |
| 169 | 0 | 5 | 28 | 92 | 0 | 1 | 120 | 9 | 69 | 2 |
| 171 | n.d. | 6 | n.d. | 140 | 0 | 1 | 243 | 124 | 0 | 0 |
| 175 | n.d. | 25 | n.d. | 62 | 0 | 4 | 208 | 105 | 7 | 14 |
| 176 | n.d. | 32 | 0 | 127 | 8 | 2 | 284 | 347 | 0 | 14 |
| 177 | 0 | 28 | 31 | 28 | 0 | 0 | 96 | 264 | 0 | 21 |
| 179 | 0 | 2 | n.d. | 89 | 0 | 6 | 193 | 108 | 0 | 14 |
| 181 | 0 | 5 | n.d. | 45 | 18 | 0 | 91 | 92 | 0 | 12 |
| 186 | n.d. | 39 | 33 | 20 | 0 | 15 | 206 | 0 | 76 | 25 |
| 191 | 0 | 3 | 11 | 126 | 9 | 5 | 154 | 34 | 0 | 20 |
| 196 | 0 | 6 | n.d. | 76 | 0 | 1 | 225 | 78 | 0 | 17 |
| 201 | 0 | 6 | n.d. | 76 | 0 | 1 | 225 | 78 | 0 | 17 |
| 206 | 0 | 9 | n.d. | 121 | 0 | 4 | 239 | 43 | 0 | 30 |
| 209 | n.d. | 0 | 36 | 79 | 0 | 19 | 187 | 97 | 0 | 13 |
| 211 | 0 | 1 | 19 | 110 | 0 | 1 | 151 | 106 | 25 | 23 |
| 212 | 0 | 3 | 22 | 9 | 0 | 0 | 55 | 115 | 43 | 28 |
| 214 | 0 | 0 | 11 | 157 | 0 | 7 | 463 | 0 | 0 | 21 |
| 216 | n.d. | 4 | 15 | 15 | 0 | 8 | 242 | 2 | 41 | 26 |
| 221 | n.d. | 50 | n.d. | 129 | 0 | 3 | 441 | 37 | 84 | 48 |
| 223 | 0 | 3 | 26 | 155 | 0 | 5 | 261 | 140 | 0 | 39 |
| 226 | n.d. | 1 | 32 | 68 | 0 | 0 | 243 | 119 | 0 | 25 |
| 233 | 0 | 24 | 0 | 294 | 10 | 0 | 326 | 38 | 13 | 0 |
| 239 | 0 | 18 | 0 | 51 | 4 | 2 | 123 | 187 | 0 | 28 |
| 240 | 0 | 4 | n.d. | 94 | 19 | 0 | 282 | 285 | 0 | 1 |
| 241 | 0 | 6 | n.d. | 77 | 0 | 0 | 279 | 269 | 0 | 11 |
| 246 | 0 | 4 | 0 | 81 | 0 | 10 | 101 | 162 | 0 | 2 |
| 256 | n.d. | 38 | 32 | 100 | 7 | 2 | 222 | 76 | 0 | 8 |
| 261 | 0 | 28 | n.d. | 128 | 11 | 4 | 222 | 175 | 4 | 1 |
| 265 | n.d. | 18 | 37 | 107 | 0 | 5 | 167 | 100 | 0 | 16 |
| 271 | 0 | 17 | 0 | 27 | 0 | 0 | 414 | 71 | 0 | 18 |
| 276 | 0 | 10 | 13 | 60 | 16 | 0 | 79 | 62 | 0 | 15 |
| 281 | n.d. | 32 | n.d. | 42 | 0 | 0 | 77 | 182 | 0 | 11 |
| 287 | n.d. | 19 | 0 | 145 | 17 | 9 | 423 | 119 | 69 | 10 |
| 291 | 0 | 1 | 21 | 126 | 0 | 5 | 162 | 80 | 58 | 23 |
| 295 | 0 | 6 | 31 | 33 | 0 | 1 | 62 | 50 | 0 | 24 |
| 301 | 0 | 8 | 0 | 130 | 0 | 10 | 235 | 96 | 2 | 21 |
| 306 | 0 | 12 | n.d. | 1 | 0 | 0 | 5 | 77 | 0 | 33 |
| 311 | 0 | 15 | 19 | 127 | 0 | 0 | 189 | 50 | 0 | 21 |
| 316 | n.d. | 11 | 30 | 139 | 7 | 17 | 361 | 52 | 0 | 19 |
| 321 | n.d. | 2 | n.d. | 57 | 3 | 0 | 398 | 37 | 50 | 21 |
| 325 | 0 | 3 | 13 | 99 | 0 | 4 | 232 | 66 | 0 | 27 |
| 326 | 0 | 11 | 0 | 18 | 6 | 0 | 362 | 84 | 55 | 11 |
| 331 | 0 | 13 | 0 | 69 | 0 | 5 | 167 | 29 | 34 | 9 |
| 335 | 0 | 35 | n.d. | 106 | 17 | 0 | 182 | 4 | 51 | 6 |
| 336 | n.d. | 22 | 0 | 217 | 0 | 6 | 214 | 62 | 12 | 19 |
| 341 | 20 | 9 | n.d. | 93 | 23 | 1 | 51 | 35 | 0 | 29 |

| Depth (cm) | Fe | Ga | Hf | Hg | La | Mn | Mo | Nb | Ni |
|---|---|---|---|---|---|---|---|---|---|
| 1 | 13847 | 0 | 0 | 1 | 0 | 1920 | 0 | 18 | 80 |
| 6 | 17594 | 0 | 0 | 16 | 125 | 2218 | 17 | 0 | 57 |
| 11 | 16679 | 0 | 2 | 10 | 20 | 2321 | 5 | 0 | 62 |
| 16 | 18977 | 0 | 1 | 5 | 100 | 2498 | 9 | 0 | 41 |
| 21 | 22529 | 0 | 0 | 6 | 120 | 3168 | 16 | 0 | 41 |
| 26 | 22067 | 0 | 1 | 1 | 86 | 3040 | 2 | 0 | 26 |
| 31 | 24864 | 0 | 0 | 2 | 197 | 3281 | 23 | 0 | 3 |
| 36 | 23401 | 0 | 0 | 5 | 140 | 3209 | 15 | 2 | 34 |
| 41 | 23326 | 1 | 1 | 2 | 195 | 2689 | 0 | 0 | 24 |
| 46 | 20465 | 2 | 1 | 15 | 0 | 3182 | 10 | 6 | 41 |
| 51 | 19635 | 0 | 1 | 12 | 36 | 2924 | 13 | 0 | 6 |
| 56 | 22666 | 0 | 1 | 7 | 135 | 2971 | 12 | 0 | 5 |
| 61 | 24240 | 4 | 0 | 0 | 132 | 3620 | 15 | 0 | 25 |
| 66 | 21843 | 0 | 0 | 0 | 255 | 2140 | 34 | 0 | 41 |
| 68 | 11627 | 0 | 1 | 9 | 6 | 2455 | 15 | 0 | 26 |
| 71 | 20370 | 0 | 1 | 20 | 57 | 2824 | 9 | 0 | 30 |
| 76 | 22749 | 0 | 0 | 1 | 83 | 3320 | 8 | 22 | 27 |
| 81 | 21994 | 0 | 0 | 20 | 6 | 3584 | 13 | 0 | 28 |
| 86 | 19735 | 1 | 1 | 12 | 21 | 3147 | 6 | 0 | 18 |
| 91 | 0 | 2 | 0 | 3 | 159 | 4944 | 19 | 0 | 9 |
| 96 | 17910 | 0 | 1 | 2 | 47 | 3392 | 12 | 0 | 17 |
| 101 | 15410 | 0 | 0 | 1 | 48 | 3320 | 0 | 0 | 2 |
| 106 | 16678 | 2 | 1 | 18 | 177 | 936 | 23 | 0 | 49 |
| 111 | 11445 | 0 | 0 | 13 | 0 | 2232 | 12 | 0 | 22 |
| 116 | 2266 | 0 | 0 | 9 | 115 | 1603 | 16 | 1 | 0 |
| 121 | 10908 | 0 | 0 | 29 | 26 | 4735 | 15 | 0 | 15 |
| 126 | 0 | 0 | 2 | 6 | 10 | 2817 | 17 | 0 | 22 |
| 131 | 19400 | 5 | 2 | 1 | 0 | 2343 | 11 | 0 | 22 |
| 135 | 6737 | 2 | 0 | 9 | 206 | 1664 | 8 | 0 | 21 |
| 136 | 22596 | 0 | 0 | 14 | 128 | 2385 | 23 | 0 | 12 |
| 138 | 3477 | 0 | 2 | 12 | 66 | 2036 | 21 | 16 | 14 |
| 141 | 19138 | 0 | 0 | 7 | 17 | 3278 | 0 | 0 | 19 |
| 146 | 16292 | 0 | 0 | 7 | 9 | 1388 | 0 | 0 | 27 |
| 151 | 19575 | 3 | 0 | 0 | 78 | 1960 | 1 | 2 | 18 |
| 156 | 19702 | 0 | 2 | 2 | 0 | 2010 | 5 | 0 | 20 |
| 161 | 18683 | 0 | 0 | 13 | 169 | 974 | 10 | 0 | 15 |
| 163 | 16390 | 5 | 0 | 4 | 182 | 826 | 4 | 0 | 9 |
| 166 | 11851 | 0 | 0 | 1 | 0 | 1678 | 0 | 0 | 10 |
| 169 | 28373 | 0 | 1 | 13 | 50 | 890 | 0 | 0 | 10 |
| 171 | 45486 | 1 | 0 | 4 | 0 | 1411 | 20 | 0 | 3 |
| 175 | 54003 | 0 | 0 | 0 | 64 | 3250 | 32 | 0 | 12 |
| 176 | 0 | 0 | 1 | 3 | 60 | 62316 | 79 | 0 | 0 |
| 177 | 0 | 0 | 0 | 14 | 37 | 36991 | 35 | 0 | 18 |
| 179 | 0 | 0 | 0 | 11 | 144 | 4396 | 4 | 0 | 17 |
| 181 | 32814 | 0 | 2 | 0 | 69 | 4819 | 39 | 2 | 23 |
| 186 | 32069 | 0 | 0 | 5 | 31 | 2611 | 14 | 0 | 26 |
| 191 | 16439 | 0 | 1 | 21 | 0 | 1227 | 5 | 0 | 12 |
| 196 | 16448 | 0 | 0 | 1 | 0 | 1860 | 7 | 0 | 1 |
| 201 | 16448 | 0 | 0 | 1 | 0 | 1860 | 7 | 0 | 1 |
| 206 | 20537 | 0 | 2 | 8 | 49 | 3006 | 0 | 0 | 31 |
| 209 | 4373 | 0 | 2 | 3 | 0 | 1201 | 10 | 0 | 3 |
| 211 | 32878 | 0 | 1 | 9 | 115 | 1385 | 1 | 0 | 10 |
| 212 | 66083 | 0 | 0 | 3 | 148 | 1498 | 54 | 5 | 2 |
| 214 | 26269 | 0 | 1 | 12 | 0 | 1666 | 4 | 0 | 18 |
| 216 | 66746 | 0 | 0 | 6 | 38 | 1782 | 54 | 0 | 10 |
| 221 | 38976 | 3 | 0 | 8 | 175 | 3742 | 0 | 0 | 45 |
| 223 | 0 | 0 | 0 | 13 | 74 | 14925 | 0 | 0 | 17 |
| 226 | 0 | 0 | 0 | 5 | 113 | 14344 | 24 | 0 | 0 |
| 233 | 13793 | 0 | 2 | 13 | 130 | 2004 | 57 | 3 | 24 |
| 239 | 0 | 0 | 0 | 0 | 49 | 32443 | 8 | 0 | 19 |
| 240 | 0 | 0 | 1 | 4 | 214 | 39015 | 5 | 0 | 15 |
| 241 | 0 | 0 | 0 | 5 | 101 | 34863 | 9 | 0 | 0 |
| 246 | 0 | 0 | 0 | 0 | 109 | 14830 | 0 | 3 | 0 |
| 256 | 46428 | 0 | 0 | 8 | 184 | 19369 | 29 | 17 | 10 |
| 261 | 66277 | 0 | 2 | 0 | 163 | 3590 | 34 | 8 | 10 |
| 265 | 43011 | 0 | 2 | 3 | 51 | 5022 | 30 | 0 | 3 |
| 271 | 42938 | 1 | 0 | 0 | 127 | 3493 | 36 | 0 | 0 |
| 276 | 36526 | 1 | 1 | 0 | 121 | 1661 | 12 | 5 | 3 |
| 281 | 64037 | 0 | 0 | 12 | 60 | 3504 | 57 | 0 | 14 |
| 287 | 49946 | 1 | 0 | 0 | 198 | 1364 | 36 | 4 | 0 |
| 291 | 32105 | 0 | 1 | 4 | 160 | 1200 | 5 | 0 | 15 |
| 295 | 18393 | 0 | 0 | 8 | 29 | 1425 | 22 | 0 | 8 |
| 301 | 23977 | 1 | 1 | 0 | 146 | 2118 | 0 | 0 | 23 |
| 306 | 19748 | 3 | 1 | 6 | 0 | 2453 | 0 | 0 | 23 |
| 311 | 24300 | 0 | 0 | 3 | 141 | 2068 | 32 | 0 | 20 |
| 316 | 24820 | 3 | 0 | 1 | 178 | 1709 | 12 | 0 | 5 |
| 321 | 24397 | 0 | 0 | 15 | 227 | 1499 | 22 | 0 | 8 |
| 325 | 22356 | 0 | 0 | 11 | 17 | 1482 | 2 | 0 | 0 |
| 326 | 11716 | 1 | 1 | 8 | 197 | 0 | 0 | 0 | 29 |
| 331 | 23957 | 0 | 1 | 0 | 183 | 1585 | 2 | 1 | 26 |
| 335 | 27005 | 0 | 1 | 13 | 244 | 378 | 14 | 4 | 8 |
| 336 | 29125 | 0 | 1 | 0 | 61 | 2188 | 7 | 0 | 33 |
| 341 | 22436 | 3 | 1 | 0 | 10 | 2311 | 0 | 0 | 19 |

| Depth (cm) | Pb | Pd | Pt | Rb | Rh | Sb | Se | Sn | Sr |
|---|---|---|---|---|---|---|---|---|---|
| **1** | 28 | n.d. | 57 | 1 | 0 | 14 | 0 | 0 | 653 |
| **6** | 0 | 25 | 0 | 17 | 89 | 0 | 7 | 0 | 700 |
| **11** | 0 | 0 | 0 | 20 | 0 | 99 | 5 | 18 | 728 |
| **16** | 9 | 0 | 0 | 21 | 0 | 3 | 1 | 8 | 734 |
| **21** | 7 | 0 | n.d. | 14 | n.d. | 13 | 0 | 0 | 770 |
| **26** | 29 | 0 | 14 | 15 | n.d. | 31 | 0 | 0 | 673 |
| **31** | 19 | 0 | 0 | 16 | 67 | 60 | 0 | 2 | 804 |
| **36** | 7 | 0 | 0 | 17 | n.d. | 2 | 0 | 18 | 649 |
| **41** | 10 | 22 | n.d. | 18 | 48 | 43 | 0 | 0 | 725 |
| **46** | 0 | 0 | n.d. | 15 | n.d. | 17 | 0 | 14 | 701 |
| **51** | 0 | 23 | 0 | 16 | n.d. | 80 | 3 | 11 | 672 |
| **56** | 2 | n.d. | n.d. | 15 | n.d. | 42 | 0 | 0 | 707 |
| **61** | 1 | 14 | 0 | 21 | 42 | 34 | 2 | 0 | 729 |
| **66** | 8 | 0 | 10 | 19 | 202 | 33 | 0 | 0 | 768 |
| **68** | 32 | 0 | 14 | 11 | 40 | 0 | 0 | 0 | 883 |
| **71** | 0 | n.d. | 0 | 14 | n.d. | 0 | 2 | 7 | 705 |
| **76** | 3 | 42 | n.d. | 9 | n.d. | 43 | 0 | 0 | 717 |
| **81** | 12 | n.d. | 23 | 17 | 53 | 11 | 1 | 7 | 686 |
| **86** | 5 | 0 | n.d. | 22 | n.d. | 17 | 0 | 0 | 710 |
| **91** | 0 | 0 | 0 | 17 | 109 | 62 | 4 | 0 | 655 |
| **96** | 4 | 0 | 21 | 13 | n.d. | 6 | 0 | 0 | 702 |
| **101** | 5 | 0 | 13 | 16 | 245 | 74 | 0 | 11 | 744 |
| **106** | 12 | 0 | n.d. | 12 | 256 | 54 | 0 | 0 | 654 |
| **111** | 23 | n.d. | 0 | 16 | 48 | 1 | 0 | 0 | 681 |
| **116** | 58 | n.d. | n.d. | 10 | 0 | 6 | 0 | 0 | 493 |
| **121** | 34 | n.d. | 27 | 5 | n.d. | 0 | 0 | 0 | 604 |
| **126** | 35 | 0 | 38 | 16 | n.d. | 61 | 0 | 0 | 953 |
| **131** | 13 | n.d. | 0 | 16 | 0 | 65 | 3 | 0 | 790 |
| **135** | 25 | 0 | 0 | 15 | n.d. | 45 | 0 | 10 | 1136 |
| **136** | 13 | 0 | 11 | 27 | n.d. | 42 | 0 | 0 | 654 |
| **138** | 0 | 15 | 0 | 18 | n.d. | 101 | 8 | 0 | 823 |
| **141** | 15 | 0 | n.d. | 13 | n.d. | 0 | 0 | 0 | 712 |
| **146** | 62 | n.d. | n.d. | 11 | n.d. | 81 | 0 | 0 | 508 |
| **151** | 30 | 0 | n.d. | 14 | 95 | 27 | 0 | 0 | 704 |
| **156** | 27 | 0 | 19 | 15 | n.d. | 20 | 0 | 21 | 764 |
| **161** | 11 | 0 | n.d. | 14 | 50 | 0 | 0 | 0 | 660 |
| **163** | 14 | 19 | 0 | 13 | 0 | 91 | 0 | 12 | 602 |
| **166** | 15 | 0 | 15 | 17 | n.d. | 0 | 0 | 0 | 632 |
| **169** | 15 | 0 | 12 | 10 | n.d. | 0 | 0 | 0 | 468 |
| **171** | 24 | 0 | n.d. | 14 | 43 | 19 | 0 | 0 | 385 |
| **175** | 36 | 0 | 22 | 14 | n.d. | 52 | 0 | 0 | 247 |
| **176** | 13 | 0 | n.d. | 11 | 44 | 76 | 0 | 11 | 250 |
| **177** | 37 | 0 | 11 | 10 | n.d. | 27 | 0 | 0 | 280 |
| **179** | 1 | 0 | 69 | 11 | n.d. | 38 | 0 | 19 | 656 |
| **181** | 0 | 0 | 0 | 12 | n.d. | 43 | 2 | 0 | 510 |
| **186** | 7 | 0 | n.d. | 8 | 0 | 0 | 0 | 0 | 608 |
| **191** | 2 | 12 | n.d. | 9 | n.d. | 16 | 0 | 0 | 620 |
| **196** | 5 | 0 | 29 | 14 | 87 | 0 | 0 | 0 | 739 |
| **201** | 5 | 0 | 29 | 14 | 87 | 0 | 0 | 0 | 739 |
| **206** | 0 | n.d. | 0 | 15 | 0 | 0 | 2 | 5 | 636 |
| **209** | 14 | 0 | 18 | 0 | n.d. | 65 | 0 | 0 | 536 |
| **211** | 2 | n.d. | 0 | 13 | n.d. | 32 | 0 | 0 | 249 |
| **212** | 0 | 14 | 0 | 12 | n.d. | 13 | 6 | 0 | 267 |
| **214** | 16 | 0 | 15 | 8 | n.d. | 10 | 0 | 2 | 973 |
| **216** | 2 | 0 | 0 | 14 | n.d. | 50 | 4 | 0 | 329 |
| **221** | 13 | n.d. | 10 | 12 | 0 | 23 | 1 | 44 | 635 |
| **223** | 13 | 0 | 31 | 9 | 0 | 37 | 0 | 0 | 649 |
| **226** | 16 | 0 | 43 | 8 | 407 | 33 | 0 | 0 | 597 |
| **233** | 0 | n.d. | 0 | 21 | 179 | 46 | 2 | 17 | 922 |
| **239** | 11 | 0 | n.d. | 12 | 49 | 52 | 0 | 10 | 366 |
| **240** | 0 | n.d. | n.d. | 15 | n.d. | 35 | 0 | 6 | 538 |
| **241** | 0 | 12 | 0 | 21 | 0 | 6 | 9 | 0 | 431 |
| **246** | 14 | 0 | 0 | 14 | 0 | 0 | 1 | 0 | 322 |
| **256** | 3 | 24 | 0 | 10 | n.d. | 43 | 0 | 18 | 283 |
| **261** | 0 | 13 | 0 | 15 | 43 | 5 | 3 | 0 | 288 |
| **265** | 13 | 26 | 20 | 11 | n.d. | 10 | 0 | 0 | 386 |
| **271** | 0 | 31 | 0 | 11 | n.d. | 57 | 5 | 8 | 335 |
| **276** | 0 | 0 | n.d. | 15 | 0 | 10 | 0 | 0 | 443 |
| **281** | 0 | 0 | 0 | 9 | n.d. | 11 | 5 | 0 | 321 |
| **287** | 0 | 28 | 0 | 12 | n.d. | 84 | 6 | 0 | 456 |
| **291** | 9 | 32 | n.d. | 14 | n.d. | 3 | 0 | 0 | 353 |
| **295** | 19 | 0 | n.d. | 11 | 0 | 35 | 0 | 0 | 680 |
| **301** | 10 | 0 | 0 | 21 | n.d. | 27 | 2 | 28 | 713 |
| **306** | 24 | 0 | n.d. | 13 | 0 | 0 | 0 | 0 | 604 |
| **311** | 6 | 0 | n.d. | 15 | 80 | 0 | 0 | 0 | 677 |
| **316** | 7 | 14 | n.d. | 15 | n.d. | 22 | 0 | 23 | 695 |
| **321** | 13 | 0 | 12 | 18 | 72 | 69 | 0 | 5 | 738 |
| **325** | 14 | 15 | 26 | 16 | 124 | 39 | 0 | 0 | 598 |
| **326** | 0 | n.d. | 0 | 23 | 0 | 0 | 4 | 52 | 416 |
| **331** | 11 | 23 | 0 | 22 | 64 | 61 | 3 | 17 | 686 |
| **335** | 2 | 13 | n.d. | 16 | n.d. | 23 | 1 | 3 | 479 |
| **336** | 0 | 21 | 0 | 22 | 141 | 45 | 2 | 25 | 750 |
| **341** | 0 | 19 | 0 | 25 | n.d. | 30 | 1 | 3 | 760 |

| Depth (cm) | Ta | Te | Th | Tl | U | V | W | Y | Zn | Zr |
|---|---|---|---|---|---|---|---|---|---|---|
| 1 | 0 | 4 | 12 | 8 | 0 | 363 | 0 | 6 | 99 | 0 |
| 6 | 39 | 4 | 0 | 0 | 15 | 0 | 0 | 15 | 101 | 0 |
| 11 | 14 | 2 | 0 | 7 | 0 | 92 | 4 | 12 | 112 | 0 |
| 16 | 41 | 0 | 1 | 3 | 0 | 0 | 0 | 13 | 114 | 0 |
| 21 | 0 | 2 | 0 | 0 | 0 | 0 | 0 | 19 | 146 | 0 |
| 26 | 0 | 2 | 5 | 6 | 0 | 0 | 0 | 4 | 131 | 0 |
| 31 | 19 | 7 | 9 | 3 | 11 | 0 | 0 | 15 | 134 | 0 |
| 36 | 13 | 4 | 5 | 1 | 0 | 0 | 0 | 9 | 127 | 0 |
| 41 | 0 | 2 | 0 | 3 | 0 | 0 | 0 | 11 | 124 | 0 |
| 46 | 0 | 2 | 0 | 1 | 0 | 160 | 0 | 3 | 118 | 0 |
| 51 | 39 | 5 | 6 | 3 | 0 | 110 | 0 | 12 | 141 | 0 |
| 56 | 0 | 3 | 10 | 0 | 0 | 0 | 0 | 16 | 142 | 0 |
| 61 | 0 | 1 | 0 | 3 | 0 | 0 | 0 | 2 | 152 | 0 |
| 66 | 0 | 0 | 17 | 7 | 44 | 0 | 0 | 24 | 157 | 0 |
| 68 | 0 | 3 | 0 | 2 | 0 | 305 | 0 | 18 | 611 | 0 |
| 71 | 70 | 4 | 0 | 7 | 0 | 0 | 0 | 12 | 178 | 0 |
| 76 | 0 | 6 | 3 | 4 | 0 | 0 | 0 | 4 | 202 | 0 |
| 81 | 0 | 3 | 0 | 3 | 4 | 216 | 0 | 10 | 247 | 0 |
| 86 | 0 | 0 | 9 | 8 | 0 | 280 | 0 | 8 | 256 | 0 |
| 91 | 0 | 4 | 0 | 2 | 7 | 0 | 0 | 0 | 245 | 0 |
| 96 | 0 | 4 | 2 | 4 | 0 | 0 | 0 | 12 | 389 | 0 |
| 101 | 0 | 2 | 19 | 5 | 42 | 0 | 0 | 3 | 463 | 0 |
| 106 | 0 | 3 | 5 | 3 | 40 | 0 | 0 | 13 | 548 | 0 |
| 111 | 5 | 5 | 0 | 1 | 0 | 307 | 0 | 23 | 1397 | 0 |
| 116 | 0 | 1 | 1 | 0 | 0 | 0 | 0 | 3 | 1546 | 0 |
| 121 | 0 | 0 | 4 | 2 | 0 | 0 | 0 | 11 | 1274 | 0 |
| 126 | 0 | 1 | 6 | 2 | 0 | 157 | 0 | 11 | 657 | 0 |
| 131 | 0 | 1 | 5 | 8 | 0 | 92 | 0 | 12 | 678 | 0 |
| 135 | 0 | 2 | 0 | 0 | 0 | 0 | 0 | 4 | 666 | 0 |
| 136 | 0 | 3 | 11 | 9 | 0 | 0 | 0 | 14 | 572 | 0 |
| 138 | 0 | 7 | 0 | 2 | 0 | 0 | 0 | 0 | 487 | 0 |
| 141 | 0 | 0 | 0 | 0 | 0 | 107 | 0 | 6 | 625 | 0 |
| 146 | 0 | 2 | 0 | 0 | 0 | 27 | 0 | 11 | 958 | 0 |
| 151 | 0 | 0 | 10 | 3 | 19 | 0 | 0 | 3 | 611 | 0 |
| 156 | 0 | 4 | 19 | 12 | 0 | 184 | 0 | 11 | 481 | 0 |
| 161 | 0 | 0 | 17 | 0 | 0 | 0 | 0 | 3 | 405 | 0 |
| 163 | 0 | 0 | 0 | 4 | 0 | 0 | 0 | 7 | 381 | 0 |
| 166 | 0 | 0 | 9 | 5 | 0 | 229 | 0 | 13 | 390 | 0 |
| 169 | 0 | 0 | 0 | 2 | 0 | 0 | 0 | 6 | 450 | 0 |
| 171 | 0 | 0 | 8 | 1 | 9 | 106 | 0 | 0 | 528 | 0 |
| 175 | 0 | 8 | 7 | 7 | 0 | 0 | 0 | 0 | 532 | 0 |
| 176 | 24 | 4 | 0 | 4 | 0 | 0 | 4 | 5 | 449 | 0 |
| 177 | 0 | 2 | 5 | 0 | 0 | 0 | 0 | 0 | 435 | 0 |
| 179 | 0 | 3 | 18 | 1 | 0 | 0 | 0 | 13 | 123 | 0 |
| 181 | 9 | 5 | 0 | 5 | 0 | 0 | 0 | 0 | 104 | 0 |
| 186 | 0 | 0 | 11 | 14 | 11 | 0 | 0 | 4 | 86 | 0 |
| 191 | 0 | 0 | 0 | 2 | 0 | 202 | 0 | 10 | 58 | 0 |
| 196 | 0 | 0 | 21 | 2 | 20 | 245 | 0 | 6 | 96 | 0 |
| 201 | 0 | 0 | 21 | 2 | 20 | 245 | 0 | 6 | 96 | 0 |
| 206 | 0 | 2 | 1 | 1 | 2 | 0 | 0 | 9 | 128 | 0 |
| 209 | 0 | 2 | 0 | 6 | 0 | 298 | 0 | 6 | 65 | 0 |
| 211 | 8 | 0 | 8 | 0 | 0 | 0 | 0 | 72 | 0 | 0 |
| 212 | 9 | 0 | 7 | 6 | 0 | 0 | 0 | 8 | 95 | 0 |
| 214 | 0 | 4 | 0 | 3 | 12 | 319 | 0 | 8 | 88 | 0 |
| 216 | 19 | 2 | 12 | 5 | 19 | 0 | 0 | 2 | 117 | 0 |
| 221 | 0 | 6 | 0 | 3 | 0 | 0 | 0 | 3 | 118 | 0 |
| 223 | 0 | 4 | 5 | 12 | 0 | 0 | 0 | 2 | 62 | 0 |
| 226 | 0 | 0 | 20 | 4 | 56 | 0 | 0 | 6 | 50 | 0 |
| 233 | 32 | 6 | 0 | 5 | 29 | 0 | 0 | 11 | 61 | 0 |
| 239 | 0 | 6 | 0 | 15 | 23 | 0 | 16 | 15 | 78 | 0 |
| 240 | 49 | 0 | 0 | 1 | 13 | 0 | 0 | 3 | 64 | 0 |
| 241 | 9 | 0 | 17 | 13 | 3 | 0 | 0 | 1 | 52 | 0 |
| 246 | 5 | 0 | 0 | 2 | 0 | 0 | 0 | 0 | 51 | 0 |
| 256 | 8 | 3 | 0 | 8 | 2 | 0 | 0 | 0 | 74 | 0 |
| 261 | 24 | 2 | 0 | 0 | 29 | 0 | 17 | 8 | 54 | 0 |
| 265 | 0 | 3 | 13 | 3 | 0 | 0 | 0 | 12 | 42 | 0 |
| 271 | 0 | 5 | 20 | 9 | 8 | 0 | 30 | 1 | 49 | 0 |
| 276 | 0 | 0 | 0 | 16 | 0 | 0 | 0 | 0 | 105 | 0 |
| 281 | 3 | 0 | 17 | 4 | 0 | 0 | 0 | 2 | 58 | 0 |
| 287 | 7 | 1 | 0 | 2 | 0 | 0 | 17 | 4 | 49 | 0 |
| 291 | 6 | 0 | 20 | 11 | 1 | 0 | 0 | 5 | 48 | 0 |
| 295 | 0 | 1 | 0 | 0 | 0 | 0 | 0 | 3 | 126 | 0 |
| 301 | 7 | 1 | 7 | 3 | 13 | 0 | 33 | 15 | 58 | 0 |
| 306 | 0 | 2 | 5 | 0 | 0 | 132 | 0 | 10 | 68 | 0 |
| 311 | 0 | 1 | 10 | 5 | 18 | 0 | 0 | 16 | 61 | 0 |
| 316 | 0 | 2 | 0 | 0 | 0 | 0 | 0 | 24 | 67 | 0 |
| 321 | 0 | 4 | 0 | 8 | 19 | 0 | 0 | 21 | 63 | 0 |
| 325 | 0 | 5 | 5 | 0 | 36 | 169 | 0 | 11 | 71 | 0 |
| 326 | 0 | 7 | 0 | 0 | 0 | 0 | 0 | 10 | 73 | 0 |
| 331 | 24 | 2 | 16 | 3 | 18 | 0 | 2 | 19 | 77 | 0 |
| 335 | 20 | 4 | 0 | 11 | 11 | 0 | 0 | 2 | 67 | 0 |
| 336 | 7 | 6 | 15 | 15 | 40 | 0 | 0 | 9 | 78 | 0 |
| 341 | 0 | 8 | 0 | 3 | 0 | 71 | 0 | 6 | 84 | 0 |

## 6.4. Micropaleontological Analysis

Even though the occurrence of benthic foraminifera in the Discovery Deep deposit shows obvious downcore variability, the specimens exhibit consistently low abundances, with a few exceptions. A total of ~65 different benthic foraminifera species were identified in the examined samples. Among them the genera *Bolivina*, *Eggerella* and *Globocassidulina* along with Miliolids are the most abundant. Besides the dominant benthic foraminifera, the genera *Cymbaloporeta* sp., Anomalinoides sp., *Cassidulina* spp., *Fissurina* spp., *Lagena* spp., *Melonis* spp., *Cibicides* spp. and *Gyroidinoides* spp. frequently appear (Figure 27), but in low abundances.

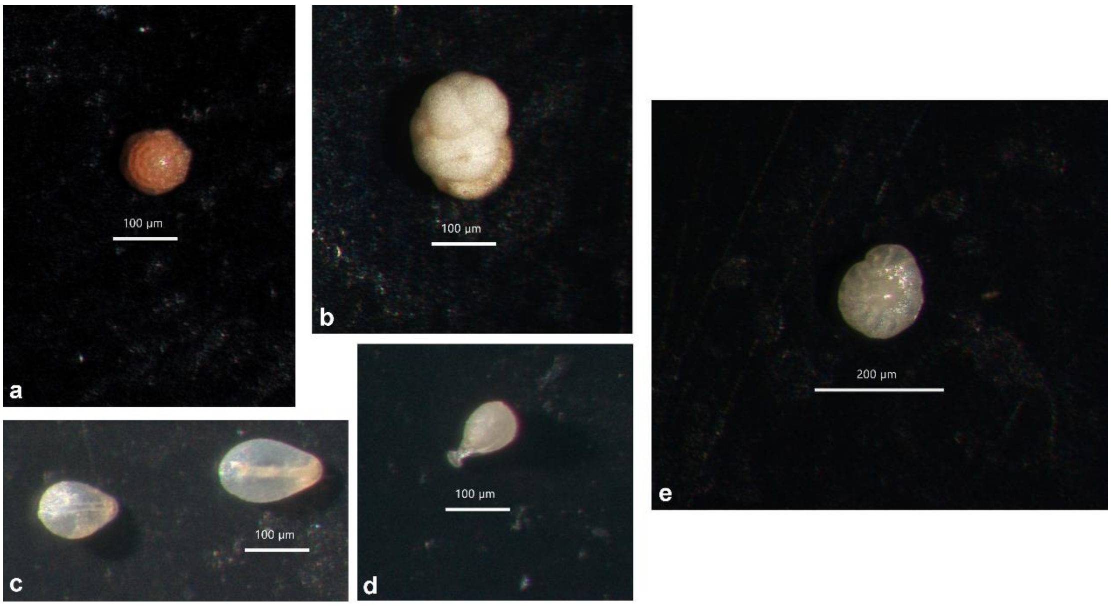


**Figure 27:** *Benthic foraminifera identified in the Discovery Deep core. (a) Cymbaloporeta sp.; (b) Cassidulina sp.; (c) Fissurina sp.; (d) Lagena sp.; (e) Cibicides sp.*

The downcore distribution of the dominant foraminiferal taxa is presented in Figure 28. *Bolivina* is a shallow infaunal, opportunistic taxon, often associated with oxygen-depleted environments (Kaiho, 1994; Jorissen, 1999). Individuals of *Bolivina* spp. (Figure 29) are present throughout the entire core, with their relative abundance consistently exceeding 10% (average of 20.1%). The abundances exhibit continuous changes, varying from 8.6% to 37.8% and showing two peaks occurring in Unit A at

40-41cm (2.05 cal ka BP) and at the top of Unit C (15.77 cal ka BP). *Eggerella* spp. are the primary species present (Figure 30), characterized by the highest average relative abundance (26.2%). *Eggerella* species are infaunal, tolerant to low-oxygen conditions (Langlet et al., 2014; Cesbron et al., 2016). The downcore abundance of *Eggerella* spp. shows an increasing trend in Unit A, followed by a drop in Unit B and being completely absent at 210-211 cm (6.5 cal ka BP). However, a sharp increase appears at 267-268 cm (12.34 cal ka BP; near the end of "Late" Pleistocene), corresponding to a maximum value of 60%, while deeper in the core, in Unit C, the *Eggerella* spp. abundance reduces to an almost constant value of ~17%. *Globocassidulina*, the third dominant genus in the core, is an epifaunal protist thriving in high-oxygen environments (Kaiho, 1994) and is mostly represented by the species *Globocassidulina subglobosa* (Figure 31), (0-33.6%, average of 6.3%). It demonstrates relatively low abundances in the uppermost part of the core, showing two significant peaks, the bigger one at 240-241 cm (9.25 cal ka BP) and the smaller one at 87-88 cm (2.43 cal ka BP). However, deeper than ~270 cm and throughout the entire Unit C, approaching the Last Glacial Maximum, *Globocassidulina* spp. are absent. Finally, the relative abundance of Miliolids (Figure 32) varies between 4% and 25% (average of 15.2%), displaying a downward increasing trend, interrupted by a significant drop prior to the onset of Holocene and followed by an equally significant increase (>20%) at the top of Unit C during MIS-2.

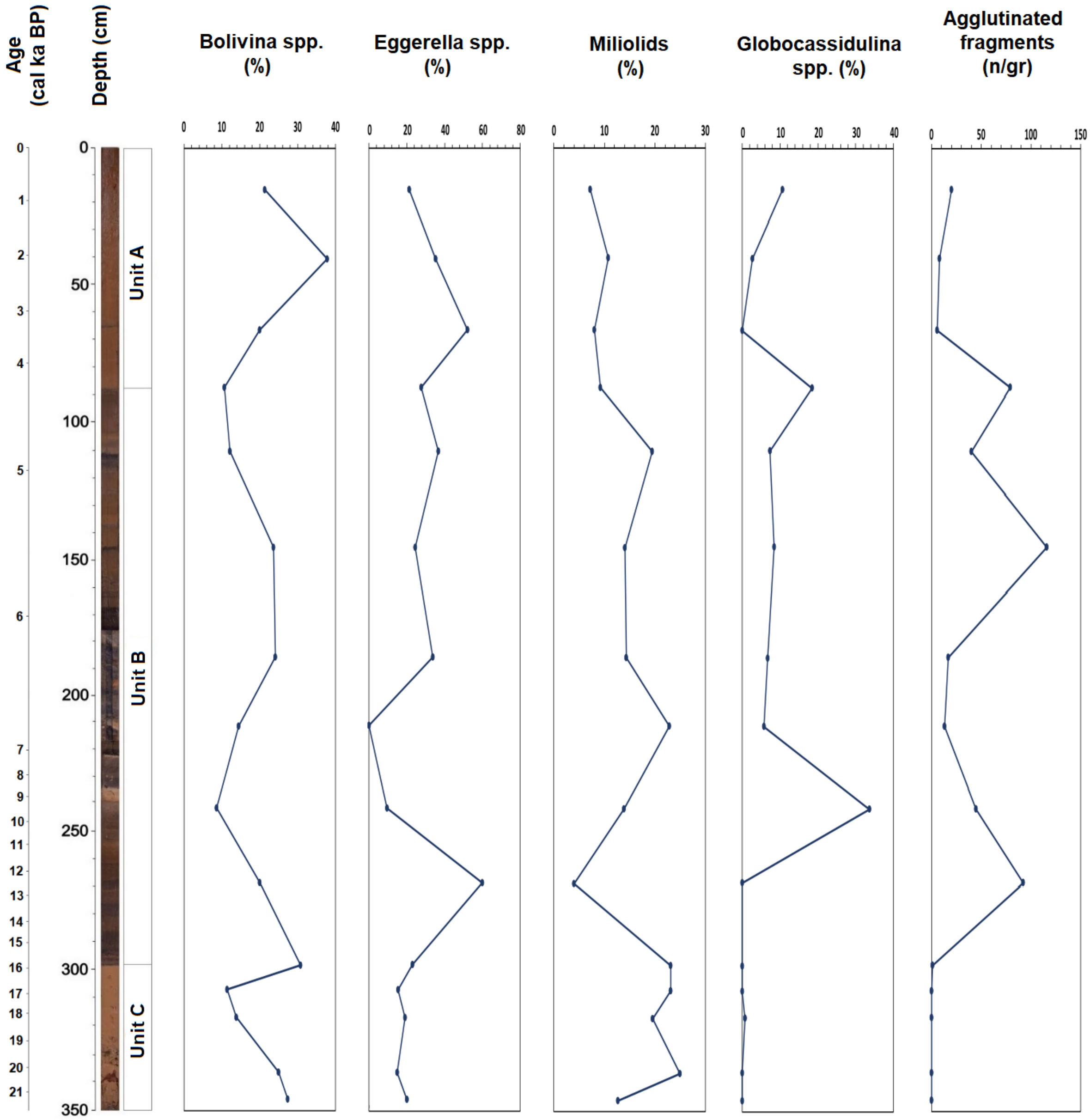


**Figure 28:** *Downcore relative abundance of the dominant genera of benthic foraminifera in the Discovery Deep core.*

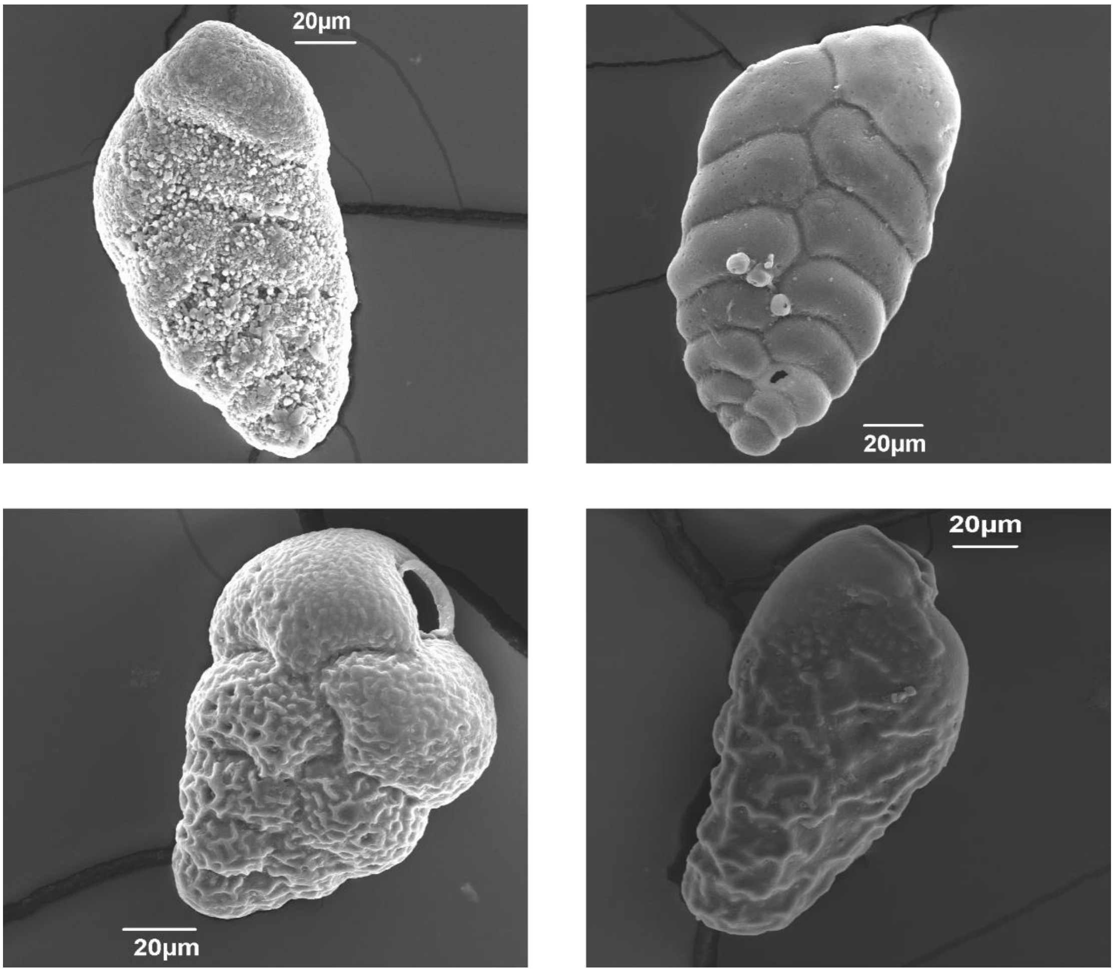


**Figure 29:** *Bolivina spp. from the Discovery Deep core (SEM images).*

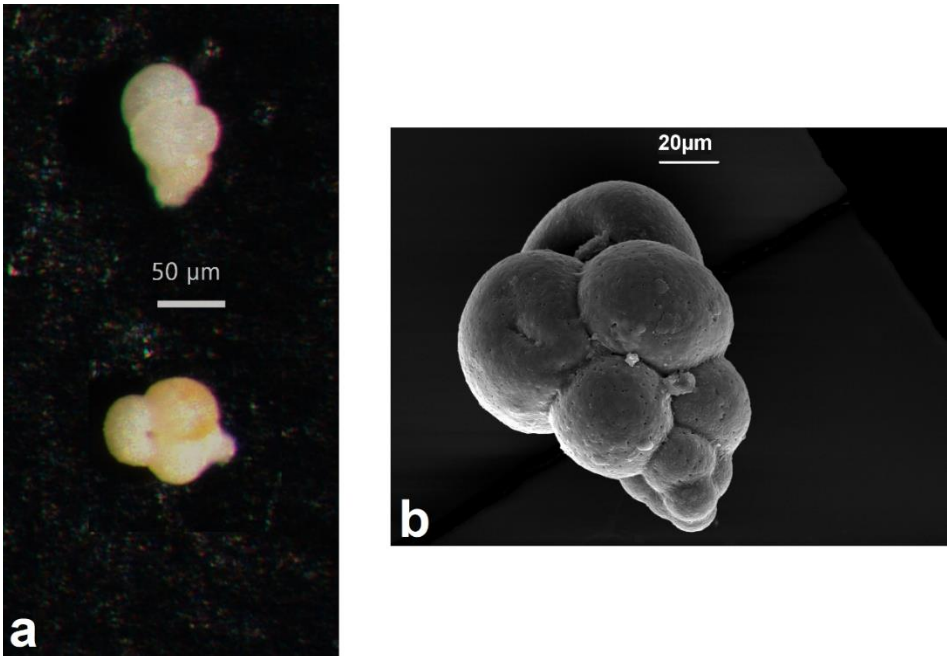


**Figure 30:** Eggerella spp. from the Discovery Deep core. (a) Stereoscope image; and (b) SEM image.

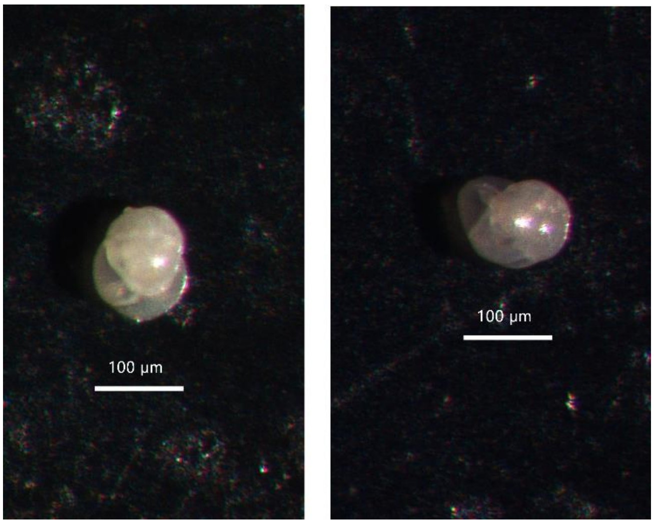


**Figure 31:** *Globocassidulina sp. from the Discovery Deep core (stereoscope images).*

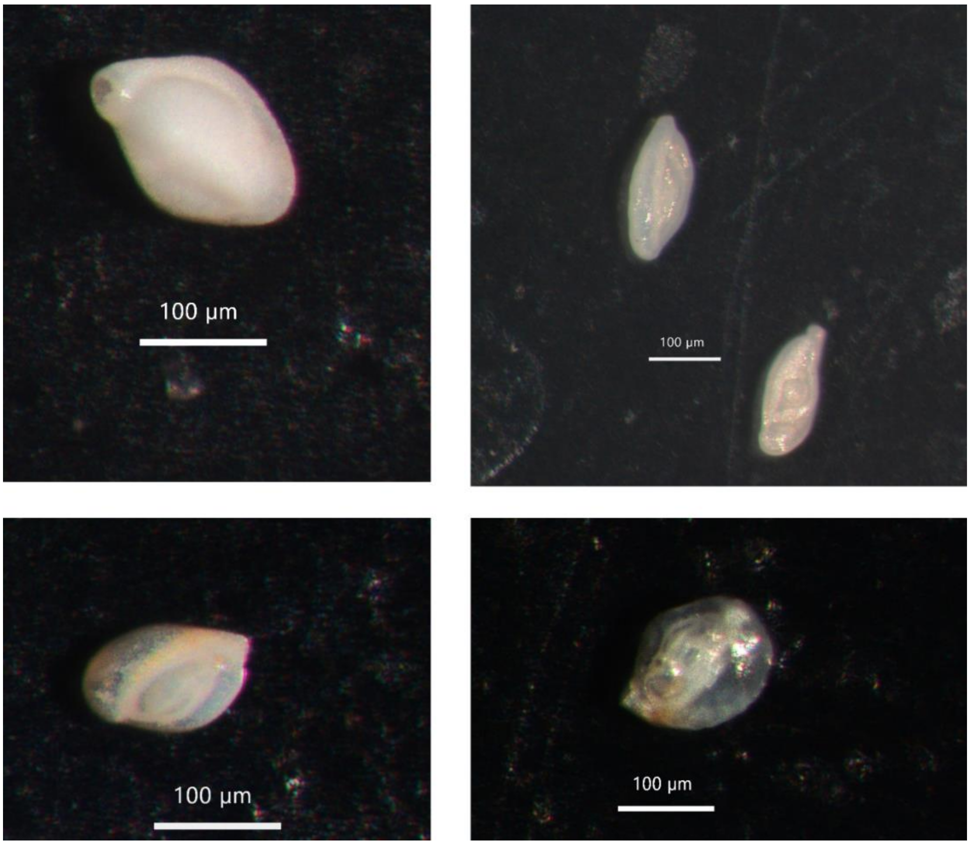


**Figure 32:** *Miliolids (stereoscope images).*

Concerning the indices estimated for the assessment of the benthic foraminiferal community (Figure 33) in the Discovery Deep core, the BFN index appears rather low, showing values mostly ranging from 6 to 58 specimens per gram for most of the examined samples. Only two significant peaks in the benthic population are observed, exceeding 200 individuals per gram. The first one occures at 145-146 cm (5.53 cal ka BP) and the second at 316-317 cm (17.94 cal ka BP). The D diversity index varies between 0.06 and 0.3, showing an average of 0.12, indicating low dominance levels, i.e., there is not any particular taxon that clearly dominates the benthic community. The J diversity index ranges from 0.49 to 0.96, with an average value of 0.75, suggesting that the microfauna community in the Discovery Deep deposit is characterized by moderate to high equilibrium conditions. The S diversity index varies from 7 to 53, with an average of 20 different taxa per sample and a significant peak at 316-317 cm (17.94 cal ka BP). Finally, the benthic foraminiferal diversity, expressed by the H' (1.53-3.3, with an average of 2.55) and a-index (4.75-67.63, with an average of 26.02), shows values, which in combination with the S index, suggests a moderately high foraminiferal heterogeneity, without, in general, any striking differences between the lithological Units A, B and C.

**Figure 33:** Downcore distribution of the absolute abundance *(BFN, n·g*[-1]*) and of the diversity parameters (D: Dominance index, J: Evenness, S: Species richness, H': Shannon-Wiener index and, finally, Fisher's a-index).*

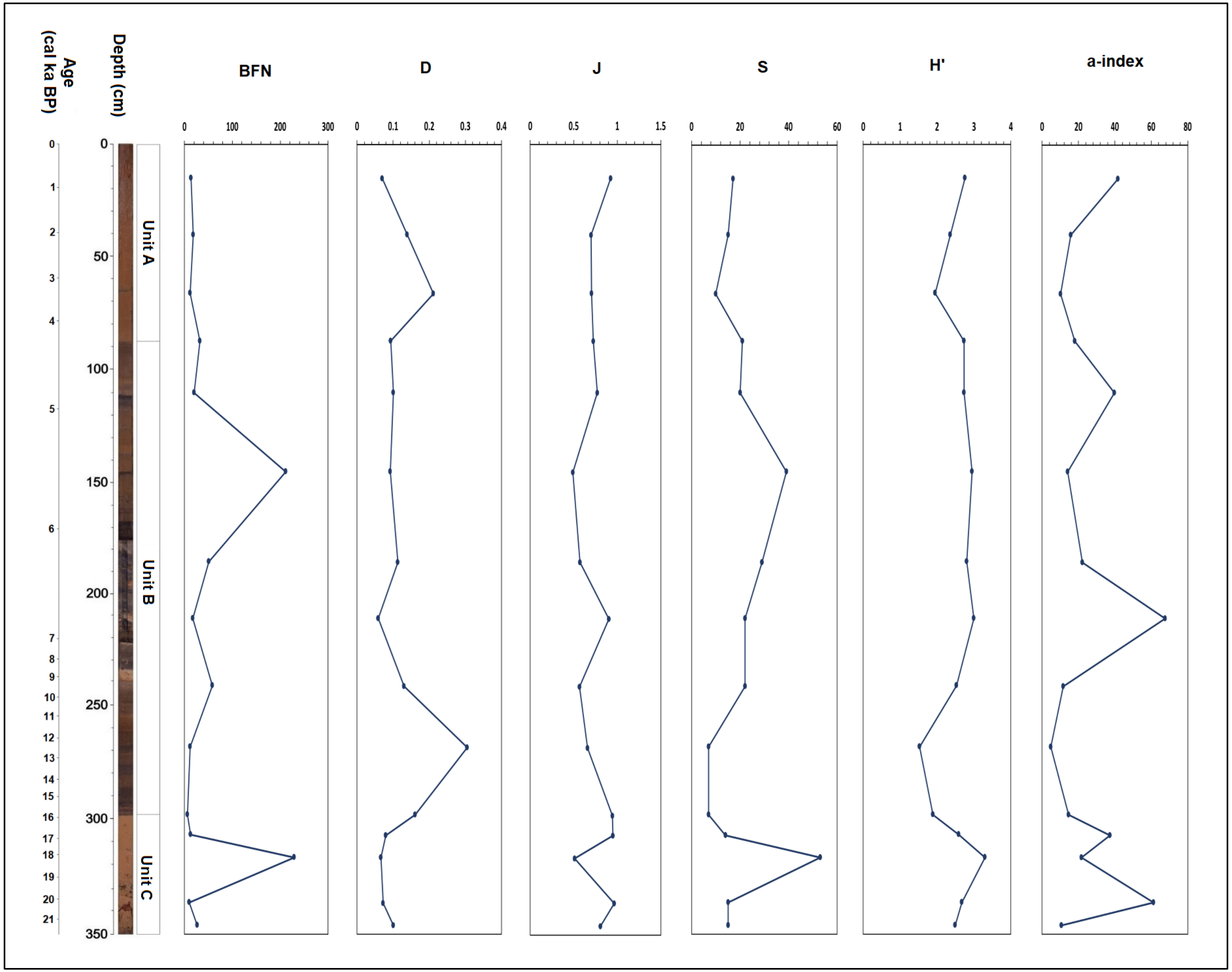

It should be emphasized that a noteworthy observation about the condition of the identified benthic fauna within Unit B is the fact that the majority of the foraminifera specimens are coated with crystal-like particles (Figure 34), while in the same unit agglutinated fragments predominantly occur (see Figure 28, 35).

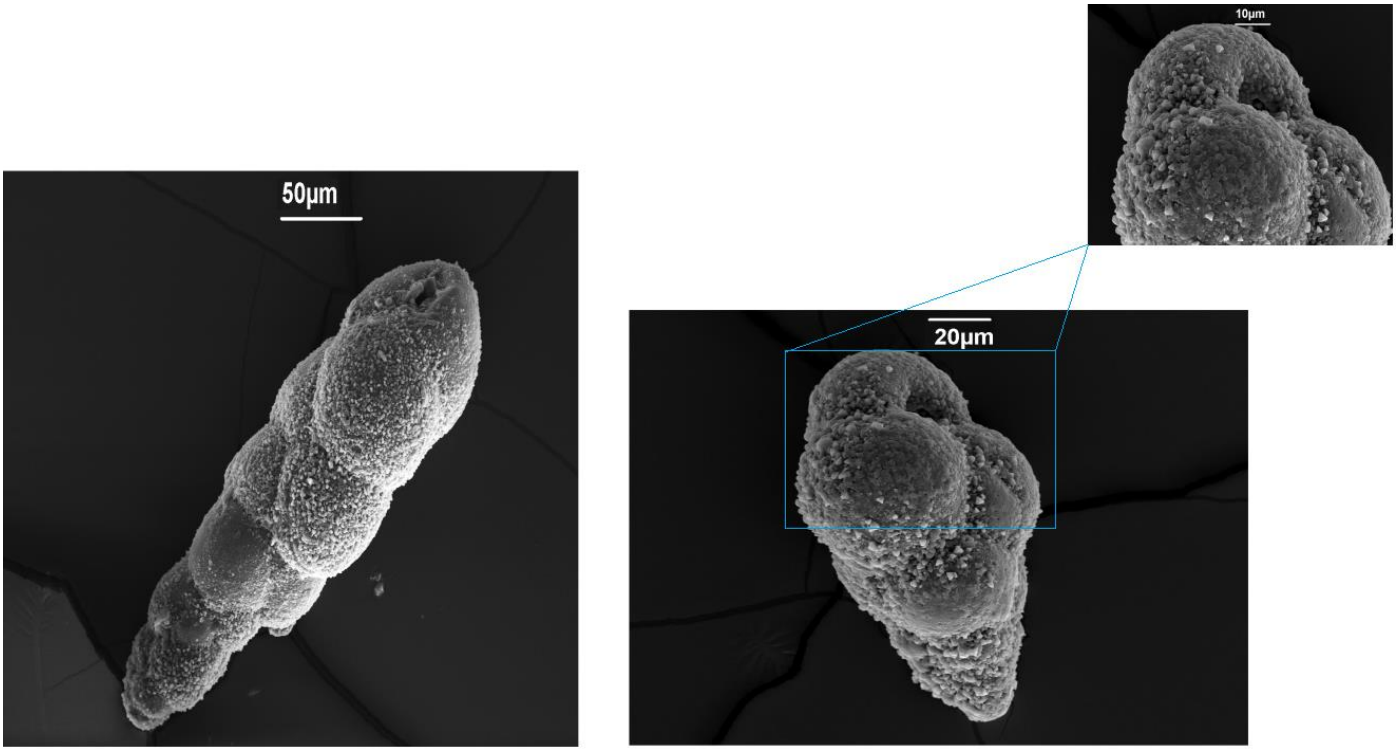


**Figure 34:** *Benthic foraminifera from the Discovery Deep core, coated with crystal-like particles.*

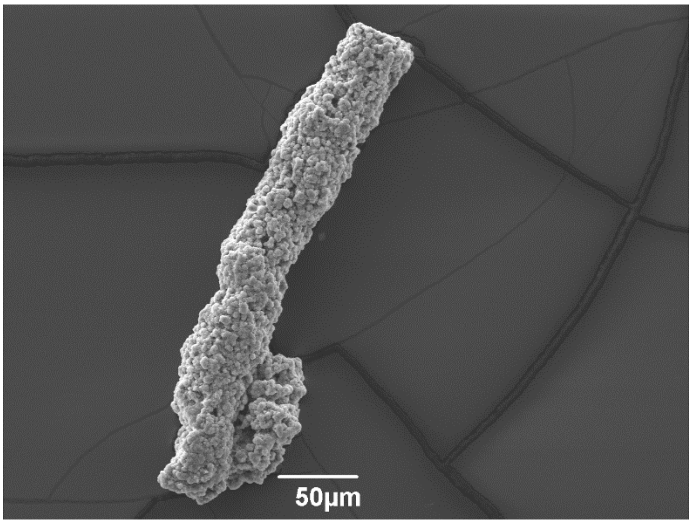


**Figure 35:** *Agglutinated fragment from the Discovery Deep core, covered with crystal-like particles.*

Eventually, in addition to all the aforementioned findings, an overall assessment of the planktonic foraminiferal assemblages provides evidence for the absence of species with large tests in both Unit A and Unit C. Instead, species with small tests (<125μm) prevail. In contrast, in Unit B as well as in the lamina of Unit C (at 328 cm), planktonic foraminifera with shell size >125 μm are also abundant.

# 7. DISCUSSION

Even though significant emphasis has been given to the geochemistry of the metalliferous sediments of Atlantis II Deep (hydrothermally precipitated from the up to ~70 ºC brine; (Modenesi & Santamarina, 2022)), which is undoubtedly the most mineralized deep of Red Sea and one of the largest present-day ore-forming environments, the studies concerning the neighboring Discovery Deep brine pool (formed ~5 km southwest of the Atlantis II Deep) are quite limited and rather old. Firstly, Swallow & Crease (1965) reported the presence of Fe-bearing sediments in the deep, while afterwards Miller et al. (1966) and Ross et al. (1973) provided in detail the results of their investigation on recent Fe-deposits in the area. In addition, Bischoff (1969), besides a diversity of authigenic minerals, such as limonite, goethite, Fe-montmorillonite, Mn-bearing siderite, lepidocrocite and pyrite, identified detrital material consisting of pteropods, coccoliths and foraminiferal shells, along with minor amounts of quartz, feldspar and clays.

Hence, in order to update the existing knowledge regarding the sedimentation processes in the Discovery Deep hot brine as well as its paleoceanographic evolution, the results obtained from physico-chemical and foraminiferal analyses (together with $^{14}C$ dating) of a geoarchive from the site have been integrated. It should be emphasized that hydrothermal activity is an integral component of the seafloor accretion processes because the circulating fluids and plumes facilitate the thermal and chemical exchange between the oceans and the crust, supporting life above and below the seafloor, and affect hydrodynamics and biological activity at water depths shallower than the abyssal zone. In addition, the hydrothermal sediment deposits are valuable for their (usually) increased metal content, for their crucial role in the growth of extremophile ecosystems, for the evidence that provide to support the understanding of the spatial-temporal variability in hydrothermal venting and, finally, for their function as geological records of how life at hydrothermal vent systems has evolved.

The geoarchive from the Discovery Deep, extending up to 3.5 m below the seafloor, exhibits three distinct lithostratigraphic units, reflecting diverse sedimentation processes and environmental conditions during deposition. The temporal fluctuations in the sedimentological and micropaleontological characteristics of the sedimentary column indicate pronounced changes in the depositional environment over the past 21-22 kyr. These changes include time intervals of “normal” pelagic background biodetrital sedimentation in the Red Sea Rift with rates ranging from 9-20 cm/ka, mostly configured by sediment flows through the steep basalt slopes of the deep due to the numerous earthquake swarms in Red Sea (Quliti et al., 2016), as well as periods of extreme depositional rates (53-107 cm/ka) with the relevant sedimentation being mainly the result of hydrothermal activity. All aforementioned high sedimentation rates compared to the typical marine pelagic deposition in the global ocean are nicely reflected by the poorly to very poorly sorted sediments of the Discovery Deep core.

An analogous sedimentary succession has also been recorded in cores recovered from the adjacent Atlantis II Deep hot brine, where hydrothermal highly-metalliferous deposits, enriched in Au, Ag, Co, Cu, Fe, Mn and Zn, overlie a stratigraphic unit consisting of biogenic and detrital material (Degens & Ross, 1969; Cocherie et al., 1994; Laurila et al., 2014b). However, the contents of the previous metals in the Discovery Deep core, except those of Mn and Zn at specific stratigraphic intervals only, are significantly lower, in the order of hundreds and thousands of ppm (Laurila et al., 2014a; Laurila et al., 2014b; Barrett et al., 2021). This finding is consistent with previous studies, which found analogous low metal concentrations in both the brine and the sediments of Discovery Deep (Degens & Ross, 1969; Modenesi & Santamarina, 2022). However, the low Fe contents along the entire analyzed deposit are in contrast with the studied of Swallow & Crease (1965), Miller et al. (1966) and Ross et al. (1973), who have suggested the occurrence of Fe deposits in the area. This probably implies that the spatial distribution in the Discovery Deep sediment cover is rather non-uniform.

In any case, based on the results of the present study as well as on the previous investigations, it can be suggested that the metalliferous sedimentary load underlying the Discovery Deep brine must be of much lower economic importance compared to the adjacent Atlantis II Deep. This might be attributed to the fact that the Discovery Deep is not a self-sustained brine pool (Hunt et al., 1967; Degens & Ross, 1969; Backer & Schoell, 1972; Schoell & Faber, 1978; le Quentrec & Sichler, 1991; Faber et al., 1998; Hartmann et al., 1998; Anschutz et al., 1999), but it develops from occasional intense overflows of the Atlantis II Deep, which are discharged into the Discovery Deep through a topographic sill (at a water depth of ~1900 m) that has established their "interconnection". Therefore, since it is assumed that there is not any heating source beneath the Discovery Deep that directly feeds the area with high-salinity hydrothermal fluids, then it is reasonable for the contents of the chemically precipitated metals within the local sediments to be significantly lower than those found in the Atlantis II Deep sediments. Furthermore, the high temperatures recorded in the Discovery Deep the past decades (1964 and 1995) should rather be attributed to its proximity to the present-day active vent site in the SW part of Atlantis II Deep and the assumed "interconnection" between the two deeps (Backer & Schoell, 1972; Schoell & Hartmann, 1973; Schoell & Faber, 1978; Hartmann et al., 1998). This is also in accordance with the condition observed at the top of the currently analyzed core, which did not show any evidence of recent local hydrothermal impact. Finally, in contrast to Atlantis II Deep, the sediments below the Discovery Deep brine are colder than the brine itself, further supporting that there is a lack of heating source beneath the study area (Hunt et al., 1967; Degens & Ross, 1970).

Concerning the onset of the hydrothermal impact on the Discovery Deep environment, the age-depth model of the present investigation indicates that the hydrothermal deposition should have begun at 15-16 cal ka BP. In contrast, the dating of the metalliferous sediments (accumulating at an average rate of ~50 cm/ka on basaltic bedrock) in the Atlantis II Deep provides ages going back to ~25 kyr (Ku et al., 1969; Shanks & Bischoff, 1977; Cocherie et al., 1994). Hence, the suggestion that the two deeps are "interconnected" and there is lack of a local hydrothermal feeder for the Discovery Deep is also favored by the fact that the hydrothermal sedimentation in Atlantis II Deep precedes the corresponding process in the Discovery Deep, provided of course that the analyzed core has penetrated through the entire sedimentary overburden below the brine column.

Faber et al. (1998) proposed that the hydrocarbons (e.g., methane) found in samples from the Discovery Deep were likely formed through the thermal degradation of the occurring organic matter. Consequently, this could explain the low TOC contents (most of them being less than 0.5%) of the currently analyzed deposit. In addition, the TOC/TN ratio calculated for the entire investigated geoarchive, which unexpectedly suggest a terrestrial origin, is a real enigma. Apparently, wind-borne dust (Palchan et al., 2018; Ehrmann et al., 2024) could contribute to the formation of the investigated deposit, but wind-blown dust can form only a minor portion of deep sea sediments on a volumetric basis (Rea, 2009) and is not feasibly to dominate the TOC/TN proxy. On the other hand, intense hydrodynamic transport of terrestrial material has not been found at the moment in Red Sea areas. Therefore, the only explanation for the enhanced TOC/TN ratio could be the process of nitrogen fixation by thermophilic (up to 75 ºC) chemosynthetic microbial communities thriving in the deep (Siam et al., 2012; Wang et al., 2013).

The majority of previous studies on sediment cores retrieved from the Red Sea hot brines consistently reported the essential absence of benthic foraminifera due to the anoxic environment (Miller et al., 1966; Degens & Ross, 1969; Hartmann et al., 1998; Coulibaly et al., 2006). However, the microfossil analyses in these studies were performed on sieves with sizes larger than 63 μm (e.g., 125, 150, 325 μm). In contrast to the aforementioned studies, an exception to this trend was presented in the study of Abu-Zied (2013) who analyzed the 63 μm fraction, revealing the existence of benthic foraminiferal tests in sediments retrieved from the brines in Shaban and Kebrit deeps. Likewise, in the present study benthic foraminifera (with small test) were also identified only within the 63 μm fraction throughout the investigated core. Strikingly, when an inspection of the 125 μm fraction in the same samples was carried out, the lack of benthic foraminifera species was evident.

In light of the documented presence of small-size benthic fauna within the brine-filled deeps (previously considered only anoxic and devoid of benthic life), a periodic dissolved oxygen influx has been implied for the extreme environments. Edelman-Furstenberg et al. (2001) reported that every 4-7 years, convection events in Red Sea initiate the renewal of deep waters, leading to cooler, fresher conditions and a significant increase in the dissolved oxygen content near the seafloor. Additionally, this occasional bottom water renewal is also suggested by the periodic appearances of laminated sediments in the Shaban deep, as documented by Seeberg-Elverfeldt et al. (2005).

Despite the generally low density of benthic foraminifera in the Discovery Deep core (revealed by the BFN index), the existence of moderate to high diversity, coupled with the low dominance trend in the occurring population, indicates that there are not any opportunistic taxa that exclusively dominate the seemingly inhospitable environment of the study site. Instead, benthic foraminifera assemblages are primarily characterized by taxa that are indicators of dysoxic conditions, such as *Bolivina* spp. and *Eggerella* spp. (Kaiho 1994; Langlet et al., 2014).

## Unit C (15.7-21.4 ka BP)

The lithostratigraphic Unit C is a clear example of the typical pelagic background sedimentation in the Red Sea Rift and represents a glacial MIS-2 deposit. The relatively homogenized mud deposit and the lower sedimentation rates (~8.8 cm/ka) indicate stable environmental conditions and lack of hydrothermally-influenced sedimentation. Similarly, the lower contents of mining metals, such as Fe, Mn, Zn and chalcophile elements, within this unit supports the lack of hydrothermal activity.

The only prominent change in the stratigraphic column of this unit is the occurrence of a dark laminae (less than 1 cm thick) at 19 cal ka BP, which coincides with a sharp decrease in the Mn/Fe ratio, implying Mn reduction processes. Sporadic changes in the environmental conditions may also be implied by the occurrence of small-size planktonic foraminifera in the Discovery Deep deposit of Unit C, which according to Abu-Zied (2012) can be attributed to changes in the brine-seawater interface.

Specifically, he concluded that the high density and salinity of the brine in a deep may effectively cause segregation of the brine water from normal seawater. Therefore, it is possible that the precipitated planktonic foraminifera tests are sorted at the brine-seawater interface. Hence, large-test foraminifera of possible high buoyancy are unable to enter the brine, while small-test foraminifera of possible low buoyancy are more likely to settle on the brine seafloor. The process that could potentially affect the condition in the brine-seawter interface in the Discovery Deep area might be an abrupt increase in the hydrothermal activity in Atlantis II Deep, resulting in brine overflows from there to Discovery Deep sub-basin, modifying the stratification of the brine in the study area. Finally, the sudden increase in the BFN index and the diversity of the benthic assemblage at 17.9 cal ka BP, along with the occurrence of the genus *Globocassidulina* sp., an indicator of oxic conditions (Kaiho, 1994), which is entirely absent in the rest of Unit C, could be attributed to a minor input of dissolved oxygen in the brine. Nevertheless, any other significant changes in the sedimentological characteristics of Unit C were not observed.

## Unit B (4.4-15.7 ka BP)

Unit B exhibits drastic changes in its sedimentological characteristics. The sedimentary layers in this unit display significant variability in the RGB color, MS values, grain size statistical parameters (i.e., Mz and $K_G$) and geochemical characteristics, definitely due to hydrothermal impact.

In more detail, the sediments in Unit B are mainly enriched in Mn (reaching up to excessive values of ~62,300 ppm) and Zn (reaching up to ~1540 ppm) at specific stratigraphic intervals, compared to Unit C and A, apparently associated with hydrothermal impact. However, among the chalcophile elements only Zn competes with analogous contents in the Atlantis II Deep sediments (Anschutz et al., 1990). In addition, it is quite interesting that the MS distribution at the stratigraphic interval 170-220 cm shows ferromagnetic signal caused by an interfacial Mn/Fe coupling, which occurs when thin coatings of the paramagnetic Mn are deposited on body-centered cubic (bcc) Fe phases (Andrieu et al., 1997). An analogous distinct ferromagnetism has also been observed in the metalliferous sediments from Atlantis II Deep (Modenesi & Santamarina, 2022).

Another prominent characteristic of Unit B is the occurrence of extreme sedimentation rates (53-107 cm/ka) in the major part (87-217 cm) of the stratigraphic column, coinciding with a dramatic increase (up to ~80%) in the sand fraction. Such a rapid deposition has also been recorded from the Atlantis II Deep and is clearly associated with intense hydrothermal venting and remarkable metalliferous sedimentation (Shanks & Bischoff, 1977; Laurila et al., 2014a). However, such enhanced sand contents have not been recorded for the deposits from Atlantis II Deep by previous studies (Bischoff, 1969; Zierenberg & Shanks, 1988; Modenesi & Santamarina, 2022). In the case of Discovery Deep, the potential sources of the increased sand fraction should be (i) potential vigorous overflows from the Atlantis II Deep that eroded the "interconnection" route (sill) between the two neighboring deeps or/and (ii) mass wasting events from the steep basalt flanks of the Discovery Deep sub-basin.

The metal precipitation, and, subsequently, the mineralogical composition in the Red Sea hot brines, are regulated by geochemical processes influenced by the interplay between the hydrothermal vent fluid – seawater mixing and the oxidation/reduction potential (Eh) (Zierenberg & Shanks, 1988; Anschutz et al., 2000). In the brine that accumulates inside the hot deeps, when low Eh values prevail, then Mn remains in solution and diffuse out of the brine, while under oxidizing conditions (i.e., high Eh values) Mn precipitates, forming distinct Mn-rich sediments at the bottom of the deeps. In contrast, a reversed trend has been observed for Fe, forming Fe-rich sedimentary facies under reducing conditions (Scholten et al., 1991; Anschutz et al., 2000; Laurila et al., 2014b). Therefore, the peaks observed in the Mn content and Mn/Fe ratio profiles of the currently analyzed deposit reflect changes in the redox conditions within the brine, emphasizing the occurrence of some oxic time intervals in a type of environment that is commonly anoxic or dysoxic.

Further, it should be noticed that the measured low Fe contents in the Discovery Deep geoarchive, compared to the increased values reported from the Atlantis II Deep (ranging from 25 to 55 wt% and even up to ~60 wt%) (Laurila et al., 2014a; Barrett et al., 2021), is in agreement with the study of Danielsson et al. (1980), which concluded that these differences have likely been caused by the oxygen amount reaching the deepest part of the Discovery Deep brine due to the lack of an intermediate brine zone, thus, influencing Fe precipitation.

Concerning the benthic fauna, a noteworthy characteristic of Unit B is the presence of agglutinated foraminiferal fragments. This indicates a different depositional environment compared to Units A and C, where these fragments are either entirely absent or occur in low abundances. Furthermore, the presence of calcareous infaunal benthic foraminifera, tolerant to dysoxic conditions, along with the occurrence of the oxygen-dependent *Globocassidulina* sp., suggests the lack of entirely anoxic conditions at the seafloor below the brine. However, the foraminiferal specimens found in this unit are poorly preserved and coated by crystal-like particles, most probably due to the influence of hydrothermal activity and metal precipitation. In addition, large-test planktonic foraminifera are present in the microfaunal population of this stratigraphic unit. Therefore, according to Abu-Zied (2012), their presence indicates the weakening of the brine stratification, which allowed the large planktonic foraminifera (of potential high buoyancy) to settle on the seabed. As it has already been mentioned, the brine stratification in the Discovery Deep can be destabilized by the assumed discharges of hydrothermal fluids from the Atlantis II Deep into the Discovery Deep sub-basin.

### Unit A (0-4.41 ka BP)

The younger lithostratigraphic Unit A consists of pelagic sediment deposited during the warm MIS-1. This unit does not demonstrate the typical colorful and bright sedimentary layers occurring within the analogous stratigraphic interval (being still hydrothermal active) of the nearby Atlantis II Deep sedimentary sequence (Hunt et al., 1967) and of course, visually, it appears completely different from the underlying hydrothermally-impacted Unit B. The metal contents in the sedimentary column are, generally, close to the background values and only a few values of Mn (up to ~3600 ppm) and Zn (up to ~600 ppm) appear enhanced in the stratigraphic interval 40-60 cm (2-4 cal ka BP). The moderate increase in the contents of Mn and Zn could be the result of liquefaction processes triggered by the seismicity or excessive heating flow in the central Red Sea Rift that could promote the migration and diffusion of metals from the interior of the sedimentary column towards the seabed surface (Lu et al., 2019). Therefore, it is reasonable to assume that any evident hydrothermal activity in the study area from ~4.4 cal ka BP up to the present is absent. In particular, the current inert state of the Discovery

Deep brine pool is in agreement with the previous studies of Degens & Ross (1969) and Swift et al. (2012).

The dormant state of the Discovery Deep is also supported by the nonexistence of large foraminiferal tests within Unit A (which, in contrast, were present in Unit B), implying a well-established stratification in the brine-seawater interface. The occurring stratification, being the result of the lack of overflows from the Atlantis II Deep to Discovery Deep (being not strong enough to spill over the "interconnection" sill), hinders the intrusion of the large planktonic foraminifera into the brine's bottom. In addition, the constant low Mn/Fe ratio along Unit A, indicates a stability of the redox conditions, which is conformable with the hydrothermally unaffected brine column for the past ~4.4 kyr.

Finally, in most studies concerning the Red Sea hot brines, the non-hydrothermal sediments are predominantly composed of fine mud (Bischoff, 1969; Zierenberg & Shanks, 1988; Modenesi & Santamarina, 2022). However, in Unit A, during the Late Holocene (Meghalayan), between 2-4 cal ka BP, the prevalence of sand is obvious. This striking change in the sediment particle size should be configured by the joint contribution of two processes: (i) sediment gravity flows (being the primary sand source) originating from the unstable basaltic flanks of the Discovery Deep sub-basin, due to the ongoing seismic and volcanic activity in the central Red Sea Rift (Vita-Finzi & Spiro, 2006); and (ii) aeolian transport (being the secondary sand source), because by the onset of Meghalayan (4.2 ka) and for ~2 kyr, the climate in the Red Sea region was extremely aridic (Mayewski et al., 2004; Edelman-Furstenberg et al., 2009), leading to increased sand/dust influxes in the central Red Sea (Palchan & Torfstein, 2019; Sergiou et al., 2022).

# 8. CONCLUSIONS

The key findings of the current research effort can be summarized as follows:

- The sedimentation processes in the Discovery Deep hot brine pool are a combination of Red Sea background sediment accumulation and hydrothermal-induced deposition. During the glacial MIS-2 and Meghalayan stage (i.e., the most recent stage of Holocene) sedimentation with rates of 9-20 cm/ka was taking place via typical pelagic deposition, material accumulation from sediment gravity flows and minor aeolian deposition of sand and dust. The depositional environment during the aforementioned time intervals was characterized by metal contents in the sediments close to their background values, dysoxic conditions and strong stratification in the brine column. Further, the hydrothermal impact on the Discovery Deep sub-basin began at 15-16 cal ka BP and ceased at ~4.4 cal ka BP up to the present time, as documented by the enhanced Mn and Zn values (up to ~62,300 ppm and ~1540 ppm, respectively), the extreme sedimentation rates (53-107 cm/ka), the ferromagnetic signal of the magnetic susceptibility measurements, the distinct color-banding of the deposited layers and laminae, and, eventually, the specific characteristics of the benthic foraminiferal assemblages.
- Despite the seemingly inhospitable conditions in the Discovery Deep area, the identified benthic foraminiferal assemblages emphasize the adaptability of these organisms to extreme environments. However, their distribution and morphological characteristics are clearly influenced when hydrothermal processes are in progress. Additionally, the existence of extremophile

microorganisms that fix the nitrogen occurring in the sediments should be very likely.

- Regardless of the long-term hydrothermal impact on the study area, the metal contents in the sediments below the brine appear much lower than someone could expect, except of Mn and Zn at specific stratigraphic intervals only. This implies that Discovery Deep is not an autonomous venting field, but it is rather fed by intense hydrothermal overflows of the nearby Atlantis II Deep major venting system.
- The presence of benthic foraminifera tolerant to dysoxic conditions, along with oxygen-dependent species, in combination with the relatively low Fe contents and the occurrence of Mn-rich layers suggest the absence of entirely anoxic conditions in the study area.
- Finally, the dominance of sand fraction within a major stratigraphic interval of the hydrothermally-impacted portion in the Discovery Deep geoarchive should mainly be the result of (i) the seabed intense erosion caused by potential overflows from the Atlantis II Deep to the study area via their “interconnection” route (topographic sill) or/and (ii) the likely mass wasting episodes through the unstable, steep basalt flanks of the Discovery Deep sub-basin.

# REFERENCES


Abu-Zied, R.H., 2013. Effect of the Red Sea brine-filled deeps (Shaban and Kebrit) on the composition and abundance of benthic and planktonic foraminifera. Arabian Journal of Geosciences, Volume 6, pp. 3809-3826.

Addy, S. K. & Behrens, E., 1980. Time of accumulation of hypersaline anoxic brine in Orca basin (Gulf of Mexico). Marine Geology, 37(3-4), pp. 241-252.

Adel, M. et al., 2016. Viruses-to-mobile genetic elements skew in the deep Atlantis II brine pool sediments. Scientific Reports, 6(1), p. 32704.

Almogi-Labin, A., Hemleben, C., Meischner, D. & Erlenkeuser, H., 1991. Paleoenvironmental events during the last 13,000 years in the central Red Sea as recorded by pteropoda. Paleoceanography, 6(1), pp. 83-98.

Andrieu, S. et al., 1997. 1 ML Mn/Fe(001): Is Mn coupling with Fe antiferromagnetic or ferromagnetic?. Journal of Magnetism and Magnetic Materials, 165(1-3), pp. 191-194.

Anschutz, P. et al., 1999. Hydrographic changes during 20 years in the brine-filled basins of the Red Sea. Deep Sea Research Part I: Oceanographic Research Papers, 46(10), pp. 1779-1792.

Anschutz, P., Blanc, G., Fritz, B. & Boulegue, J., 1990. Characterisation of the physico-chemical conditions during the settling of metalliferous sediments in the Atlantis-II Deep (Red Sea). Chemical Geology, Volume 84, pp. 192-193.

Anschutz, P., Blanc, G., Monnin, C. & Boulègue, J., 2000. Geochemical dynamics of the Atlantis II Deep (Red Sea): II. Composition of metalliferous sediment pore waters. Geochimica et Cosmochimica Acta, 64(23), pp. 3995-4006.

Antunes, A., Ngugi, D. & Stingl, U., 2011. Microbiology of the Red Sea (and other) deep-sea anoxic brine lakes. Environmental Microbiology Reports, 3(4), pp. 416-433.

Augustin, N., van der Zwan, F. M., Devey, C. W. & Brandsdóttir, B., 2021. 13 million years of seafloor spreading throughout the Red Sea Basin. Nat Commun, 12(1), 2427.

Avramidis, P., Nikolaou, K. & Bekiari, V., 2015. Total Organic Carbon and Total Nitrogen in Sediments and Soils: A Comparison of the Wet Oxidation – Titration Method with the Combustion-infrared Method. Agriculture and Agricultural Science Procedia, Volume 4, pp. 425-430.

Backer, H. & Schoell, M., 1972. New Deeps with Brines and Metalliferous Sediments in the Red Sea. Nature Physical Science, Volume 240, pp. 153-158.

Baker, E. T. & German, C. R., 2004. On the global distribution of hydrothermal vent fields. In: C. R. German, J. Lin & L. M. Parson, eds. Mid-Ocean Ridges: Hydrothermal Interactions Between the Lithosphere and Oceans. (AGU Geophysical Monograph, 148). Washington, D.C, USA: American Geophysical Union, pp. 245-266.

Barrett, T. J., Jarvis, I., Hannington, M. D. & Thirlwall, M. F., 2021. Chemical characteristics of modern deep-sea metalliferous sediments in closed versus open basins, with emphasis on rare-earth elements and Nd isotopes. Earth-Science Reviews, Volume 222, p. 103801.

Batang, Z. B. et al., 2012. First discovery of a cold seep on the continental margin of the central Red Sea. Journal of Marine Systems, Volume 94, pp. 274-253.

Berggren, W., 1969. Micropaleontologic Investigations of Red Sea Cores-Summation and Synthesis of Results. In: E. T. Degens & D. A. Ross, eds. Hot Brines and Recent Heavy Metal Deposits in the Red Sea. New York: Springer, pp. 329-335.

Bischoff, J. L., 1969. Red Sea Geothermal Brine Deposits: Their Mineralogy, Chemistry, and Genesis. In: E. Degens & D. Ross, eds. Hot Brines and Recent Heavy Metal Deposits in the Red Sea. Berlin, Heidelberg: Springer, pp. 368-401.

Blanc, G. & Anschutz, P., 1995. New stratification in the hydrothermal brine system of the Atlantis II Deep, Red Sea. Geology, 23(6), pp. 543-546.

Blott, Simon & Pye, Kenneth. (2015). GRADISTATv8.

Blum, N. & Puchelt, H., 1991. Sedimentary-hosted polymetallic massive sulfide deposits of the Kebrit and Shaban Deeps, Red Sea. Mineral. Deposita, Volume 26, pp. 217-227.

Bonatti, E., 1985. Punctiform initiation of seafloor spreading in the Red Sea during transition from a continental to an oceanic rift. Nature, Volume 316, pp. 33-37.

Bonatti, E., Cipriani, A. & Lupi, L., 2015. The Red Sea: Birth of an Ocean. In: N. Rasul & I. Stewart, eds. The Red Sea. Springer Earth System Sciences. Berlin, Heidelberg: Springer, pp. 29-44.

Boström, K., Arquharson, B. F. & Eyl, W., 1972. Submarine hot springs as a source of active ridge sediments. Chemical Geology, 10(3), pp. 189-203.

Boström, K. & Fisher, D. E., 1969. Distribution of mercury in East Pacific sediments. Geochimica et Cosmochimica Acta, 33(6), pp. 743-745.

Boström, K. & Peterson, M. N. A., 1966. Precipitates from hydrothermal exhalations on the east pacific rise. Economic Geology, 61(7), pp. 1258-1265.

Boström, K. & Peterson, M. N. A., 1969. The origin of aluminum-poor ferromanganoan sediments in areas of high heat flow on the East Pacific Rise. Marine Geology, 7(5), pp. 427-447.

Bosworth, W., 2015. Geological Evolution of the Red Sea: Historical Background, Review, and Synthesis. In: N. Rasul & I. Stewart, eds. The Red Sea. Springer Earth System Sciences. Berlin, Heidelberg: Springer, pp. 45-78.

Bosworth, W., Huchon, P. & McClay, K., 2005. The Red Sea and Gulf of Aden Basins. Journal of African Earth Sciences, Volume 43, pp. 334-378.

Botz, R. et al., 2007. Organic-rich sediments in brine-filled Shaban- and Kebrit Deeps, Northern Red Sea. Chemical Geology, 244(3-4), pp. 520-553.

Brueckmann, W., Kraetschell, A. & Augustin, N., 2017. Data Mining the Red Sea Atlantis II Deep. Houston, Texas, USA, Paper presented at the Offshore Technology Conference.

Bugrova, E., 2020. Biostratigraphy of the Paleogene of Syria Based on Small Benthic Foraminifera. Stratigraphy and Geological Correlation, December, 28(1), pp. 765-780.

Bunzel, D. et al., 2017. A multi-proxy analysis of Late Quaternary ocean and climate variability for the Maldives, Inner Sea. Clim. Past, 13(12), pp. 1791-1813.

Canfield, D. E., 1994. Factors influencing organic carbon preservation in marine sediments. Chemical Geology, 114(3-4), pp. 315-329.

Cavalier-Smith, T., 2018. Kingdom Chromista and its eight phyla: a new synthesis emphasising periplastid protein targeting, cytoskeletal and periplastid evolution, and ancient divergences. Protoplasma, September, Volume 255, pp. 297-357.

Cesbron, F. et al., 2016. Vertical distribution and respiration rates of benthic foraminifera: Contribution to aerobic remineralization in intertidal mudflats covered by Zostera noltei meadows. Estuarine, Coastal and Shelf Science, Volume 179, pp. 23-38.

Chu, D. & Gordon, R. G., 1998. Current plate motions across the Red Sea. Geophysical Journal International, 135(2), pp. 313-328.

Chung, Y., Finkel, R. C. & Kim, K., 1982. 226Ra, 210Pb and 210Po in the Red Sea. Earth and Planetary Science Letters, 58(2), pp. 213-224.

Cita, M. B., 2006. Exhumation of Messinian evaporites in the deep-sea and creation of deep anoxic brine-filled collapsed basins. Sedimentary Geology, Volume 188-189, pp. 357-378.

Cocherie, A., Calvez, J. Y. & Oudin-Dunlop, E., 1994. Hydrothermal activity as recorded by Red Sea sediments: Sr-Nd isotopes and REE signatures. Marine Geology, 118(3-4), pp. 291-302.

Cochran, J. R., 1983. A Model for Development of Red Sea. The American Association of Petroleum Geologists Bulleliti, 67(1), pp. 41-69.

Coleman, R. G., 1974. Geological Background of the Red Sea. In: C. A. Burk & C. L. Drake, eds. The Geology of Continental Margins. Berlin, Heidelberg: Springer, pp. 743-751.

Corliss, J. B. et al., 1979. Submarine Thermal Springs on the Galápagos Rift. Science, 203(4385), pp. 1073-1083.

Cosentino, C. et al., 2017. Benthic foraminifera as indicators of relative sea-level fluctuations: Paleoenvironmental and paleoclimatic reconstruction of a Holocene marine succession (Calabria, south-eastern Tyrrhenian Sea). Quaternary International, May, 493(part A), pp. 79-101.

Coulibaly, A. S. et al., 2006. The effect of paleo-oceanographic changes on the sedimentary recording of hydrothermal activity in the Red Sea during the last 30,000 years. Marine Geology, 226(1-2), pp. 51-64.

Craig, H., 1966. Isotopic Composition and Origin of the Red Sea and Salton Sea Geothermal Brines.. Science, 154(3756), pp. 1544-1548.

Cronan, D., 1972. The Mid-Atlantic Ridge near 45 °N, XVII: Al, As, Hg, and Mn in Ferruginous Sediments from the Median Valley. Canadian Journal of Earth Sciences, 9(3), pp. 319-323.

Culver, S. J., 1991. Early Cambrian Foraminifera from West Africa. Science, 254(5032), pp. 689-691.

Danielsson, L.-G., Dyrssen, D. & Granéli, A., 1980. Chemical investigations of Atlantis II and discovery brines in the Red Sea. Geochimica et Cosmochimica Acta, 44(12), pp. 2051-2065.

De Lange, G. J. et al., 1990. Composition of anoxic hypersaline brines in the Tyro and Bannock Basins, eastern Mediterranean. Marine Chemistry, 31(1-3), pp. 63-88.

Degens, E. T. & Ross, D. A., 1969. Hot Brines and Recent Heavy Metal Deposits in the Red Sea. 1 ed. Berlin, Heidelberg: Springer .

Degens, E. T. & Ross, D. A., 1970. Hot brines and recent heavy metal deposits in the Red Sea. Geologiska Föreningen i Stockholm Förhandlingar, 92(2), pp. 246-248.

Degens, E. T. & Ross, D. A., 1970. The Red Sea Hot Brines. Scientific American, 222(4), pp. 32-43.

Dekkers, M., 1978. Magnetic properties of sediments. In: Sedimentology. Encyclopedia of Earth Science. Berlin, Heidelberg: Springer.

Dekov, V. M. et al., 2007. Fe–Mn-(hydr)oxide-carbonate crusts from the Kebrit Deep, Red Sea: Precipitation at the seawater/brine redoxcline. Marine Geology, 236(1-2), pp. 95-119.

Delaunay, A. et al., 2023. Structure and morphology of the Red Sea, from the mid-ocean ridge to the ocean-continent boundary. Tectonophysics, Volume 849, p. 229728.

DeMets, C., Gordon, R. G. & Argus, D. F., 2010. Geologically current plate motions. Geophysical Journal International, 181(1), pp. 1-80.

D'haenens, S., Bornemann, A., Stassen, P. & P.Speijer, R., 2012. Multiple early Eocene benthic foraminiferal assemblage and δ13C fluctuations at DSDP Site 401 (Bay of Biscay — NE Atlantic). Marine Micropaleontology, May, Volume 88-89, pp. 15-35.

Dieckmann, G. S. et al., 1991. Antarctic sea ice; a habitat for the foraminifer Neogloboquadrina pachyderma. Journal of Foraminiferal Research, April, 21(2), pp. 182-189.

Dimiza, M. et al., 2016. The Foram Stress Index: A New Tool for Environmental Assessment of Soft-Bottom Environments Using Benthic Foraminifera. A Case Study from the Saronikos Gulf, Greece, Eastern Mediterranean. Ecol. Indic., Volume 60, pp. 611-621.

Duarte, C. M. et al., 2020. Discovery of Afifi, the shallowest and southernmost brine pool reported in the Red Sea. Scientific Reports, 10, 910.

Edelman-Furstenberg, Y., Almogi-Labin, A. & Hemleben, C., 2009. Palaeoceanographic evolution of the central Red Sea during the late Holocene. The Holocene, 19(1), pp. 117-127.

Edelman-Furstenberg, Y., Scherbacher, M., Hemleben, C. & Almogi-Labin, A., 2001. Deep-Sea Benthic Foraminifera from the Central Red Sea. Journal of Foraminiferal Research, 31(1), pp. 48-59.

Eder, W., Schmidt, M., Koch, M. & Garbe-Schönberg, D. H. R., 2002. Prokaryotic phylogenetic diversity and corresponding geochemical data of the brine-seawater interface of the Shaban Deep, Red Sea. Environmental Microbiology, 4(11), pp. 758-763.

Edwards, F. J., 1987. Climate and Oceanography. In: J. F. Edwards & M. S. Head, eds. Key Environments: Red Sea. Oxford: Pergamon Press, pp. 45-69.

Ehrmann, W. et al., 2024. Monsoon-driven changes in aeolian and fluvial sediment input to the central Red Sea recorded throughout the last 200 000 years. Clim. Past, 20(1), pp. 37-52.

El-Kahawy, R. et al., 2018. Morphological deformities of benthic foraminifera in response to nearshore pollution of the Red Sea, Egypt. Environmental Monitoring and Assessment, 190(5), 312.

Faber, E. et al., 1998. Methane in Red Sea brines. Organic Geochemistry, 29(1-3), pp. 363-379.

Farmer, J., 2000. Hydrothermal systems: Doorways to early biosphere evolution. GSA Today, 10(7), pp. 1-9.

Fenton, M., Geiselhart, S., Rohling, E. J. & Hemleben, C., 2000. Aplanktonic zones in the Red Sea. Marine Micropaleontology, 40(3), pp. 277-294.

Fisher, D. & Boström, K., 1969. Uranium Rich Sediments on the East Pacific Rise. Nature, Volume 224, pp. 64-65.

Fisher, R. A., Corbet, A. S. & Williams, C. B., 1943. The Relation Between the Number of Species and the Number of Individuals in a Random Sample of an Animal Population. Journal of Animal Ecology, 12(1), pp. 42-58.

Folk, R., 1974. Petrology of Sedimentary Rocks. Austin, Texas: Hemphill Publishing Co..

Folk, R. L. & Ward, W. C., 1957. Brazos River Bar: A Study in the Significance of Grain Size Parameters. Journal of Sedimentary Petrology, Volume 27, pp. 3-6.

Fouquet, Y., 1997. Where are the large hydrothermal sulphide deposit in the oceans?. Proceedings of the Royal Society A: Mathematical, Physical and Engineering Sciences, 355(1723), pp. 427-441.

Frerichs, W., 1970. Paleobathymetry, paleotemperature, and tectonism. Bulletin of the Geological Society of America, November, 81(11), pp. 3445-3452.

Frerichs, W. E., 1971. Paleobathymetric trends of neogene foraminiferal assemblages and sea floor tectonism in the Andaman Sea area. Marine Geology, October, Volume 11, pp. 159-173.

Frontalini, F. & Coccioni, R., 2008. Benthic foraminifera for heavy metal pollution monitoring: A case study from the central Adriatic Sea coast of Italy. Estuarine, Coastal and Shelf Science, January, 76(2), pp. 404-417.

German, C. R. & Seyfried, W. E., 2014. 8.7 - Hydrothermal Processes. In: H. D. Holland & K. K. Turekian, eds. Treatise on Geochemistry (Second Edition). s.l.:Elsevier, pp. 191-233.

Gogou, A. et al., 2007. Organic geochemical evidence of Late Glacial–Holocene climate instability in the North Aegean Sea. Palaeogeography, Palaeoclimatology, Palaeoecolog, 256(1-2), pp. 1-20.

Goldstein, S. T., 1997. Gametogenesis and the antiquity of reproductive pattern in the Foraminiferida. Journal of Foraminiferal Research, October, 27(4), pp. 319-328.

Groves, J. R., Larghi, C., Nicora, A. & Rettori, R., 2003. Mississippian (Lower Carboniferous) microfossils from the Chios Mélange (Chios Island, Greece). Geobios, Jule, 36(4), pp. 379-389.

Guney, M., Al-Marhoun, M. A. & Nawab, Z. A., 1988. Metalliferous sub-marine sediments of the Atlantis-II-Deep, Red Sea. CIM Bulletin, 18(910), pp. 33-39.

Gurvich, E. G., 2006. Metalliferous sediments of the Red Sea. In: Metalliferous sediments of the World Ocean: fundamental theory of Deep-Sea hydrothermal sedimentation. Berlin: Springer, pp. 127-210.

Hammer, O., Harper, D. & Ryan, P., 2001. Past: paleontological statistics software package for educaton and data anlysis. Palaeontologia electronica, 4(1), p. 9.

Hannington, M. D., de Ronde, C. D. J. & Petersen, S., 2005. Sea-floor tectonics and submarine hydrothermal systems. In: J. W. Hedenquist, J. F. H. Thompson, R. J. Goldfarb & J. P. Richards, eds. Economic Geology 100th Anniversary Volume. Littelton, Colorado, USA: Society of Economic Geologists, pp. 111-141.

Hannington, M. et al., 2011. The abundance of seafloor massive sulfide deposits. Geology, 39(12), pp. 1155-1158.

Harris, P. T., 2020. Chapter 6 - Seafloor geomorphology—coast, shelf, and abyss. In: H. Peter T & B. Elaine, eds. Seafloor Geomorphology as Benthic Habitat (Second Edition). s.l.:Elsevier, pp. 115-160.

Hartmann, M., Scholten, J. C., Stoffers, P. & Wehner, F., 1998. Hydrographic structure of brine-filled deeps in the Red Sea—new results from the Shaban, Kebrit, Atlantis II, and Discovery Deep. Marine Geology, 144(4), pp. 311-330.

Heaton, R. C., Jackson, M. P. A., Bamahmoud, M. & Nani, A. S. O., 1995. Superposed Neogene Extension, Contraction, and Salt Canopy Emplacement in the Yemeni Red Sea. In: M. Jackson, D. Roberts & S. Snelson, eds. Salt tectonics: a global perspective. s.l.:AAPG Memoir 65, pp. 333-351.

Heaton, T. et al., 2020. Marine20—The Marine Radiocarbon Age Calibration Curve (0–55,000 cal BP). Radiocarbon, 62(4), pp. 779-820.

Hess, H. H., 1962. History of Ocean Basins. In: A. E. J. Engel, H. L. James & B. F. Leonard, eds. Petrologic Studies: A Volume to Honor A. F. Buddington. s.l.:Geological Society of America, Boulder, pp. 599-620.

Hoffmann, R., 1991. Marginalia: Hot Brines in the Red Sea. American Scientist, 79(4), pp. 298-299.

Holbourn, A., Henderson, A. S. & MacLeod, N., 2013. Introduction. In: Atlas of Benthic Foraminifera. s.l.:Natural History Museum, pp. 1-13.

Horowitz, A. & Cronan, D., 1976. The geochemistry of basal sediments from the North Atlantic Ocean. Marine Geology, 20(3), pp. 205-228.

Hunt, J. M., Hays, E. E., Degens, E. T. & Ross, D. A., 1967. Red Sea: Detailed Survey of Hot-Brine Areas. Science, 156(3774), pp. 514-516.

Ikpeama, M. O. U., Boger, P. D. & Faure, G., 1974. A study of strontium in core 119K, Discovery deep, Red Sea. Chemical Geology, 13(1), pp. 11-22.

Izzeldin, A. Y., 1987. Seismic, gravity and magnetic surveys in the central part of the Red Sea: their interpretation and implications for the structure and evolution of the Red Sea. Tectonophysics, 143(4), pp. 269-306.

Jannasch, H. W. & Wirsen, C. O., 1979. Chemosynthetic Primary Production at East Pacific Sea Floor Spreading Centers. BioScience, 29(10), pp. 592-598.

Jorissen, F., 1999. Benthic foraminiferal microhabitats below the sediment-water interface. In: Modern Foraminifera. Springer, Dordrecht, pp. 161-179.

Jorissen, F. J., Stigter, H. C. d. & Widmark, J. G., 1995. A conceptual model explaining benthic foraminiferal. Marine Micropaleontology, December, 26(1-4), pp. 3-15.

Kaiho, K., 1994. Benthic foraminiferal dissolved-oxygen index and dissolved-oxygen levels in the modern ocean. Geology, Volume 22, pp. 719-722.

Ku, T.-L., Thurber, D. & Mathieu, G., 1969. Radiocarbon Chronology of Red Sea Sediments. In: E. R. D. Degens, ed. Hot Brines and Recent Heavy Metal Deposits in the Red Sea . Berlin, Heidelberg: Springer, pp. 348-359.

LaBrecque, J. & Zitellini, N., 1985. Continuous sea-floor spreading in Red Sea: an. AAPG Bulletin, 69(4), pp. 513-524.

LaFemina, P. C., 2015. Chapter 3 - Plate Tectonics and Volcanism. In: H. Sigurdsson, ed. The Encyclopedia of Volcanoes (Second Edition). s.l.:Academic Press, pp. 65-92.

Langer, M. R., 2008. Assessing the Contribution of Foraminiferan Protists to Global Ocean Carbonate Production. Journal of Eukaryotic Microbiology, February, 55(3), pp. 163-169.

Langlet, D. et al., 2014. Foraminiferal species responses to in situ, experimentally induced anoxia in the Adriatic Sea. Biogeosciences, 11(7), pp. 1775-1797.

Laurila, T. E. et al., 2015. New insights into the mineralogy of the Atlantis II Deep metalliferous sediments, Red Sea. Geochemistry, Geophysics, Geosystems, 16(12), pp. 4449-4478.

Laurila, T. E., Hannington, M. D., Petersen, S. & Garbe-Schönberg, D., 2014a. Early depositional history of metalliferous sediments in the Atlantis II Deep of the Red Sea: Evidence from rare earth element geochemistry. Geochimica et Cosmochimica Acta, Volume 126, pp. 146-168.

Laurila, T. E., Hannington, M. D., Petersen, S. & Garbe-Schönberg, D., 2014b. Trace metal distribution in the Atlantis II Deep (Red Sea) sediments. Chemical Geology, Volume 386, pp. 80-100.

le Quentrec, M. F. & Sichler, B., 1991. 3-D inversion of deep tow magnetic data on the Atlantis II Deep (Red Sea): hydrothermal and geodynamic interpretation. Tectonophysics, 198(2-4), pp. 421-439.

Loeblich, A. R. & Tappan, H., 1987. Foraminiferal Genera and Their Classification. Van Nostrand Reinhold Company, New York. 970pp. New York: s.n.

Loizeau, J., Span, D., Coppee, V. & Dominik, J., 2001. Evolution of the trophic state of Lake Annecy (eastern France) since the last glaciation as indicated by iron, manganese and phosphorus speciation. Journal of Paleolimnology, Volume 25, pp. 205-214.

Ludwig, J. A. & Reynolds, J. F., 1988. Statistical Ecology: A Primer in Methods and Computing. 1 ed. New York: Wiley-Interscience Pub..

Lu, F. et al., 2019. Migration and Diffusion of Heavy Metal Cu from the Interior of Sediment during Wave-Induced Sediment Liquefaction Process. Journal of Marine Science and Engineering, 7(12), p. 449.

Malvern Instruments Ltd, 2007. Mastersizer 2000 Essential, user manual. Worcestershire, UK: Malvern Instruments.

Mapelli, F. et al., 2017. An Updated View of the Microbial Diversity in Deep Hypersaline Anoxic Basins. In: Adaption of Microbial Life to Environmental Extremes: Novel research results and application. Vienna: Springer-Verlag, pp. 23-40.

Martins, M. V. A. et al., 2016. Can benthic foraminifera be used as bio-indicators of pollution in areas with a wide range of physicochemical variability?. Estuarine, Coastal and Shelf Science, December, 182(part A), pp. 211-225.

Mayewski, P. et al., 2004. Holocene Climate Variability. Quaternary Research, Volume 62, pp. 243-255.

Mckenzie, D., Davies, D. & Molnar, P., 1970. Plate Tectonics of the Red Sea and East Africa. Nature, Volume 226, pp. 243-248.

McManus, J., 1988. Grain size determination and interpretation. In: M. Tucker, ed. Techniques in Sedimentology. UK: Blackwell, pp. 63-85.

Meyers, P. A., 1994. Preservation of elemental and isotopic source identification of sedimentary organic matter. Chemical Geology, 114(3-4), pp. 289-302.

Miller, A. R. et al., 1966. Hot brines and recent iron deposits in deeps of the Red Sea. Geochimica et Cosmochimica Acta, 30(3), pp. 341-359.

Modenesi, M. C. & Santamarina, J. C., 2022. Hydrothermal metalliferous sediments in Red Sea deeps: Formation, characterization and properties. Engineering Geology, Volume 305, p. 106720.

Monin, A. S. et al., 1982. Red Sea Submersible Research Expedition. Deep-Sea Research, 29(3), pp. 361-373.

Morcos, S. A., 1970. Physical and chemical oceanography of the Red Sea. Oceanogr Mar Biol Ann Rev, Volume 8, pp. 73-202.

Murray, J., 1991. Ecology and Palaeoecology of Benthic Foraminifera. 1st ed. Harlow/Essex, New York: Longman, Wiley,.

Murray, S. P. & Johns, W., 1997. Direct observations of seasonal exchange through the Bab el Mandab Strait. Geophysical Research Letters, 24(21), pp. 2557-2560.

Naeher, S. et al., 2013. Tracing bottom water oxygenation with sedimentary Mn/Fe ratios in Lake Zurich, Switzerland. Chemical Geology, Volume 352, pp. 125-133.

National Oceanic and Atmospheric Administration, Hydrothermal Vents and Ocean Chemistry. Submarine Ring of Fire 2002. NOAA/OER. [Online] Available at: https://oceanexplorer.noaa.gov/explorations/02fire/background/vent_chem/ventchem.html [Accessed 15 10 2023].

Nawab, Z. A., 1984. Red Sea mining: A new era. Deep Sea Research Part A. Oceanographic Research Papers, 31(6-8), pp. 813-822.

O'neill, B. J., 1996. Using Microfossils in Petroleum Exploration. The Paleontological Society Papers, October, Volume 2, pp. 237-246.

Palchan, B. et al., 2018. Dust transport and synoptic conditions over the Sahara–Arabia deserts during the MIS6/5 and 2/1 transitions from grain-size, chemical and isotopic properties of Red Sea cores. Earth and Planetary Science Letters, Volume 382, pp. 125-139.

Palchan, D. & Torfstein, A., 2019. A drop in Sahara dust fluxes records the northern limits of the African Humid Period. Nat Commun, Volume 10, p. 3803.

Patzert, W. C., 1974. Wind-induced reversal in Red Sea circulation. Volume 21, pp. 109-121.

Pawlowski, J. et al., 2003. The evolution of early Foraminifera. Proc Natl Acad Sci U S A, 100(20), pp. 11494-8.

Pedgley, D. E., 1974. An outline of the weather and climate of the Red Sea. L'Oceanographie Physique de la Mer Rouge, pp. 9-27.

Pérez-Asensio, J. & Rodríguez-Ramírez, A., 2020. Benthic Foraminiferal Salinity index in marginal-marine environments: A case study from the Holocene Guadalquivir estuary, SW Spain. Palaeogeography, Palaeoclimatology, Palaeoecology, December, Volume 560, p. 110021.

Pierret, M. C., Clauer, N., Bosch, D. & Blanc, G., 2010. Formation of Thetis Deep metal-rich sediments in the absence of brines, Red Sea. Journal of Geochemical Exploration, 104(1-2), pp. 12-26.

Purkis, S. et al., 2022. Discovery of the deep-sea NEOM Brine Pools in the Gulf of Aqaba, Red Sea. Communications Earth & Environment, Volume 3, 146.

Quliti, S. et al., 2016. Assessment of Main Parameters of Extreme Earthquakes in Red Sea, West Coast of Saudi Arabia. Open Journal of Earthquake Research, 5(2), pp. 122-134.

Rasul, N. M. A., Stewart, I. C. F. & Nawab, Z. A., 2015. Introduction to the Red Sea: Its Origin, Structure, and Environment. In: N. Rasul & I. Stewart, eds. The Red Sea. Springer Earth System Sciences. Berlin, Heidelberg: Springer, pp. 1-28.

Rea, D. K., 2009. Eolian Dust, Marine Sediments. In: V. Gornitz, ed. Encyclopedia of Paleoclimatology and Ancient Environments. Encyclopedia of Earth Sciences Series. Dordrecht: Springer, pp. 308-312.

Reghellin, D., Coxall, H. K., Dickens, G. R. & Backman, J., 2015. Carbon and oxygen isotopes of bulk carbonate in sediment deposited beneath the eastern equatorial Pacific over the last 8 million years. Paleoceanography, September, 30(10), pp. 1261-1286.

Reicherter, K. et al., 2010. The sedimentary inventory of tsunamis along the southern Gulf of Cádiz (southwestern Spain). Zeitschrift für Geomorphologie, Supplementary Issues, 54(3), pp. 147-173.

Rosenthal, Y., A.Boyle, E. & Slowey, N., 1997. Temperature control on the incorporation of magnesium, strontium, fluorine, and cadmium into benthic foraminiferal shells from Little Bahama Bank: Prospects for thermocline paleoceanography. Geochimica et Cosmochimica Acta, September, 61(17), pp. 3633-3643.

Ross, D. et al., 1973. Red sea drillings. Science, 179(4071), pp. 377-380.

Rothwell, R. & Rack, F., 2006. New techniques in sediment core analysis: An introduction. Geological Society London Special Publications, 267(1), pp. 1-29.

Saada, S. A., Mickus, K., Eldosouky, A. M. & Amin , I., 2021. Insights on the tectonic styles of the Red Sea rift using gravity and magnetic data. Marine and Petroleum Geology, Volume 133, p. 105253.

Schoell, M. & Faber, E., 1978. New isotopic evidence for the origin of Red Sea brines. Nature, Volume 275, pp. 436-438.

Schoell, M. & Hartmann, M., 1973. Detailed temperature structure of the hot brines in the Atlantis II Deep area (Red Sea). Marine Geology, 14(1), pp. 1-14.

Scholten, J. C., Stoffers, P., Walter, P. & Plüger, W., 1991. Evidence for episodic hydrothermal activity in the Red Sea from the composition and formation of hydrothermal sediments, Thetis Deep. Tectonophysics, 190(1), pp. 109-117.

Seeberg-Elverfeldt, I. A. et al., 2004. The significance of diatoms in the formation of laminated sediments of the Shaban Deep, Northern Red Sea. Marine Geology, 209(1-4), pp. 279-301.

Seeberg-Elverfeldt, I., Lange, C., Pätzold, J. & Kuhn, G., 2005. Laminae type and possible mechanisms for the formation of laminated sediments in the Shaban Deep, northern Red Sea. Ocean Science, 1(2), pp. 113-126.

Sen Gupta, B., 1999. Modern Foraminifera. Dordrecht: Kluwer academic Publishers.

Sergiou, S. et al., 2022. Influences of sea level changes and the South Asian Monsoon on southern Red Sea oceanography over the last 30 ka. Quaternary Research, Volume 110, pp. 114-132.

Shaltout, M., 2019. Recent sea surface temperature trends and future scenarios for the Red Sea. Oceanologia, 61(4), pp. 484-504.

Shanks, W. C. & Bischoff, J. L., 1977. Ore transport and deposition in the Red Sea geothermal system: a geochemical model. Geochimica et Cosmochimica Acta, 41(10), pp. 1507-1519.

Shannon, C. E., 1948. A mathematical theory of communication. The Bell System Technical Journal, 27(3), pp. 379-423.

Shimadzu Scientific Instruments, n.d. Shimadzu Corporation. [Online] Available at: https://www.shimadzu.com/ [Accessed 19 10 2023].

Siam, R. et al., 2012. Unique Prokaryotic Consortia in Geochemically Distinct Sediments from Red Sea Atlantis II and Discovery Deep Brine Pools. PLoS ONE, 7(8), p. e42872.

Siemensma, F. et al., 2017. Taxonomic revision of freshwater foraminifera with the description of two new agglutinated species and genera. European Journal of Protistology, August, Volume 60, pp. 28-44.

Sofianos, S. & Johns, W. E., 2015. Water Mass Formation, Overturning Circulation, and the Exchange of the Red Sea with the Adjacent Basins. In: N. Rasul & I. Stewart, eds. The Red Sea. Springer Earth System Sciences. Berlin, Heidelberg: Springer, pp. 343-353.

Sofianos, S. S., Johns, W. E. & Murray, S. P., 2002. Heat and freshwater budgets in the Red Sea from direct observations at Bab el Mandeb. Deep Sea Research Part II: Topical Studies in Oceanography, 49(7-8), pp. 1323-1340.

Southon, J. et al., 2002. Marine Reservoir Corrections for the Indian Ocean and Southeast Asia. Radiocarbon, 44(1), pp. 167-180.

Stern, R. J. & Johnson, P. R., 2019. Constraining the Opening of the Red Sea: Evidence from the Neoproterozoic Margins and Cenozoic Magmatism for a Volcanic Rifted Margin. In: N. Rasul & I. Stewart, eds. Geological Setting, Palaeoenvironment and Archaeology of the Red Sea. Cham: Springer, pp. 53-79.

Stuiver, M. & Reimer, P., 1993. Extended 14C Data Base and Revised CALIB 3.0 14C Age Calibration Program. Radiocarbon, Volume 35, pp. 215-230.

Swallow, J. C. & Crease, J., 1965. Hot Salty Water at the Bottom of the Red Sea. Nature, Volume 205, pp. 165-166.

Swift, S. A., Bower, A. S. & Schmitt, R. W., 2012. Vertical, horizontal, and temporal changes in temperature in the Atlantis II and Discovery hot brine pools, Red Sea. Deep Sea Research Part I: Oceanographic Research Papers, Volume 64, pp. 118-128.

Thornburg, C. C., Zabriskie, T. M. & McPhail, K. L., 2010. Deep-Sea Hydrothermal Vents: Potential Hot Spots for Natural Products Discovery?. J. Nat. Prod, 73(3), pp. 489-499.

Thunell, R., Locke, S. M. & Williams, D. F., 1988. Glacio-eustatic sea-level control on Red Sea salinity. Nature, Volume 334, pp. 601-604.

Triantafyllou, G. et al., 2014. Exploring the Red Sea seasonal ecosystem functioning using a three-dimensional biophysical model. Journal of Geophysical Research: Oceans, 119(3), pp. 1791-1811.

Triantaphyllou, M. et al., 2021. Paleoenvironmental evolution and sea level change in the Saronic Gulf (Aegean Sea, Greece): evidence from the Piraeus coastal plain and Elefsis Gulf sedimentary records. Water, 13(12), p. 1621.

Ukstins, I. A. et al., 2002. Matching conjugate volcanic rifted margins: 40Ar/39Ar chrono-stratigraphy of pre- and syn-rift bimodal flood volcanism in Ethiopia and Yemen. Earth and Planetary Science Letters, 198(3-4), pp. 289-306.

van der Zwan, F. M., Devey, C. W. & Augustin, N., 2019. Hydrothermal Prospection in the Red Sea Rift: Geochemical Messages from Basalts. In: N. M. A. Rasul & I. C. F. Stewart, eds. Geological Setting, Palaeoenvironment and Archaeology of the Red Sea. Cham: Springer, pp. 221-232.

Vestheim, H. & Kaartvedt, S., 2016. A deep sea community at the Kebrit brine pool in the Red Sea. Marine Biodiversity, 46(1), pp. 59-65.

Vita-Finzi, C. & Spiro, B., 2006. Isotopic indicators of deformation in the Red Sea. Journal of Structural Geology, Volume 28, pp. 1114-1122.

Waelbroeck, C. et al., 2002. Sea-level and deep water temperature changes derived from benthic foraminifera isotopic records. Quaternary Science Reviews, 21(1-3), pp. 295-305.

Wang, Y. et al., 2013. Autotrophic Microbe Metagenomes and Metabolic Pathways Differentiate Adjacent Red Sea Brine Pools. Scientific Reports, Volume 3, p. 1748.

Wang, Y. et al., 2015. Zonation of Microbial Communities by a Hydrothermal Mound in the Atlantis II Deep (the Red Sea). PLoS ONE, 10(10), p. e0140766.

Watson, S. W. & Waterbury, J. B., 1969. The Sterile Hot Brines of the Red Sea. In: E. Degens & D. Ross, eds. Hot Brines and Recent Heavy Metal Deposits in the Red Sea. Berlin, Heidelberg: Springer, pp. 272-281.

Wentworth, C. K., 1922. A Scale of Grade and Class Terms for Clastic Sediments. 30(5), pp. 177-192.

Werner, F. & Lange, K., 1975. A bathymetric survey of the Sill Area between the Red Sea and the Gulf of Aden. Geologisches Jahrbuch D, Volume 13, pp. 125-130.

Wilson, R. W. et al., 2019. Fifty years of the Wilson Cycle concept in plate tectonics: an overview. Geological Society, London, Special Publications, 470(1), pp. 1-17.

Winckler, G. et al., 2001. Constraints on origin and evolution of Red Sea brines from helium and argon isotopes. Earth and Planetary Science Letters, 184(3-4), pp. 671-683.

Winters, W. J., 1987. Guidelines for handling, storing, and preparing soft marine sediment for geotechnical testing. Open-File Report 87-278, Massachusetts : U.S. Geological Survey: Woods Hole.

WoRMS Editorial Board, 2023. World Register of Marine Species. [Online] Available at: https://www.marinespecies.org [Accessed 6 11 2023].

Xie, J., Krokos, G., Sofianos, S. & Hoteit, I., 2019. Interannual Variability of the Exchange Flow Through the Strait of Bab-al-Mandeb. Journal of Geophysical Research: Oceans, 124(3), pp. 1988-2009.

Young, R. A. & Ross, D., 1974. Volcanic and sedimentary processes in the Red Sea axial trough. Deep-Sea Research, Volume 21, pp. 289-297.

Zambetakis-Lekkas, A., Pomoni-Papaioannou, F. & Alexopoulos, A., 1998. Biostratigraphical and sedimentological study of Upper Senonian - Lower Eocene sediments of Tripolitza Platform in central Crete (Greece). Cretaceous Research, December, Volume 19, pp. 715-732.

Zierenberg, R. A. & Shanks, W. C., 1988. Isotopic studies of epigenetic features in metalliferous sediment, Atlantis II Deep, Red Sea. Canadian Mineralogist, 26(3), pp. 737-753.

Zumbo, V., Feraud, G., Bertrand, H. & Chazot, G., 1995. 40Ar/39Ar chronology of Tertiary magmatic activity in Southern Yemen during the early Red Sea-Aden Rifting. Journal of Volcanology and Geothermal Research, 65(3-4), pp. 265-279.